Empirical Relations Between the Earth's Radiation Budget, Cloudiness, and Various Meteorological Parameters

Thesis by Daniel Wenkert

In partial fulfillment of the requirements
for the degree of
Doctor of Philosophy

California Institute of Technology
Pasadena, California

1986
(submitted October 4, 1985)

To my parents and my brother and sisters

Acknowledgements

Many people helped in the work that went into this thesis. First of all I would like to thank my thesis advisor, Andy Ingersoll. He first suggested that there might be worthwhile discoveries to be made in the raw statistics of the Nimbus 7 ERB radiances and encouraged me to develop a technique to correct for the lack of diurnal coverage in that data, along with providing help along the way. I received programing help from K. Matsumoto, E. Huang, R. Logan, and D. Alexander. Both L. Stowe and V. R. Taylor of NOAA/NESDIS were forthcoming in supplying me with tapes of data before they had been described in the literature and in answering many questions I had on ERB and the STRTs in particular. M. Suarez of UCLA and GLAS was helpful in explaining a number of things about the FGGE Level-IIIb data set. The NSF supported me through a Graduate Fellowship during much of this research. Just about all the faculty, the students, and the staff in Planetary Science at Caltech, provided worthwhile scientific discussions or help at some point in my graduate program. I would especially like to thank Jim, Tony, Todd, Maria, Jim, Mary, Randy, and Steve for raising flagging morale at various times.

Above all, I would like to thank all the members of my family, especially my parents, for providing emotional, and sometimes financial, support during my graduate career.

ABSTRACT

I have investigated the effect of variation of meteorological variables, cloudiness, and surface variables (such as albedo and continentality) on the reflected solar and emitted terrestrial radiation leaving the top of the atmosphere. The investigation was empirical and used the radiometric data from the scanner channels of the Earth Radiation Budget (ERB) instrument on Nimbus 7, cloudiness variables from analyses done by L.Stowe et al. on data from the Temperature and Humidity Infrared Radiometer (THIR) on Nimbus 7, and meteorological data from the FGGE (First GARP Global Experiment) Level III-b global weather analyses. The data were analysed on time scales of one day and spatial scales of about 450 km.

This investigation had three main goals. The first goal was to determine the effect of cloudiness on the net radiation for various surface and atmospheric conditions during the period investigated (12 June to 18 June 1979). The second goal was to determine whether or not this type of linear analysis on a data set of synoptic time and space scales could be used for a reasonable and empirically accurate parameterization of radiation to be used in simple energy balance climate models (which are valid at vastly larger time and space scales than this data set). The third goal was to compare the regressions determined from this data set between radiation, cloudiness, and weather with the

internal statistics developed in a Global Circulation Model (GCM), with the idea that eventually this type of linear analysis could be used as a constraint on GCMs used by the atmospheric science community.

TABLE OF CONTENTS

Acknowledgements iv

Abstract v

List of Figures x

List of Tables xii

Chapter 1 INTRODUCTION AND GOALS 1

Chapter 2 ORIGIN OF THE DATA 7

A) Nimbus 7 ERB and radiation data 7

B) Nimbus 7 THIR and cloud cover 11

C) The FGGE Level III-b data set from ECMWF and weather variables 13

D) Geographic data on the STR and RAND/SIO tapes 15

Chapter 3 METHOD OF DATA ANALYSIS 18

A) Turning an analysis of radiances into an analysis of flux 18

B) Dividing the upward hemisphere into discrete bins 25

C) The diurnal coverage problem and its solution 28

D) Calculation of the diurnal correction factors 37

Chapter 4 EXPLANATION OF THE PARAMETERS INVESTIGATED AND THE TECHNIQUES USED IN THE CALCULATIONS 47

A) Reasons for choosing the variables listed in Table 4.1 for this investigation 47

B) Conversion of FGGE Level IIIb data into the variables listed in Table 4.1 53

C) The development of an albedo table from the published literature 64

D) The determination of average values for all the visible and infrared radiances and other variables for each target area for each day 67

E) The determination of the summation matrices 70

F) Filling in blanks in the summation matrices 74

G) Which summation matrices were calculated 76

H) How the covariance matrices and average vectors were used 80

Chapter 5 RESULTS 83

A) What sort of results were best and why 84

B) Sources and magnitudes of error 88

C) How cloudiness affects the planetary albedo and fluxes at the top of the atmosphere 99

D) Simple diagnostic equations for albedo and outgoing infrared flux at the top of the atmosphere 121

E) Statistics of use in testing general circulation models and synoptic scale variables diagnostic of cloudiness 130

Chapter 6 CONCLUSIONS 143

A) The implications of these results for the Earth's climate 144

B) Future directions in this research 148

REFERENCES 152

Appendix A BRIEF DESCRIPTION OF THE DATA SETS USED TO DETERMINE SURFACE ALBEDOES 158

Appendix B A STATISTICAL COMPARISON OF THE RESULTS DERIVED FROM ANALYSES USING DIFFERENT PATTERNS OF ANGULAR BINS FOR THE VISIBLE RADIANCES 164

Appendix C A COMPARISON OF THE RESULTS DERIVED FROM ANALYSES USING DIFFERENT MODELS FOR THE DIURNAL VARIATION OF BIDIRECTIONAL REFLECTANCE AND THEREFORE DIFFERENT DIURNAL CORRECTION FACTORS FOR VISIBLE RADIANCES 175

Appendix D A STATISTICAL COMPARISON OF THE RESULTS DERIVED FROM ANALYSES USING DIFFERENT QUANTITIES OF DATA 184

List of Figures

Chapter 2

2.1 ERB scan pattern (single vertical scan) 9

2.2 The five different ERB scan modes 9

Chapter 3

3.1 Visible ERB scanner data taken in one day for several target areas 20

3.2 An explanation of the coordinates 23

3.3 The patterns of angular bins used in this thesis 26

3.4 Albedo versus solar zenith angle for the Stowe-Taylor data 32

3.5 Comparisons of the Stowe-Taylor data with the results of the three diurnal variation models used in this thesis 41

Chapter 5

5.1 Effect of cloudiness on flux versus latitude 104

5.2 "Measured" flux versus cloudiness 105

5.3 Contrast between June and November in the effect of cloudiness on flux versus latitude 109

5.4 Contrast between continents and oceans in the effect of cloudiness on flux versus latitude 113

5.5 Comparison of single and multiple parameter regressions of net flux vs. cloudiness 117

5.6 Effect of cloudiness on flux vs. average cloudiness for various latitudes 119

5.7 Total derivative of net flux with respect to total cloudiness against total derivative of cloudiness with respect to surface temperature 119

5.8 Zonal average flux versus zonal average surface temperature 126

5.9 Correlation coefficients of cloud-related meteorological parameters with albedo and infrared flux vs. latitude 134

5.10 Multiple correlation coefficients for regressions of albedo and infrared flux against many cloud-related meteorological parameters vs. latitude 137

List of Tables

Chapter 4

4.1 The variables investigated in this thesis and the symbols used for them 48

4.2 Analysis techniques, geographic groupings, and wavelength categories used in this thesis and the headings for them as used in tables 77

Chapter 5

5.1 Number of independent observations of visible and infrared flux for 4.5° latitude bands 100

5.2 Effect of total cloud fraction on top-of-the-atmosphere albedo and fluxes for various regions of the Earth 102

5.3 The average of the total cloud fraction and its effect on top-of-the-atmosphere albedo and fluxes for one day in June 1979 and one day in November 1978 108

5.4 Regression coefficients for flux vs. total cloud fraction 111

5.5 Regression coefficients for top-of-the-atmosphere radiation for three cloud type multiple regression for the 8 LATITUDES geographic grouping 115

5.6 Regression coefficients for top-of-the-atmosphere albedo and emitted longwave flux in terms of surface temperature 123

5.7 Regression coefficients for outgoing infrared flux in terms of surface temperature from earlier studies 124

Chapter 1

INTRODUCTION AND GOALS

What is the effect on the Earth's surface climate (especially annually-averaged surface temperature and rainfall) of a doubling of the atmosphere's CO_2 concentration? What is the effect of a changing solar ''constant'' or a changing Earth orbit on these climatic parameters? These and other questions related to the Earth's climate are not as easily answered as they are posed. One of the main reasons for the difficulty of their solution is that the atmospheric radiation budget, and therefore the surface climate, is heavily influenced by the distribution of various types of cloudiness, at least on time scales of less than a year. Webster and Stephens (1984), for example, estimate that a mere 10% increase in the amount of low-altitude cloud cover around the globe would wipe out the expected increase in surface temperature associated with the doubling of atmospheric CO_2.

Even the most sophisticated atmospheric models of our time are not notorious for their ability to simulate the present day distribution and characteristics of clouds around the Earth (see Liou and Curran (1984) for a discussion). Moreover, cloud amount and height are not the only important parameters. Somerville and Remer (1984) have found that any variation of liquid water content in clouds with temperature might have substantial consequences for the

global albedo. Many of the processes influencing the physical characteristics of clouds are only poorly understood or else very difficult to model. Most models of the Earth's atmosphere are computed on large spatial scales (typically about 500 km to 1000 km between grid points), but the processes influencing cloudiness often take place on smaller scales. Another problem is that the effects of certain types of clouds (especially laterally heterogeneous clouds like those associated with boundary layer convection) on the atmospheric radiation field are not that well known (see Harshvardhan, 1982).

Although the theoretical situation is still muddled, recently two observational data sets have become available that can help solve the question of the effect of various amounts and types of clouds on the Earth's radiation budget. One data set consists of the spatially and angularly resolved measurements of radiation leaving the top of the atmosphere determined by the scanner channels of the Earth Radiation Budget (ERB) instrument on the Nimbus 7 spacecraft. Between November 1978 and June 1980 these channels returned spectrally integrated visible (0.2 μm to 4.5 μm) and infrared (4.5 μm to >50 μm) radiances for all regions of the Earth on a four day cycle (usually three days on and one day off). The radiances were measured at angular resolutions of 0.25° by 5.12° and spatial resolutions of 4 km by 85 km at the nadir and 350 km by 320 km at the horizon (limb as seen from the spacecraft). Since the

satellite was in a sun synchronous orbit, with equator crossings at noon and midnight, all measurements outside of high latitudes were made near local noon and local midnight. In support of ERB and other experiments on Nimbus 7, an infrared camera, THIR (Temperature Humidity Infrared Radiometer), was carried onboard to determine the extent and type of cloudiness in the regions of the Earth being viewed by the Nimbus experiments. The other data set is the vast trove of meteorological measurements taken in association with the First GARP Global Experiment (FGGE) or Global Weather Experiment. For the year from December 1978 to December 1979, a large array of meteorological platforms (satellites, ships, airplanes, balloons, and surface stations), many of them specially designed for FGGE, returned conventional and some unconventional weather data. Particular concern was paid to filling in data gaps in ocean areas and the southern hemisphere. The entire data set was binned, averaged, and interpolated using a general circulation model (GCM) that the European Center for Medium Range Forecasting (ECMWF) uses operationally for weather forecasting.

I had three goals in mind in analyzing these data. The first goal was to determine how the distribution of clouds (as they occur now) in the Earth's atmosphere affects the radiation budget of the surface and atmosphere. The second goal was to develop equations that could be used to predict top-of-the-atmosphere radiation fields for simple climate

models. Since these are simple models, involving only a few meteorological variables, I did not want to explicitly include cloudiness. So I looked for equations in simple parameters (e.g., surface temperature, surface albedo, etc.) to predict the radiation field that bypassed cloud cover prediction. The third goal was to develop empirical relations between top-of-the-atmosphere radiation and various meteorological parameters of importance for predicting cloudiness and radiation in general circulation models (GCMs). I hope, in the future, to compare these relations with the internal statistics of various GCMs.

This is not the first time that someone has attempted to solve the three problems outlined above. Ohring and Gruber (1983) provide a good review of past work on the first two goals. Linder et al. (1981) and Jensenius et al. (1978) are good examples of work toward the third goal. The data sets I used, however, allow a more sophisticated analysis of cloudiness, radiation, and weather than has been possible in the past.

The technique I used to accomplish these goals involved analyzing the statistics (averages, variances, and covariances) of ERB radiance measurements. These statistics were then corrected for possible systematic errors involved in the poor diurnal coverage provided by the sun-synchronous Nimbus 7. The diurnally corrected statistics of the radiances were then combined (as described in Chapter 3) to provide statistics involving the top-of-the-atmosphere

emerging visible flux, infrared flux, and planetary albedo. The resulting statistics relating the fluxes and albedo with all the other parameters were used for various single and multiple parameter regressions. The technique, in itself, provided what might be said to be the zeroth goal of this thesis, in that much time and effort was spent in determining whether the results of this work were sensitive to changes in various specifics of the analysis.

The results of this investigation are as follows. I have determined that the distribution of clouds on Earth as it occurs in our present climate (at least for 28 November 1978 and 12-18 June 1979) has no great net effect on the Earth's radiation budget as a whole. This is in contrast to a number of previous studies that have shown measurable and important effects of cloudiness on the global net radiation in the annual average. For example, Hartmann and Short (1980) found that increased cloud cover would tend to cool the Earth, due to the effect on albedo being larger than the effect on outgoing terrestrial infrared radiation. However, my results indicate that cloudiness does have a significant impact on the seasonal radiation budgets. Increased cloud cover acts to buffer seasonal excursions in the net radiation (decreasing net radiative intake in summer and increasing it in winter).

Equations were developed that I feel might be usable for estimation of the top-of-the-atmosphere radiation field in simple energy balance climate models. These equations have

coefficients for predicting the emission of longwave radiation from the surface temperature that are noticeably larger than those derived from most previous studies. However, they are similar to the results of a more recent study by Simmonds and Chidzey (1982), that used seasonal rather than annual average data.

Finally, empirical relations between various meteorological parameters (on the shorter time and smaller spatial scales of GCMs) and top-of-the-atmosphere radiation have been determined. When eventually compared with the internal statistics of GCMs these can serve as an empirical check on the validity of these models and thus help to fine tune them. In at least one comparison with previous work (that of Linder, et al., 1981) a multiple regression was able to explain a much larger fraction of the variance in the planetary albedo than was possible before.

Chapter 2

ORIGIN OF THE DATA

In this chapter I explain where the data that I used originated. My most important data came from the Nimbus 7 spacecraft. Nimbus 7 was placed in a circular sun synchronous polar orbit about the earth in mid-November 1978. This spacecraft orbits about the Earth every 104 minutes at 955 km altitude, crossing the equator at longitudinal separations of 26° at local noon and midnight.

II.A) Nimbus 7 ERB and radiation data

The scanning channels of the Nimbus 7 ERB instrument were designed primarily to help determine the outgoing visible and infrared fluxes from the top of the Earth's atmosphere on a horizontal scale of about 150 km. On any given day, the instrument would measure the radiance leaving a given region of the Earth from only a few angles. Thus to retrieve the flux (irradiance) leaving any region, an angular distribution model appropriate to the target would have to be employed. This provided the second major purpose of the scanning channels: to develop angular distribution models for outgoing visible and infrared radiation for a suitably diverse range of targets. The scanners operated successfully from November 16, 1978 through June 22, 1980. Some earth radiation budget results for this time period (Jacobowitz, et al., 1984a) and early developments of

angular distribution models (Taylor and Stowe, 1984) have been published.

I will now briefly describe the ERB scanner instrument. For detailed descriptions of the ERB hardware and data acquisition see Jacobowitz, et al. (1978) or Jacobowitz, et al. (1984b). The ERB scanners consist of 4 small coplanar telescopes (in a fan-shaped array), each possessing both infrared and visible optical systems. The instantaneous field of view (IFOV) of each scanner is 0.25° by 5.12°. Pyroelectric detectors (with nearly flat spectral sensitivity and linear reponse) were used for both the visible and infrared. The visible channels covered 0.2 μm to 4.8 μm and the infrared channels covered 4.5 μm to 50 μm. Noise equivalent radiance for the shortwave channels was 0.37 W m^{-2} sr^{-1} and 0.18 W m^{-2} sr^{-1} for the longwave channels. Sensitivity variations throughout the duration of the experiment were about ±1%.

The scanners were gimbal mounted and thus could be rotated around two axes. They were scanned vertically by a stepper motor in steps of 0.25° and horizontally in steps of 0.5°. Data was recorded at ½ second intervals (integrating the measurements during each ½ sec scan). The scan pattern of a single vertical scan is shown in Figure 2.1. Both short and long scans were used in various combinations. The long scan goes beyond the Earth's horizon (at 60.4° from the nadir). Five different scan modes (combinations of forward, backward, and side scans of long or short lengths) were used

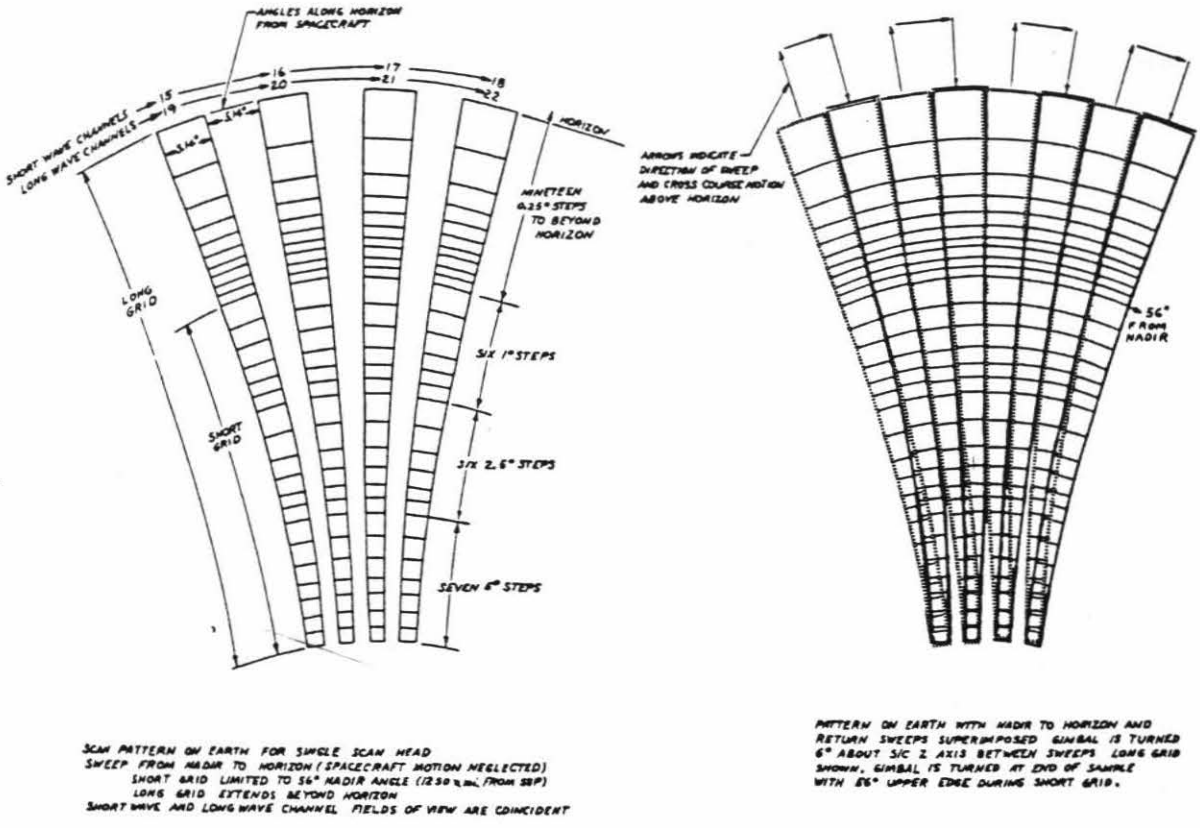

Figure 2.1 A single vertical scan (and its return) of the ERB scanner head (from Jacobowitz et al., 1984b, p. 5026).

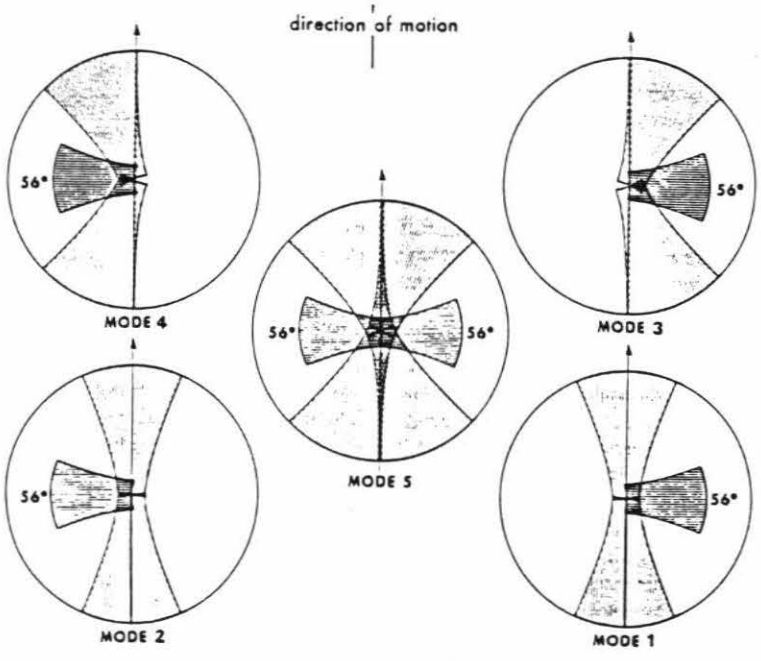

Figure 2.2 The various modes of succesive scans used by the ERB scanning instrument (from Jacobowitz et al., 1984b, p. 5027).

(see Figure 2.2). Scan modes 1 through 4 optimized the angular coverage of those geographical targets (regions of the earth's surface and atmosphere) that were viewed at the expense of geographical coverage. Scan mode 5 optimized geographical coverage at the expense of the angular coverage of the targets measured. In one of the first four modes the scan pattern is repeated every 112 s (or 700 km on the sub-spacecraft track) and in mode 5 the pattern repeats every 224 s (or 1400 km along track). Mode 5 was the standard mode of operation.

In this investigation I used the ERB scanner data on the Sub Target Radiance Tapes (STRT). These tapes are described more fully in Stowe, et al. (1980). Each tape contains all the ERB scanner measurements for each of the 18,630 sub target areas on the earth for a given day (defined in GMT). A sub target area (STA) is roughly a square region of the earth's surface 1.5° in latitude (167 km) by about 167 km in longitude (varying from 1.5° at the equator to 40° at the poles). The record for each STA includes (for each measurement) the infrared radiance (W m^{-2} sr^{-1}), visible radiance (W m^{-2} sr^{-1}), time (GMT), observer zenith angle, azimuth angle between sun and observer, and fraction (in 9^{th}s) of the scanner IFOV that fell inside the STA. The measurements are grouped by the orbital pass on which they were taken. For each orbital pass the range and mean of the solar zenith angle for the STA are listed. One should note that the theoretical maximum range for the solar zenith

angle for a given STA during a single orbital pass is 4.3°. In practice the range is much less.

II.B) Nimbus 7 THIR and cloud cover

The Temperature Humidity Infrared Radiometer (THIR) on board Nimbus 7 is a two channel scanning radiometer whose output is useful for the determination of cloud cover, emitting surface temperature, and atmospheric water. Although on earlier Nimbus satellites THIR served a research purpose, on Nimbus 7 it was included to support the other experiments. THIR consists of an optical scanner whose beam is divided into two channels, a 10.5 μm to 12.5 μm window channel and a 6.5 μm to 7.0 μm water vapor channel. The ground resolution (IFOV) at the nadir for the 11.5 μm channel is 7 km and for the 6.7 μm channel it is 20 km. A more detailed description of the instrument is in Cherrix (1978).

The group led by Larry L. Stowe of NOAA/NESDIS has taken the THIR data for the time in which the ERB scanner was working and determined fractional area cloud coverages (for high clouds, medium altitude clouds, low clouds, and clear areas) and various statistical flags and included all this data on the STRTs (Stowe, et al., 1978 and Chen, et al., 1980). The brightness temperature in each IFOV was converted into a physical temperature (by correcting for atmospheric attenuation). Fractional cloud coverage in each STA was determined by allocating all IFOVs in a sub target

area to each of four categories: surface, low cloud (cloud with tops below 2 km altitude), mid level cloud (cloud tops 2 km to 7 km in the tropics, 2 km to 6 km in mid-latitudes, and 2 km to 4 km in polar regions), and high cloud (cloud tops above the mid level cloud limits). Monthly mean atmospheric temperature profiles from NCAR (Jenne, et al., 1974 and Crutcher and Meserve, 1970) were used to establish the boundaries between these categories in terms of temperature.

In addition to the fractional area cloud coverages, various binary flags were included in the STRT records. Some flags indicated possible ambiguities in cloud level identification. These flags were ignored in this investigation because I wished to use as much data as possible. Other flags indicated (based on statistical analysis of the THIR data) the presence of cumulus clouds and of broken stratus. I ignored these flags because none of these flags indicated anything physically meaningful (L. Stowe, personal communication, 1982). One flag was included to indicate that measured temperatures in the high cloud category were so low as to indicate that the high clouds were made of ice, rather than liquid water. I used this flag in my analysis.

II.C) The FGGE Level III-b data set from ECMWF and weather variables

One of the major reasons the ERB scanner data set is so important for weather-radiation-climate studies is the existence of the contemporary FGGE data set. From December 1978 to December 1979 the nations of the world cooperated in the First GARP Global Experiment (FGGE). An expanded network of surface and upper air weather stations provided more numerous, accurate, and standardized conventional weather data than had been available before. A global network of five geostationary satellites provided cloud track winds. A new generation of American polar orbiting weather satellites (TIROS-N and NOAA-6) provided more and better temperature and humidity soundings. Finally, a large number of special platforms (including long-lived ballons, weather ships, weather instruments on commercial airliners, dropwindsondes, and weather buoys at sea) were deployed to gather conventional weather data in sparsely populated regions (especially over southern and tropical oceans). The most intensive and extensive coverage occurred during two Special Observing Periods (SOP), each lasting two months. Most of the data I analyzed covered a period of time during the second SOP (during mid-June).

The various data sets were averaged and interpolated by 4-dimensional assimilation into global weather prediction models to produce global weather analyses. The resulting global analyses are called the FGGE Level III-b data set.

Two versions were produced, one at the European Center for Medium-range Weather Forecasting (ECMWF) and the other in the United States. I used the ECMWF version because the other was yet not available when I began this project.

The ECMWF Level III-b FGGE data set is described in Bengtsson, et al. (1982b). The ECMWF model predicts temperature, horizontal winds, absolute humidity, and surface pressure on a regular (1.875° latitude by 1.875° longitude) grid at 15 (non-uniformly spaced) vertical levels in sigma ($\sigma = p/p_{surface}$) coordinates. Data were assimilated every 6 hours (±3 hour windows). The 6 hour prediction based on the previous analysis was used as the first-guess starting point for a given analysis. The analyses were produced in pressure coordinates and the winds were analyzed on the same gridpoints as the other variables. The model predicted u and v at gridpoints midway between the gridpoints for T, p_s, and q. Moreover analyses used heights and thicknesses rather than temperatures as variables. Thus, in order to produce each first guess analysis, the prediction needed to be converted to analysis variables and coordinates, using interpolation by cubic splines. Observations were then used to correct the variables at the gridpoints through optimum interpolation. Weights were assigned to various types of observations and predictions based on their error characteristics. These weights were then used, along with data taken during the 6 hour window, to determine the corrections to the first-guess (predicted)

variables. In order to assimilate the new data in a meteorologically realistic way, the weighting factors cause the correction factors to be locally non-divergent and approximately geostrophic at high latitudes. In order to eliminate contamination of the data by gravity waves, a non-linear normal mode initialization is used. In this technique, the initial change of gravity wave modes is set equal to zero. Supposedly, all this creates no problems except to partially suppress Hadley circulation and create some errors in the vertical profiles in the tropics. A far more detailed description of the analysis scheme is found in Lorenc (1981).

In the ECMWF scheme, an analysis is produced for every 6 hours. Throughout FGGE, every other analysis is stored on tape (an analysis at 00 GMT and 12 GMT every day). During each SOP, every analysis was archived. The data archived for each horizontal gridpoint in each analysis is listed in Table 2.1.

II.D) Geographic data on the STR and RAND/SIO tapes

The STR tapes include data on the nature of the earth's surface in each target area and each sub-target area (in addition to the ERB and THIR data). There is one so-called "topography" record per TA and one "geography" record per STA on each STRT. Each topography record (see Stowe, et al., 1980) specifies the fraction of each TA containing:

1) water and permanent ice for each of four seasons

2) six other surface configurations:

   plains

   hilly uplands and plateaus

   mountains

   hamada desert

   erg desert

   mountain and bolson desert

3) nine vegetation classifications:

   mountain vegetation

   selva (rain forest)

   scrub forest

   taiga (high latitude coniferous forest)

   mixed mid-latitude forest

   savannah (tropical grassland)

   prairie (mid-latitude grassland or steppe)

   tundra

   desert.

These data were obtained by hand analysis of maps from an ordinary atlas (James, 1951). Each geography record contains the fraction of land, water, snow, and ice in each STA within 24 hours of the ERB measurements (Stowe, et al., 1980). In addition, data on snow depth and age of snow and ice are given. These were obtained from Air Force nephanalysis tapes, which archive data on snow and ice (including sea ice) each day (at 00 hours GMT) on a global grid with 40 km resolution.

In addition to the data on the STRTs, I used surface elevation data off the Topographic Data tape from the National Geophysical and Solar-Terrestrial Data Center. This tape includes (along with other topographic data sets) the RAND/SIO Global Topography, a file of surface elevations over the entire Earth at a resolution of 1° of latitude and longitude. W. L. Gates and A. B. Nelson (both of Rand Corporation at that time) published this as a topographic report for the Defense Advanced Research Projects Agency in 1973. Depths (below sea level) for ocean areas were obtained from measurements made at Scripps Institution of Oceanography. Elevations above sea level (for land areas, ice caps, and regions of sea ice) were determined by visual estimations of contour charts. For ocean areas not covered by sea ice, I used an elevation of 0 meters above sea level.

Chapter 3

METHOD OF DATA ANALYSIS

In this chapter I explain how I took radiance (not flux) data, standard meteorological data, cloudiness data, and information about the Earth's surface geography and derived linear analyses of flux, weather variables of physical relevance to cloud-radiation studies, cloudiness, and surface albedo.

III.A) Turning an analysis of radiances into an analysis of flux

I am not the first to attempt to determine the relationship between out going radiative flux, cloudiness, and weather. A fine example of a cloud-radiation study is Hartmann and Short (1980), and two excellent studies of radiation-weather relationships are Jensenius, et al. (1978) and Linder et al. (1981). I believe my analysis is superior to these and other old analyses in three main ways. First, I have global weather data of relatively high quality due to my use of ERB data during a FGGE SOP. Previous analyses have been restricted in their geographic scope and had to suffer less reliable weather data. Second, the ERB scanner data have resolution sufficient to resolve synoptic scale weather (and cloud) systems (just as data from the cloud imaging systems on our conventional weather satellites do), yet they retain the broad spectral coverage and high

accuracy of the traditional low resolution ERB instruments. Third, and most important in the development of this thesis, my analyses include resolved radiance data from all portions of the hemisphere of upward going flux.

For any given target (on the Earth) at any given time, I have available only a limited set of radiance data. These data do not cover all of the upper hemisphere for the target. Therefore, I used larger (and fewer) angular bins. Figure 3.1 gives an idea of the distribution of radiance data (in the upward hemisphere) acquired during daylight hours (solar zenith angle less than 85 degrees) by the Nimbus 7 satellite for several typical target areas (regions 500 km on a side). Note that in these diagrams the upward hemisphere has been folded about the plane including the sun. This has been done for reasons of symmetry which will be explained below. For any target outside the higher latitudes, Nimbus 7 acquires daylight ERB data on, at most, two overflights a day. In the figure, each overflight acquires an arc of data (part of which may be reflected at the lower boundary of the plot). Where there are two arcs of data, there were two overflights of Nimbus 7 which acquired data for the target area during that day. Even in those cases having two arcs, the upward hemisphere is clearly not completely sampled. However, I can take analyses of radiance data of this sort and correlative (cloud and weather) data and derive relationships between

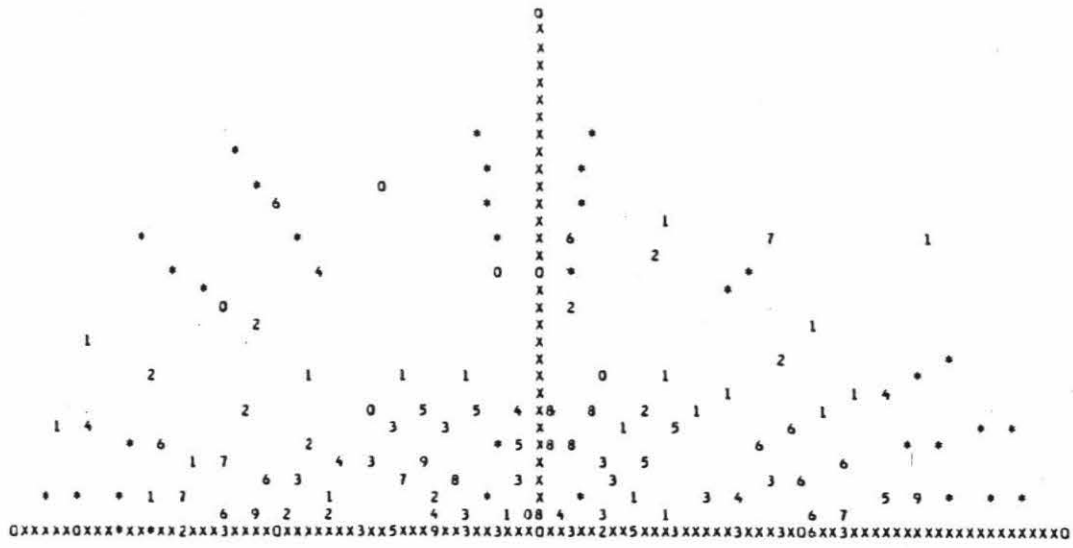

(a.) 60.75° S, 121.5° E

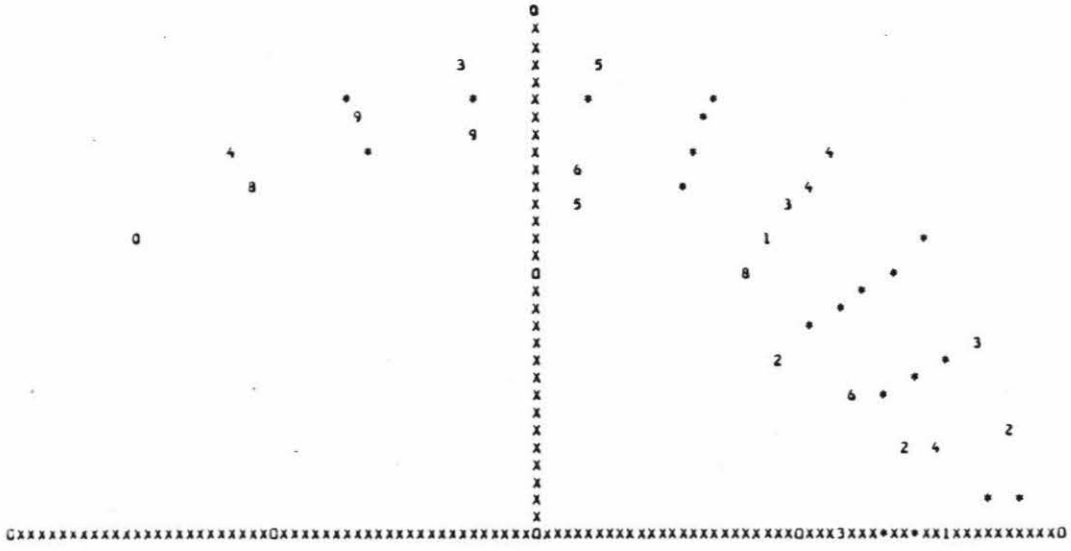

(b.) 11.25° S, 92.25° E

Figure 3.1 The angular distribution of ERB scanner data acquired in the sunlit portion of November 28, 1978 in various individual target areas.

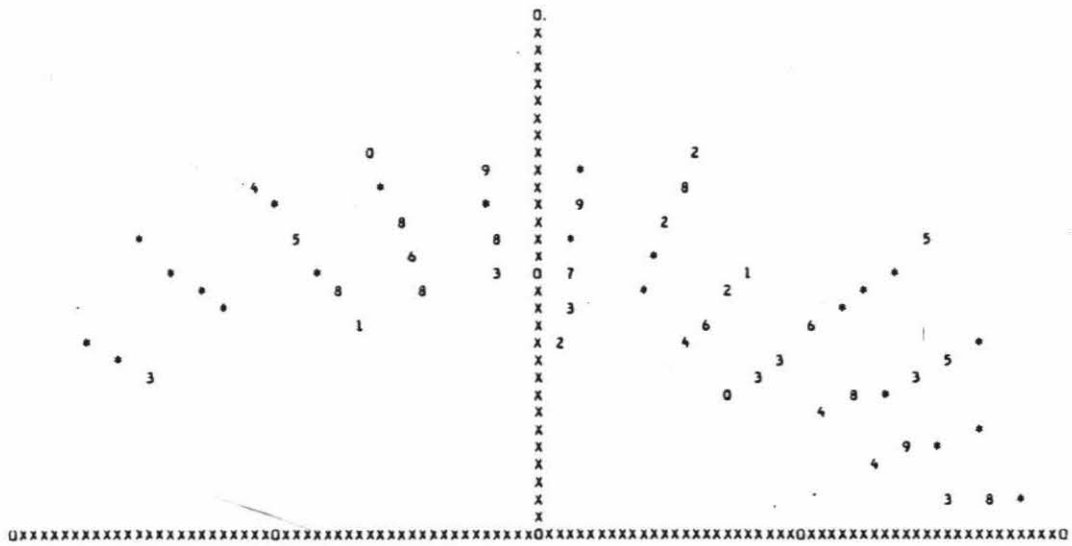

(c.) 38.25° N, 27° W

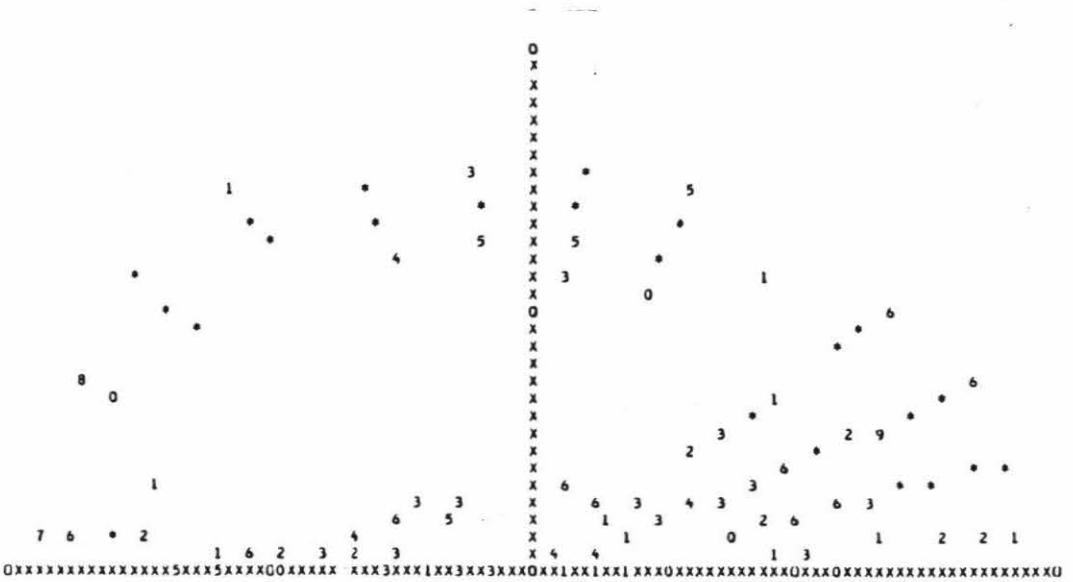

(d.) 56.25° N, 180° W

Figure 3.1 (cont.)

the full hemispheric flux and the correlative data while making very few assumptions as follows.

Let $R[\theta,\phi,\theta_\odot(t)]$ be the radiance (reflected visible or emitted infrared) leaving a portion of the Earth, at a zenith angle of θ, a relative azimuth angle (between the sun and the emission direction) of ϕ, when the solar zenith angle is $\theta_\odot$, at a time t. See Figure 3.2 for an explanation of the coordinates. Then the flux is given by

$$F(t) = \int_{\theta=0}^{\pi/2} \int_{\phi=0}^{2\pi} R[\theta,\phi,\theta_\odot(t)] \cos\theta \sin\theta \, d\theta \, d\phi. \quad (3.1)$$

If we divide the upward hemisphere into a series of angular bins, we can descretize this equation. We get

$$F(t) = \sum_i R_i(\theta_\odot(t)) \, \mu_i \, \Delta\Omega_i, \quad (3.2)$$

where x_i is the value of x in the angular bin i (defined by the angles θ_i, ϕ_i), $\mu_i = \cos\theta_i$, and $\Delta\Omega_i = \sin\theta_i \, \Delta\theta_i \, \Delta\phi_i$. Now let σ_x^2 be the variance of x, let σ_{xy} be the covariance of x and y, and let $\langle x \rangle$ be the ensemble average of x. Then

$$\begin{aligned}
\sigma_{xF} &= \langle x F \rangle - \langle x \rangle \langle F \rangle \\
&= \Big\langle \sum_i x \, R_i(\theta_\odot(t)) \, \mu_i \, \Delta\Omega_i \Big\rangle \\
&\quad - \langle x \rangle \Big\langle \sum_i R_i(\theta_\odot(t)) \, \mu_i \, \Delta\Omega_i \Big\rangle \\
&= \sum_i \mu_i \, \Delta\Omega_i \, [\langle x \, R_i(\theta_\odot(t)) \rangle - \langle x \rangle \langle R_i(\theta_\odot(t)) \rangle] \\
&= \sum_i \mu_i \, \Delta\Omega_i \, \sigma_{xR_i}. \quad (3.3)
\end{aligned}$$

The various scalar variables I used in this investigation, which are represented in equation 3.3 as x, are listed in

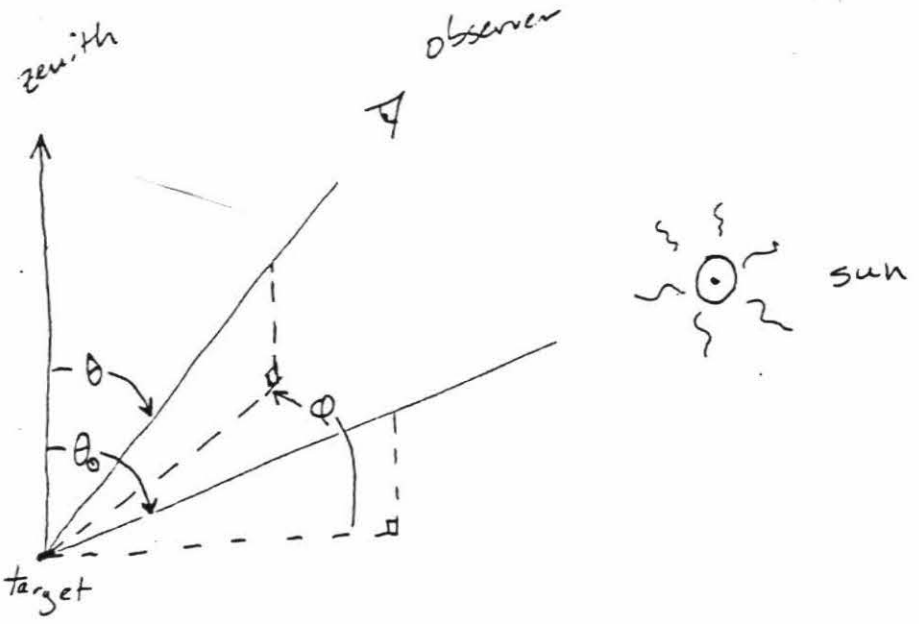

Figure 3.2 Explanation of the angular coordinates.

Table 4.1 and described in Chapter 4. Furthermore, it is simple to show that

$$\sigma_F^2 = \sum_i \sum_j u_i \, \Delta\Omega_i \, u_j \, \Delta\Omega_j \, \sigma_{R_i R_j}, \tag{3.4}$$

and that

$$\sigma_{FF} = \sum_k \sum_i u_k \, \Delta\Omega_k \, u_i \, \Delta\Omega_i \, \sigma_{R_k R_i}, \tag{3.5}$$

where italics in equation 3.5 are used for infrared flux and radiances and normal letters are used for visible data, and i and k are indices for visible and infrared radiances, respectively. Moreover,

$$\langle F \rangle = \sum_i \langle R_i \rangle \, u_i \, \Delta\Omega_i. \tag{3.6}$$

In order to use equations 3.3 - 3.6 to estimate the statistical characteristics of radiative flux, one needs a data set having a large random sample of radiances from all angular bins, including many pairs of measurements from each combination of angular bins. In other words, for any bin i, one needs many measurements of the radiance emerging from bin j that were taken at the same time that a measurement of the radiance from bin i was taken, for all bins j (covering the entire upward hemisphere). Although I did not have available radiance data covering the entire upward hemisphere for any one target (of reasonable size and duration), I did have available enough data of different distributions about the upward hemisphere that I could estimate the characteristics of the entire outgoing flux (both infrared and visible) in a statistical sense.

Previous empirical studies of cloud-radiation relationships, when using data of high spatial resolution, have generally taken individual radiance measurements and immediately converted them into values of the emerging flux at the top of the atmosphere. A number of biases can creep into the analysis this way. Even when Nimbus 7 ERB scanner data are being used this is not necessarily a wise technique. Arking and Vemury (1984) and Vemury et al. (1984) have analyzed and discussed the problems with just such types of analysis. By determining the statistics of individual radiances and only then turning these statistics into flux statistics, I avoid these problems entirely.

III.B) Dividing the upward hemisphere into discrete bins

Radiances on the STR tapes are classified as emanating from one of 419 angular bins in the upward hemisphere. If I were to use these bins in order I would be unable to determine the covariances of each radiance with all other radiances (other angular bins). Therefore, I used larger (and fewer) angular bins. In Figure 3.3, I show the boundaries of some of the angular bin patterns that I used.

The first modification I made in the STRT bin "map" was to reflect the upward hemisphere about a vertical plane that includes the vector to the sun. Thus any spot in the upward hemisphere fell into the same angular bin as that spot on the opposite side of this plane. For one thing, most reflection surface types in their pure form (e.g., total

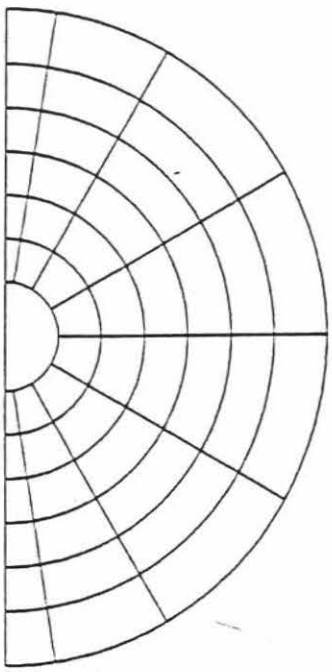

(a.) 49 visible bin map
Stowe-Taylor pattern

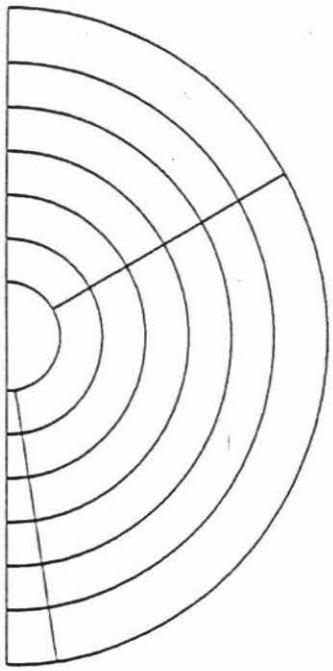

(b.) 19 visible bin map
collapsed version of (a.)

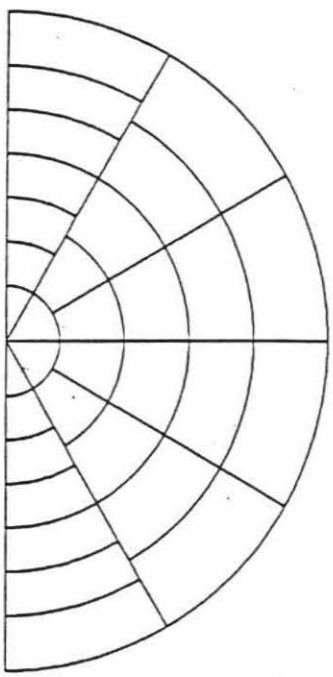

(c.) 32 visible bin map
my alternate pattern

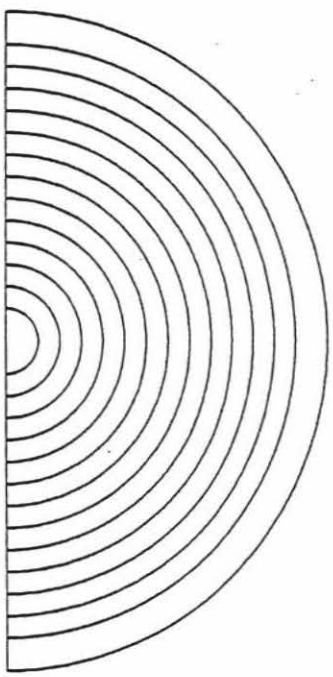

(d.) 14 infrared bin map

Figure 3.3 Maps of the angular bins used in the various analyses explained in the text. In each map, $\phi = 0$ at the top.

cloud cover at medium altitudes or tropical lowland rain forests with completely clear skies) have no preferred azimuth except that pointing toward their source of illumination (in this case, the sun). The most complicated surfaces (e.g., scattered clouds at various altitudes over mountainous, forested islands in the ocean) also have no preferred azimuth in the absence of illumination. For such surfaces (the simplest and the most complicated) using only one half of the upward hemisphere is quite reasonable, on theoretical grounds. There do exist reflector types, however, which do have a preferred azimuth other than the sun direction. Two obvious examples are linear mountain chains and cloud "streets" (lines of convective clouds separated by lines with no cloud cover, which are parallel to the wind in the lower troposphere, commonly found in the trade wind latitudes and in the lee of polar fronts). However, in order to model the effect of the innate anisotropies of such reflectors successfully, I would need to know the orientation of these reflectors relative to the satellite, data which is difficult to find even when available. Furthermore, I would have to use separate angular bins, not only for observer zenith angle and azimuth relative to the sun, but also for the relative azimuth between the reflector anisotropy and the observer (or else the sun). This is a much too difficult task for the scope of this investigation, especially for a condition which is far from ubiquitous and does not have an overwhelming impact

on the reflection of sunlight from the Earth (the way that the solar zenith angle or observer zenith angle do, for example).

The second modification I made in the angular bin map was to enlarge the size of the bins. You may note that in the bin maps in Figure 3.3 there are far fewer than the 225 you might expect in half the upward hemisphere. For analysis of infrared radiation, relative azimuth between the observer and the sun, was deemed to be unimportant. Thus in Fig. 3.3.a one finds that there are only 14 angular bins, divided by zenith angle only. For analysis of visible radiation, the relative azimuth was obviously important. However, the importance of different specific angular bin patterns on my analysis of the radiation was unknown when I began this project. Therefore, I used three different bin maps for my analyses. These are presented in Figs. 3.3.b-3.3.d.

III.C) The diurnal coverage problem and its solution

The method of statistical analysis that I presented in the first section of this chapter would be of interest to climate studies if the radiation measurements I was dealing with were either diurnal averages of the emitted (or reflected) radiance or if they were instantaneous radiances that were distributed randomly over the day. Unfortunately, neither possibility proves to be the case. The Nimbus 7 satellite travelled in a sun-synchronous orbit with noon and

midnight equator crossings. For the infrared measurements, the situation is not so bad. The data set included measurements which were near to the extrema of the diurnal radiative emission cycle (which usually peaks in the early afternoon and reaches its nadir just before dawn). The result of using all the infrared data should give nearly diurnal averages of the radiance ensemble averages and covariances. Things are much worse for the visible data. Not only were the measurements unevenly distributed over the daylight hours, but they were concentrated at an extremum, the maximum solar zenith angle, for most targets on earth. For this reason, I converted the visible radiance data from the STRTs into diurnally averaged radiances by applying various diurnal corrections.

In order to convert the STRT data by applying diurnal corrections, I need to assume that the nature of the surface atmosphere ensemble (the "scene" observed by the Nimbus 7 ERB scanner) does not change during the hours of daylight. In other words, the albedo does not change due to a change in cloudiness or sea ice or snow cover during the daylight hours of a single day. Thus, the only reason that a noontime measurement of albedo would not be representative of the diurnal average is due to the change of albedo of a scene associated with the change in solar zenith angle. My analysis should also work if I have a big enough sample and there is no <u>systematic</u> change in scene with time (during the daylight hours) for the various targets in my sample.

Except for the development of convective storms (and their associated clouds) during the afternoon over the Midwestern U.S. in the summer, I know of no systematic changes in scene type over the daylight hours which occurs in a large region of the Earth.

To derive the diurnal correction factor we first define the bidirectional reflectance (a function telling the albedo in a given direction for illumination from another given direction). The BDRF (bidirectional reflectance function), A, is defined by

$$R(\theta,\phi,\mu_\odot(t)) = \mu_\odot(t)\ A(\theta,\phi,\mu_\odot(t))\ F_\odot \qquad (3.7)$$

or

$$R_i(t) = \mu_\odot(t)\ A_i(t)\ F_\odot. \qquad (3.8)$$

Then if $\overline{x}$ is the diurnal average of x, we have,

$$\overline{R_i} = \overline{\mu_\odot\ A_i}\ F_\odot \qquad (3.9)$$

and

$$\overline{F} = \sum_i \overline{R_i}\ \mu_i\ \Delta\Omega_i. \qquad (3.10)$$

If we have some idea of how A_i varies with $\mu_\odot$ we should be able to determine the diurnal averages given only the instantaneous measurements of radiance and the solar zenith angle at the time of each measurement.

Larry Stowe and V. Ray Taylor, using the information archived on the STRTs that they helped write, developed "angular distribution models" (ADMs), actually discretized bidirectional reflectance functions, for various surface-atmosphere ensembles (see Taylor and Stowe, 1984). Models were developed for pure surfaces (clear atmosphere over

ocean, land, snow, and ice), for pure forms of clouds (total cover of low, mid-altitude, high ice, and high water clouds), for mixed clouds (total cover of mixed clouds over land and over ocean), and for partial cover of mixed clouds (40% - 60% cover of mixed clouds over land and over ocean). These 12 models were derived from data on STRTs for 66 days in 1978 and 1979. For each of the 12 models, data were averaged in 49 angular bins of the upward hemisphere (defined by observer zenith angle and relative azimuth) and 10 bins of solar zenith angle (each bin 0.1 wide in cosine of s.z.a.). Taylor and Stowe classified observations by the cloudiness observed and the type of surface known to be underneath, and they chose only the best data (in terms of the amount and quality of cloudiness data, especially). Thus they were able to average together data from vastly different regions (and most importantly, latitudes) of the Earth. The result was to cover most of the range of solar zenith angles for the various models. Some of the data from these models are presented in Figure 3.4. In each part of Figure 3.4 the albedo of each of the 12 surface-atmosphere ensembles (models) in one angular bin is plotted versus cosine of the solar zenith angle. The purpose of this figure is to convince you that the way in which the reflectivities of the various surface-atmosphere ensembles behave versus solar zenith angle are, to a certain extent, independent of the sort of surface-atmosphere ensemble being observed. Therefore, I feel that the effect of solar zenith

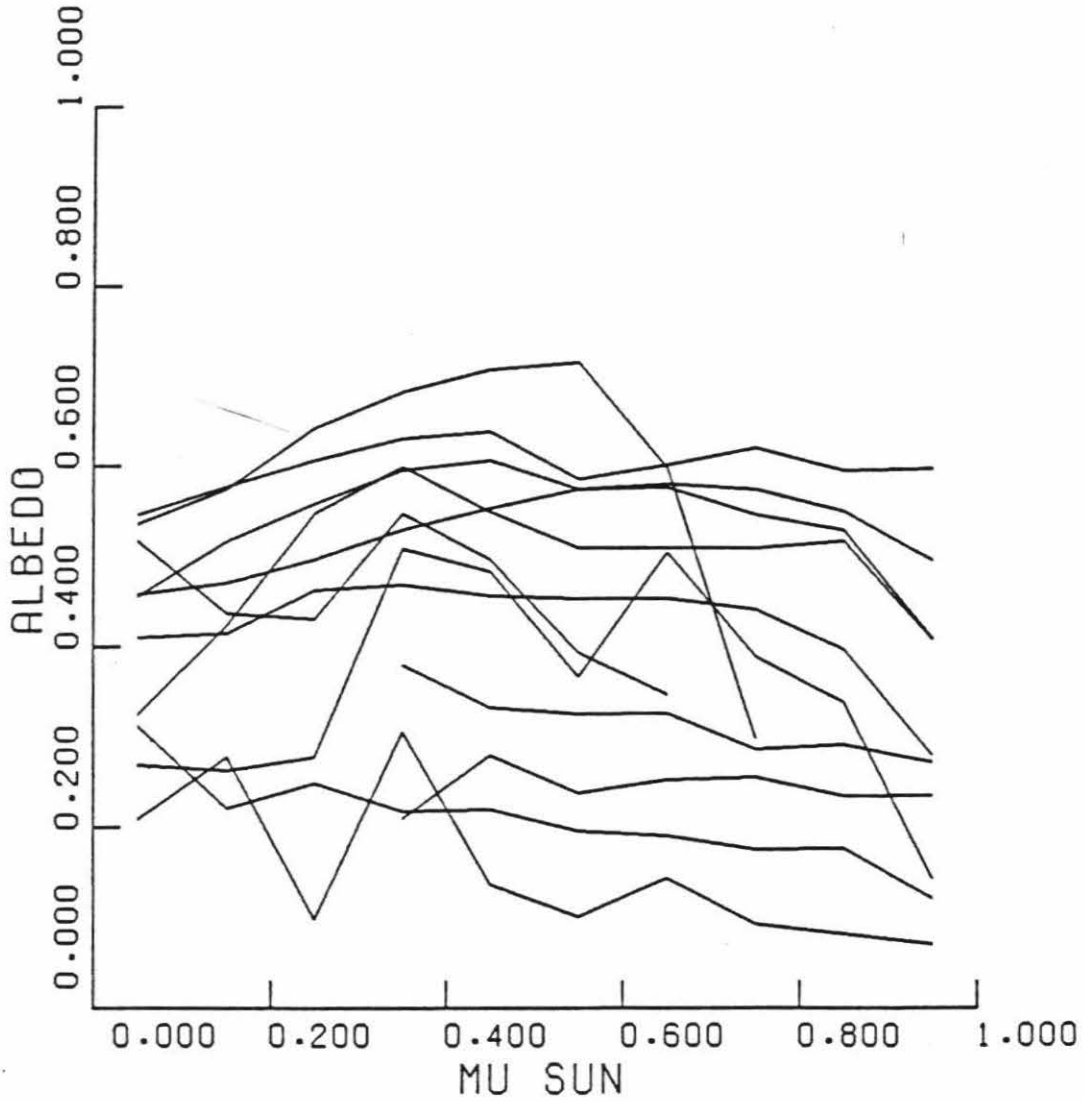

(a.) θ = 27° - 19°, ϕ = 0° - 9°

Figure 3.4 Bidirectional reflectance ("albedo") vs. cosine of the solar zenith angle for the 12 sorts of surface-atmosphere ensembles investigated by Taylor and Stowe (1984) for two angular bins.

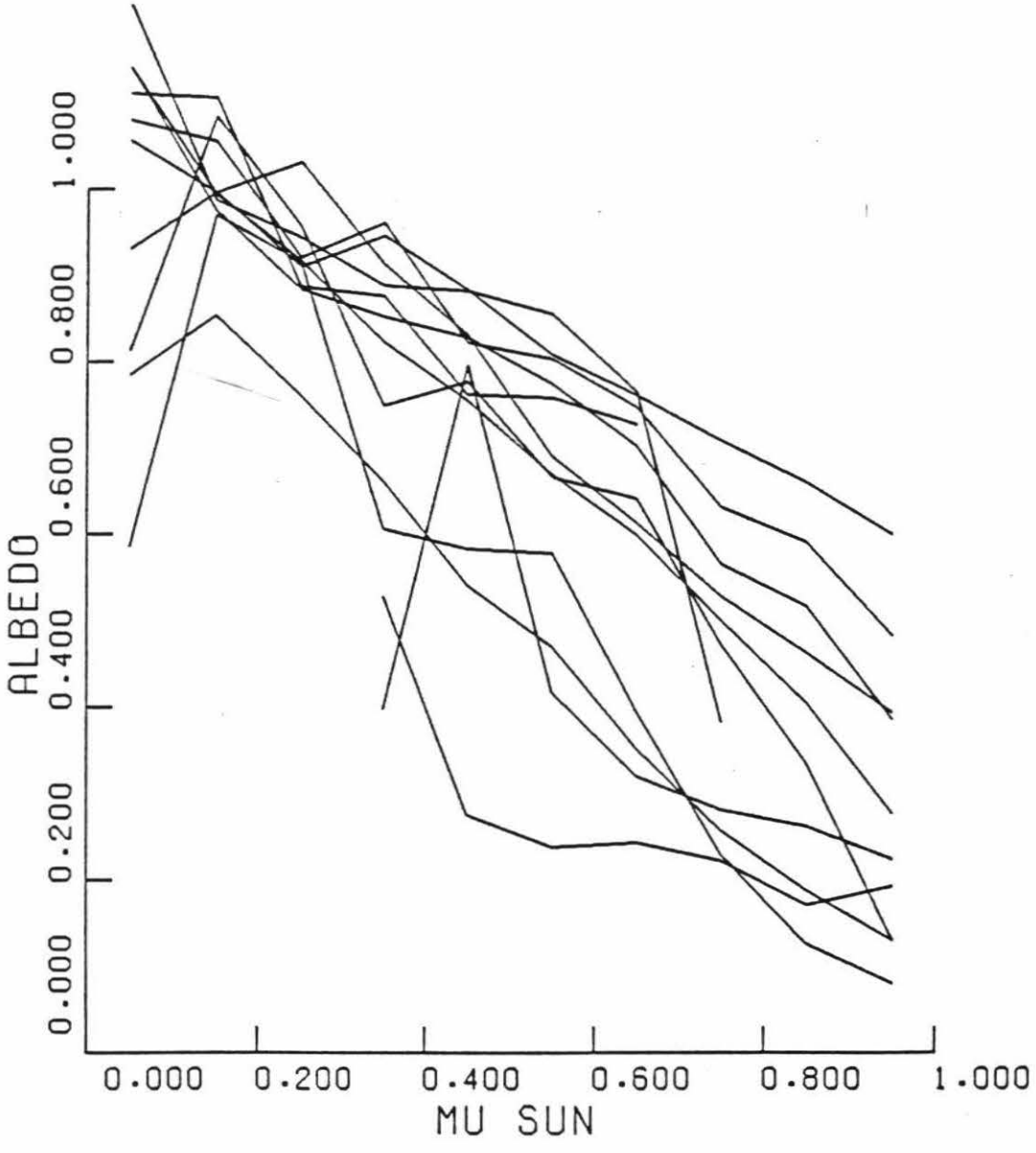

(b.) θ = 51° - 63°, ϕ = 171° - 180°

Figure 3.4 (cont.)

angle on albedo can be separated from the effect of the sort of ensemble being observed. In short, we can perform a separation of variables in our bidirectional reflectance functions. I have modeled these functions (the Taylor-Stowe models) in three ways: (a.) the constant albedo model, (b.) the additive albedo model, and (c.) the multiplicative albedo model. Note that each of the three models is used to model the albedo in each of the 49 angular bins separately. These models are explained in the following three subsections.

(a.) The constant albedo model

In this model, I assume that the albedo in a given bin is independent of the solar zenith angle (obviously wrong from a perusal of Figure 3.4, but a good place to start the investigation). Therefore, the albedo depends only on the sort of scene (surface-atmosphere ensemble) being observed. Thus,

$$A_i(t) = A_i(\mu_\odot(t), s) = g_i(s), \qquad (3.11)$$

where s signifies a suite of variables specifying scene type. From equations 3.8, 3.9, and 3.11 we get,

$$R_i(t) = \mu_\odot(t)\, g_i(s)\, F_\odot \qquad (3.12)$$

and

$$\overline{R_i} = \overline{\mu_\odot}\, g_i(s)\, F_\odot, \qquad (3.13)$$

where we have assumed (as explained above) that the scene type does not change during the daylight hours of a single

day. From equation 3.12 it is clear that we can express $g_i(s)$ in terms of the instantaneous radiance measurement,

$$g_i(s) = \frac{R_i(t)}{\mu_\odot(t)\ F_\odot}. \qquad (3.14)$$

We can now express the diurnally averaged radiance in terms of the instantaneous (measured) radiance and other known quantities,

$$\overline{R_i} = R_i(t)\ \frac{\overline{\mu_\odot}}{\mu_\odot(t)}. \qquad (3.15)$$

Note that, using equation 3.15, one can determine the diurnally averaged radiance from a target from knowledge of the instantaneous radiance and geometry (the location of the sun, the latitude, and the time of year). No a priori knowledge of the sort of scene being observed is needed. It was one of my primary goals in this thesis to do linear analyses of radiance without using special knowledge, thereby allowing me to use all of the available ERB data.

(b.) The additive albedo model

In this model, I assume that the bidirectional reflectance function can be separated into two functions, one dependant on the cosine of the solar zenith angle, and the other dependant on the scene type. The sum of these functions is the BDRF. Thus,

$$\begin{aligned} A_i(t) &= A_i(\mu_\odot(t), s) \\ &= g_i(s) + h_i(\mu_\odot). \end{aligned} \qquad (3.16)$$

In a manner similar to that used for the constant albedo model, using equations 3.8, 3.9, and 3.16, we can show that,

$$\overline{R_i} = R_i(t) \frac{\overline{u_\odot}}{u_\odot(t)} - F_\odot \, \overline{u_\odot} \, h_i(u_\odot(t)) + F_\odot \, \overline{u_\odot \, h_i}. \qquad (3.17)$$

Beyond the instantaneous radiance measurement and geometric data, the only information we need to determine the diurnally averaged radiance is knowledge of how reflectance varies with solar zenith angle, in general. This knowledge is embodied in the model function $h_i(u_\odot(t))$. I present the method I used to determine these h functions from the Stowe-Taylor data ("models") later in this chapter.

(c.) The multiplicative albedo model

In the multiplicative model, I assume much the same as with the additive model, except that the separable functions are multiplied to determine the bidirectional reflectance. Therefore, we use,

$$A_i(t) = A_i(u_\odot(t), s) = f_i(u_\odot) \, g_i(s). \qquad (3.18)$$

Once again, using equations 3.8, 3.9, and 3.18, we can show that,

$$\overline{R_i} = R_i(t) \frac{\overline{u_\odot \, f_i}}{u_\odot(t) \, f_i(u_\odot(t))}. \qquad (3.19)$$

To determine the diurnally averaged radiance using this model requires no more information than using the additive model. The only difference is the sort of model used to

simulate the effect of varying solar zenith angles throughout the day.

III.D) Calculation of the diurnal correction factors

(a.) Determining the diurnal average of $\mu_\odot$

If we let λ be the latitude of a point on Earth, τ be the time angle (angle in longitude from the midnight meridian) of the same point, and $\lambda_\odot$ be the declination of the sun (latitude of the sub-solar point on the Earth), then the cosine of the solar zenith angle is given by

$$\mu_\odot = \sin \lambda_\odot \sin \lambda - \cos \tau \cos \lambda_\odot \cos \lambda. \qquad (3.20)$$

I skip the proof of this because it is long and involved but not particularly difficult. From equation 3.20, we can derive the time of day for sunup and sundown,

$$\tau_u = \cos^{-1} (\tan \lambda_\odot \tan \lambda) \qquad (3.21)$$

and

$$\tau_d = 2\pi - \cos^{-1} (\tan \lambda_\odot \tan \lambda), \qquad (3.22)$$

where we constrain $\cos^{-1} x$ to lie between 0 and π, for all x. Then the diurnal average of the cosine of the solar zenith angle is given by

$$\overline{\mu_\odot} = \frac{1}{2\pi} \left[\int_{\tau=0}^{\tau_u} 0 \, d\tau + \int_{\tau=\tau_u}^{\tau_d} (\sin \lambda_\odot \sin \lambda - \cos \tau \cos \lambda_\odot \cos \lambda) \, d\tau + \int_{\tau=\tau_d}^{2\pi} 0 \, d\tau \right]$$

$$= \frac{1}{\pi} \int_{\tau=\tau_u}^{\pi} (\sin \lambda_\odot \sin \lambda - \cos \tau \cos \lambda_\odot \cos \lambda) \, d\tau$$

$$= [(\pi - \tau_u) \sin \lambda_\odot \sin \lambda + \sin \tau_u \cos \lambda_\odot \cos \lambda] / \pi. \qquad (3.23)$$

Note that for regions of midnight sun (polar summer), rather than using equation 3.21 for τ_u, we simply use the value 0 (since the sun is up at midnight). For regions of noontime darkness (polar winter) we simply use π for the value of τ_u (since the sun is down at noon).

(b.) Determining the g and h factors of the additive model

I used a linear least squares fit of the additive model to the Stowe-Taylor ADMs to determine the model parameters, g and h. If we suppress the subscript i (for angular bin number) equation 3.16 gives us

$$A(u_\odot, s) = h(u_\odot) + g(s)$$

or

$$A_{jk} = h_j + g_k, \qquad (3.24)$$

where $j \in \{1,2,\ldots,12\}$ designates the scene type number and $k \in \{1,2,\ldots,10\}$ designates the cosine of the solar zenith angle bin number. Our model fit minimizes the sum,

$$S = \sum_{j=1}^{10} \sum_{k=1}^{12} \nu_{jk} \, x_j \, y_k \, (A_{jk} - h_j - g_k)^2, \qquad (3.25)$$

where the x_j are weighting factors for the solar zenith angle bins, the y_k are weighting factors for the different scene types, and the ν_{jk} are zero for those combinations of scene type and solar zenith angle for which Stowe and Taylor

had no models and are one for those combinations where they did have models. By minimizing S we get

$$h_j = \left(\sum_{k=1}^{12} \nu_{jk}\, y_k\right)^{-1} \left(\sum_{k=1}^{12} \nu_{jk}\, y_k\, A_{jk} - \sum_{k=1}^{12} \nu_{jk}\, y_k\, g_k\right) \qquad (3.26)$$

and

$$g_k = \left(\sum_{j=1}^{10} \nu_{jk}\, x_j\right)^{-1} \left(\sum_{j=1}^{10} \nu_{jk}\, x_j\, A_{jk} - \sum_{j=1}^{10} \nu_{jk}\, x_j\, h_j\right). \qquad (3.27)$$

We have a degree of freedom in this model which we can use by requiring that

$$\sum_{k=1}^{12} y_k\, g_k = 0.$$

Remembering the definition of ν_{jk}, this means that

$$\sum_{k=1}^{12} \nu_{jk}\, y_k\, g_k = -\sum_{k=1}^{12} (1 - \nu_{jk})\, y_k\, g_k. \qquad (3.28)$$

In order to simplify the solution of equations 3.26 and 3.27, we now define a vector z where $z_i = g_i$ (for $i \leq 12$) and $z_i = h_{i-12}$ (for $i > 12$). Then from equations 3.26-3.28, for $1 \leq i \leq 12$, we get

$$z_i = \left(\sum_{j=1}^{10} \nu_{ji}\, x_j\right)^{-1} \left(\sum_{j=1}^{10} \nu_{ji}\, x_j\, A_{ji} - \sum_{j=1}^{10} \nu_{ji}\, x_j\, z_{j+12}\right) \qquad (3.29)$$

and for $13 \leq i \leq 22$,

$$z_i = \left(\sum_{k=1}^{12} \nu_{i-12,k}\, y_k\right)^{-1} \left[\sum_{k=1}^{12} \nu_{i-12,k}\, y_k\, A_{i-12,k} - \sum_{k=1}^{12} (1 - \nu_{i-12,k})\, y_k\, z_k\right]. \quad (3.30)$$

Equations 3.29 and 3.30 are, in fact, a set of 22 equations, which can be put in vector and matrix form as

$$\underset{\sim}{Z} = \underset{\sim}{C} + \underset{\approx}{B}\, \underset{\sim}{Z}. \quad (3.31)$$

I will not write out the values of the elements of the constant vector C, or the elements of the coefficient matrix B, as these can be determined by comparison of equation 3.31 with equations 3.29 and 3.30. The solution for the z_i (and therefore the g_k and h_j) is then given by

$$\underset{\sim}{Z} = (\underset{\approx}{I} - \underset{\approx}{B})^{-1}\, \underset{\sim}{C}. \quad (3.32)$$

I display the results for a few latitudes, angular bins, and scene types in Figure 3.5, along with the Stowe-Taylor data and the results of the constant and multiplicative models. Even for those angular bins and scene types with the most difficult phase curves, the additive model seems to make a pretty good fit to the data.

(c.) Determining the f and g factors of the multiplicative model

If we suppress the subscript i (for angular bin number) equation 3.18 gives us

$$A(u_\odot, s) = f(u_\odot)\, g(s)$$

or

$$A_{jk} = f_j\, g_k, \quad (3.33)$$

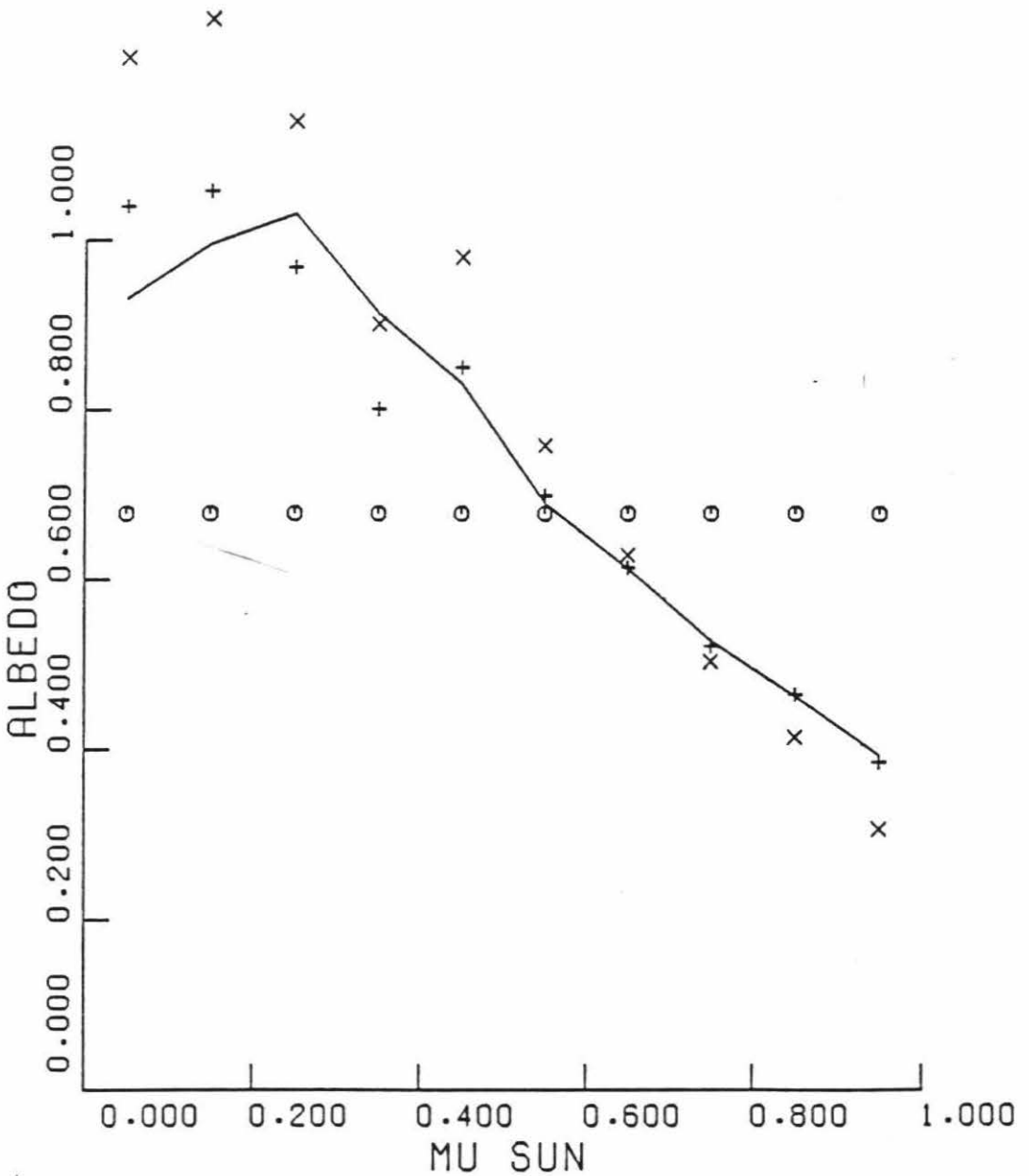

(a.) θ = 51° - 63°, ϕ = 171° - 180°, 50% cloudy over land optimized for latitudes 27° N - 31.5° N

Figure 3.5 Bidirectional reflectance ("albedo") vs. cosine of the solar zenith angle for the data of Taylor and Stowe (1984) and my fits to this data for the three diurnal correction models described in the text. Circles are for the constant model, exes for the multiplicative model, and crosses for the additive model.

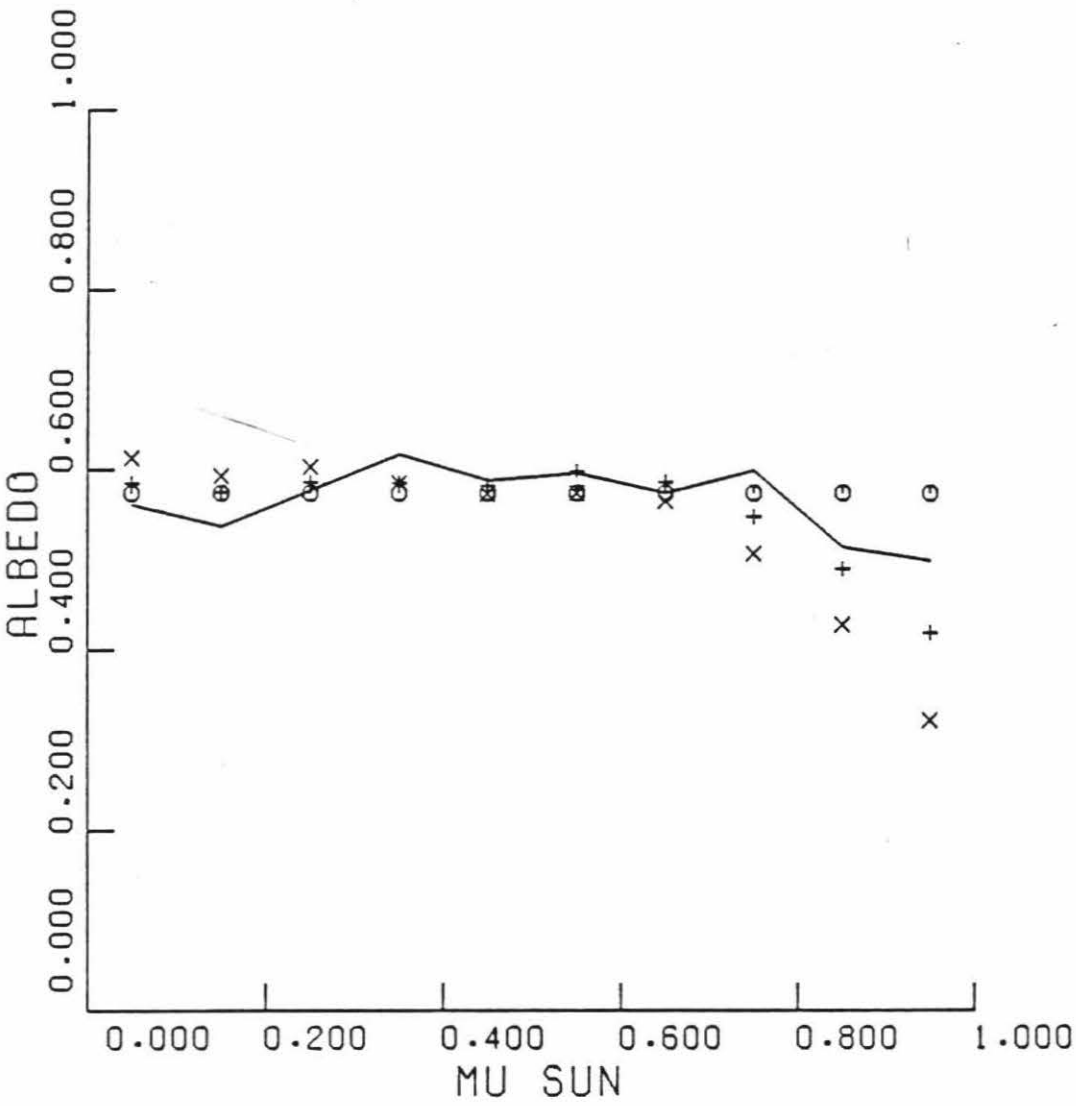

(b.) θ = 39° - 51°, ϕ = 30° - 60°, high water clouds optimized for latitudes 49.5° S - 45° S

Figure 3.5 (cont.)

where the subscripts j and k mean the same things as they did for the additive model. We just define new functions,

$$L_{jk} = \ln A_{jk} = \ln (f_j\, g_k) = \ln f_j + \ln g_k$$
$$= d_j + e_k, \qquad (3.34)$$

where the definitions of L_{jk}, d_j, and e_k are obvious. We solve for d_j and e_k in exactly the same way as we did for h_j and g_k in the additive model. I even used the same values for the weighting factors. Then I simply converted the d_j and e_k into the f_j and g_k for the multiplicative model.

The results are not strictly a linear least squares fit to the Taylor-Stowe data. Rather, they are a sort of log-linear least squares fit. There are two reasons for doing things this way. First, it seemed to me to be a more reasonable way of fitting a multiplicative model to the data. After all, the errors will be multiplicative not additive. Secondly, I was unable to derive a nonlinear least squares fit to the Stowe-Taylor data for this model which would converge with successive approximations.

Some of the results of this multiplicative model are displayed in Figure 3.5. Although this model does not fit the Stowe-Taylor data as well and as often as the additive model, it does a far better job than the constant model.

(d.) Determining the diurnal averages of $\mu_\odot$ times the f and h factors of the additive and multiplicative models

In order to determine the diurnal averages of $\mu_\odot$ times the solar zenith angle (s.z.a.) functions (f and h), I

divided the integrals into steps of 0.1 in $\mu_\odot$. This was done because the Stowe-Taylor data (and therefore the s.z.a. functions) were available only in discrete steps of 0.1 in $\mu_\odot$. We let $\mu_{\odot k} = 0.1\ k$ and let τ_k be the value of τ at which we reach $\mu_{\odot k}$. From equation 3.20, we get

$$\tau_k = \cos^{-1}(\tan \lambda_\odot \tan \lambda - \mu_{\odot k} \sec \lambda_\odot \sec \lambda). \quad (3.35)$$

Now we let q = f or h (the s.z.a. function we are dealing with; note that we have suppressed the index for the angular bin), $q_k = q(\mu_\odot(t))$ where $t_{k-1} \leq t < t_k$, and $n = 10\ \mu_\odot(\text{noon})$ rounded up to the nearest integer (i.e., the number of steps of 0.1 in $\mu_\odot$ during the hours between sunrise and noon in a target area). The diurnal corrections we need are then given by

$$\begin{aligned}
\overline{\mu_\odot\, q} &= \frac{1}{\pi} \int_{\tau=\tau_u}^{\pi} (\sin \lambda_\odot \sin \lambda \\
&\qquad - \cos \tau \cos \lambda_\odot \cos \lambda)\ q(\mu_\odot(\tau))\ d\tau \\
&= \frac{1}{\pi} \sum_{k=1}^{n} \int_{\tau_{k-1}}^{\tau_k} q_k\ (\sin \lambda_\odot \sin \lambda \\
&\qquad - \cos \tau \cos \lambda_\odot \cos \lambda)\ d\tau \\
&= \frac{1}{\pi} \sum_{k=1}^{n} q_k\ [\sin \lambda_\odot \sin \lambda\ (\tau_k - \tau_{k-1}) \\
&\qquad - \cos \lambda_\odot \cos \lambda\ (\sin \tau_k - \sin \tau_{k-1})]\ d\tau. \quad (3.36)
\end{aligned}$$

Note that $\tau_n = \pi$ and $\tau_0 = \tau_u$. The factors from equation 3.36 are then used in equations 3.17 and 3.19 (where q = h and q = f, respectively) for the additive and multiplicative diurnal correction techniques.

(e.) The weighting factors, x_j and y_k, used in determining the f and h factors of the diurnal correction models

In order to obtain useful diurnal correction models (both additive and multiplicative) it is necessary to use most, or all, of the Stowe-Taylor ADMs available for a given angular bin. However, it is not necessary to overemphasize data that are irrelevant for a given use. For example, although we want to use a lot of ADMs in order to get a useful model for tropical regions, it is not necessary to weight the effect on the model of ice surfaces covered by clear skies too much, since such a scene is rarely, if ever, encountered in the tropics. In much the same vein, we don't want to weight overly much the ADMs for low solar zenith angles (large cosine of the s.z.a., or large sun elevations) for high latitude regions, where the sun never gets very high.

I determined what fraction of the target areas and days in the data I dealt with (6 days in June 1979) in each latitude band could be classified in each scene type. I then used a weighted mean of the constant weight (for each of the 12 scene types) weighting factors and the observation frequency weighting factors to get my scene type weighting factors. If f is the fraction by which I weighted the constant weighting factor in the calculation of my actual weighting factor, and t_k is the fraction of the time that the k^{th} scene type occurs in the latitude band being investigated, then

$$y_k = \frac{1}{12} f + t_k (1 - f). \qquad (3.37)$$

In my calculations, I used $f = 0.025$.

I also determined what fraction of the sunlit portion of the day fell in each of the 10 solar zenith angle bins, for each latitude band. If f fulfills a similar role here as in the determination of the y_k, and the τ_j is defined as in the last section, then

$$x_j = \frac{1}{10} f + \frac{\tau_j - \tau_{j-1}}{\tau_n - \tau_0} (1 - f). \qquad (3.38)$$

Note that for j > n, only the first part of equation 3.38 applies. In my calculations, I used $f = 0.33$.

Chapter 4

EXPLANATION OF THE PARAMETERS INVESTIGATED AND THE TECHNIQUES USED IN THE CALCULATIONS

In most of this chapter I explain which cloudiness and meteorological variables I analyzed and how I derived them from the data sets described in Chapter 2. In Table 4.1, I have listed all of the parameters I used in my analysis. The first column of this table lists the number for each parameter. In the next column, I list the mathematical symbol used to describe each parameter. In the third column, I give the shortened name which I use for each parameter in the tables in the appendices and the next chapter. In the last column I give a verbal explanation of each parameter. At the end of this chapter I describe how I took these parameters and performed the calculations described in chapter 3 on them.

IV.A) Reasons for choosing the variables listed in Table 4.1 for this investigation

My reasons for choosing the variables I did are intimately tied to the three goals I pursued in the course of this research (as explained in Chapter 1). The first purpose was to determine the effect of clouds (as they occur presently in the Earth's atmosphere) on the outgoing radiation from the Earth. This was the main reason for including the simple cloud cover fractions from THIR

TABLE 4.1

THE VARIABLES INVESTIGATED IN THIS THESIS AND THE SYMBOLS USED FOR THEM

1	$\overline{\mu_\odot}$	AVG MUSUN	diurnal average of the cosine of the solar zenith angle
2	F_{vis}	FLUX UP V	upwelling visible flux (irradiance) at the top of the atmosphere
3	F_{inf}	FLUX UP I	upwelling infrared flux (irradiance) at the top of the atmosphere
4	f_{tot}	F CL TOTL	areal fraction covered by clouds of all types
5	f_{low}	F CL LOW	areal fraction covered by low-altitude clouds
6	f_{mid}	F CL MID	areal fraction covered by medium-altitude clouds
7	f_{hi}	F CL HIGH	areal fraction covered by all high-altitude clouds
8	f_{hii}	F CL HI I	areal fraction covered by high-altitude ice clouds
9	f_{hiw}	F CL HI W	areal fraction covered by high-altitude liquid clouds
10	f_{tot}^2	FCL**2	square of total cloud fraction
11	$f_{tot} \cdot \alpha_s$	FCL*ASURF	total cloud fraction times surface albedo
12	$f_{tot} \cdot T_s$	FCL*TSURF	total cloud fraction times surface air temperature
13	$f_{tot} \cdot T_s^4$	FCL*TS**4	total cloud fraction times surface air temperature to the 4th power
14	$f_{tot} \cdot T_{1000}$	FCL*T1000	total cloud fraction times 1000 mbar temperature

15	$f_{tot} \cdot T_{cld}$	FCL*TCTOP	total cloud fraction times temperature of highest saturated layer
16	$f_{tot} \cdot \overline{\mu_\odot}$	FCL*MUSUN	total cloud fraction times diurnal average of cosine of the s.z.a.
17	$f_{tot} \cdot \alpha_s \cdot \overline{\mu_\odot}$	FCL*AS*MU	total cloud fraction times surface albedo times diurnal average of cos(s.z.a.)
18	T_s	T SURFACE	surface air temperature
19	T_s^2	TSURF**2	surface air temperature squared
20	T_s^3	TSURF**3	surface air temperature cubed
21	T_s^4	TSURF**4	surface air temperature to the 4th power
22	z_{500}	Z500	geopotential height of the 500 mbar level
23	T_{500}	T500	temperature of the 500 mbar level
24	T_{1000}	T1000	temperature of the 1000 mbar level
25	p_s	P SURFACE	pressure at mean sea level
26	σ_{H2O}	SIGMA W V	column water vapor density
27	n_{cld}	N CLD LYR	number of saturated layers in the FGGE analysis
28	z_{cld}	Z CLD TOP	geopotential height of the highest saturated FGGE level
29	T_{cld}	T CLD TOP	temperature of the highest saturated FGGE level
30	dS/dz	DS/DZ	vertical dry static energy gradient in the lower atmosphere
31	dH^*/dz	DH*/DZ	vertical saturated moist static energy gradient in the lower atmosphere
32	$\delta_H = \frac{H_a^* - H_s}{z_a - z_s}$	DH-AV/DZ	moist static energy at the surface minus saturated moist static energy in the middle troposphere divided by the vertical separation

33	$f(\delta_H) \cdot g(\omega)$	FLAG ST W	a nonlinear flag to indicate a positive DH-AV/DZ times a nonlinear flag to indicate a negative lower troposphere pressure vertical velocity
34	r_s	R SURFACE	surface air relative humidity
35	u_{500}	U500	eastward zonal wind speed at 500 mbar
36	v_{500}	V500	northward meridional wind speed at 500 mbar
37	$P_1(\sin \lambda)$	P1 LATITU	sine of the latitude
38	$P_2(\sin \lambda)$	P2 LATITU	1/4 minus 3/4 times the cosine of twice the latitude
39	α_s	A SURFACE	diurnal average of surface albedo
40	α_s^2	ASURF**2	diurnal average of surface albedo squared
41	$\alpha_s \cdot \overline{u_\odot}$	AS*MUSUN	diurnal average of surface albedo times diurnal average of cos(s.z.a.)
42	z_s	Z SURFACE	altitude of the surface

(variables 4 - 10). To obtain a better understanding of the real effect of clouds on the radiation budget, I also included variables involving surface albedo, surface temperature, cloud top temperature, and diurnally averaged incident flux (actually diurnally averaged cosine of the solar zenith angle). These are variables number 1, 11 - 17, 18, 21, 24, 29, and 39 - 41. Multiparameter regressions of all these variables give a fairly good idea of the effect clouds have on the Earth's radiation budget.

The second goal of this research was to elucidate simple predictive equations for the outgoing irradiance (both visible and infrared) from simple meteorological variables of the sort predicted by simple climate models. In order to get these equations I did multiparameter regressions on such variables. These variables include surface temperature, temperature in the middle-to-upper troposphere, surface albedo, incident solar flux, latitude, and sometimes fractional cloud cover (at all altitudes). This helps explain my inclusion of variables number 1, 4, 10 - 21, 23, 24, and 37 - 42.

My third goal in this thesis was to determine empirical relations (i.e., covariances) between meteorological variables of possible importance to radiation prediction (especially those variables associated with cloudiness) and top-of-the-atmosphere outgoing solar (reflected) and terrestrial (emitted) flux, so that these relations could later be compared with relations derived from the internal

statistics of general circulation models. For this goal I chose variables that I felt might make good cloudiness predictors, and those that should be associated with albedo or emission temperature. I also included some standard variables predicted by most GCMs. This goal justifies my inclusion of those variables listed in Table 4.1 not already justified by the previous two goals. I included 4 parameters (26 - 29) that I felt should be associated with large scale cloudiness (like that associated with mid-latitude baroclinic weather systems). Moreover, variables 30 - 33 were those I felt might be associated with convective scale cloud systems (for example, mid-latitude mesoscale convective complexes, trade wind cumulus, and clouds in the ITCZ). I might have wanted to include parameters involving differences of various variables between grid points, especially for convective cloudiness predictors. However, this is a first attempt at this sort of thing, the calculations were involved enough, and I am only developing empirical relationships to be compared with their theoretical counterparts (not developing definitive cloudiness predictors for general circulation models). Thus all the FGGE variables I investigated were derived from FGGE data at single horizontal gridpoints.

IV.B) Conversion of FGGE Level IIIb data into the variables listed in Table 4.1

The data on the ECMWF FGGE Level 3-b tapes (from here on referred to as EFL3Ts) consisted of only the most basic of meteorological variables. Deriving some of the more physically relevant variables from these origins required a fair amount of processing. The variables numbered 18 through 36 are derived from the EFL3T data. After their calculation, these variables were stored on disk for every six hours in the (six days in mid-June 1979) study period, at every sub-target area on the Earth. Because the FGGE horizontal grid did not correspond exactly with the grid of ERB sub-target areas, I used data from the FGGE gridpoint closest to the center of each sub-target area. Some FGGE derived variables were used in combination with THIR cloudiness data in variables 12 through 15.

(a.) Simple variables at standard pressure levels

Certain of the weather variables were simply taken directly from the EFL3Ts as is. These are the values of simple parameters at specific tropospheric pressure levels, variables 22, 23, 24, 35, and 36. In combination with THIR data, this is the origin of variable number 14. These variables should be useful in comparisons with the results of GCMs and might perhaps be useful in radiation predictive equations in the more complicated of the "simple" climate models.

(b.) Variables computed at the surface

Many of the variables I used involved values of FGGE variables computed at the Earth's surface. The FGGE variables were interpolated and extrapolated onto standard pressure levels, from the sigma levels (including the surface) on which they were computed, by cubic splines in all three spatial dimensions. However, it was sufficient for this investigation (in terms of accuracy, etc.) to use linear interpolation (or extrapolation) in the vertical dimension in order to determine the values of FGGE variables at the surface (A. Hollingsworth, personal communication, 1984). Surface pressure was computed using linear interpolation of the logarithm of pressure in the vertical.

In order to do the linear interpolation, I used the geopotential heights (z) listed on the EFL3Ts for each FGGE level and the height of the surface listed in the RAND/SIO elevation data set. In the troposphere, the difference between geopotential and actual geometric height is less than 1% just about everywhere on the globe. I chose the two levels bracketing the surface or (for those regions in which the surface lay beneath the lowermost level-the 1000 mbar surface) the two levels just above the surface. I then used the values at these levels, the geopotential heights at these levels, and the surface elevation to do the linear interpolation (or extrapolation). The variables computed this way were 18 - 21, 25, and 34. Variables 19 - 21 were derived from variable 18. By combining this type of data

with THIR data I got variables 12 and 13. All of these data should be useful in comparisons with GCM results, but the primary purpose of variables 18 - 21 was to derive predictive equations for radiation in simple climate models.

(c.) Large scale cloudiness variables

The major purpose of these variables was to determine the amount of water vapor and amount of saturated atmosphere available for making clouds. In terms of the goals of this thesis, these variables were designed to be compared with the results of GCMs and perhaps to indicate the value of various parameters as diagnostic indicators of cloudiness. Variables 28 (z_{cld}) and 29 (T_{cld}) were determined by finding the highest level on the EFL3T for which relative humidity equalled or exceeded 93% at each sub-target area and then tabulating the temperature and geopotential height for that level. Variable 27 (n_{cld}) is the summation of nonlinear flags related to relative humidity for each FGGE level above the surface at each sub-target area. Each nonlinear flag, ς_i, was calculated as

$$\varsigma_i = (r_i/100)^{\xi}, \tag{4.1}$$

where i designates the vertical FGGE level number, r is relative humidity (in percent), and ξ is an exponent chosen so that $\varsigma = 0.5$ when $r = 93\%$. Thus, n_{cld} is determined by

$$n_{cld} = \sum_i \varsigma_i. \tag{4.2}$$

Although no clouds should be visible (in a perfect model) unless r = 100%, in a real model, we are dealing with

average values of parameters over large areas (defined by the size of the grid used in the model) and there are uncertainties in the model. Thus, I chose a lower threshold value for relative humidity for the production of clouds. The choice of 93% is somewhat arbitrary, however, in various existing GCMs, values less than 100% are chosen as threshold values for cloud production (see for example Hansen, et al., 1980). In later work I hope to investigate the effect of varying the value of this threshold on the efficacy of cloudiness (and radiation) prediction. In the meantime, however, n_{cld} should be useful both as a predictor of the existence of large scale clouds and as an indication of the thickness of these clouds.

The column water vapor density was determined by adding the water vapor abundances in each FGGE level above the surface. Thus,

$$\sigma_{H2O} = \sum_i (r_i/100)\ \rho^*(T_i)\ \Delta z_i, \qquad (4.3)$$

where the thickness of each layer, i, is given by

$$\Delta z_i = (z_{i+1} - z_{i-1})/2,$$

for layers above the surface, and

$$\Delta z_i = (z_{i+1} + z_i)/2 - z_s,$$

for the layer just above the surface. Note that the saturation water vapor density is given by

$$\rho^*(T_i) = u_{H2O}\ p^*(T_i)/R\ T_i,$$

where u_{H2O} is the molecular weight of water, $p^*(T_i)$ is the vapor pressure of water over the liquid surface at a temperature T_i (the saturation vapor pressure of water), R

is the universal gas constant, and T_i is the temperature in the i^{th} FGGE level.

(d.) Convective cloudiness variables

I chose four variables as possible predictors of convective cloudiness and included them in my analysis. All four of these involved vertical energy gradients. One would expect convection and production of clouds whenever the lower atmosphere is unstable, has sufficient moisture for cloud production, and temperature decreases with height. Rather than actual instability, it is sufficient to have a conditional instability in the lower atmosphere, as long as there is sufficient motive force to raise low altitude air to its level of instability. I follow now with a derivation of the four parameters and their importance for prediction of dry and moist convection. The discussion follows much of the thinking in Sarachik (1981) and Lindzen (1981) in that I deal with energy gradients rather than such more traditional (and, to me, less intuitive) variables as static stability.

To sustain vertical motion of an air parcel, we require that air parcel to have a density less than that of its surroundings,

$$\rho_{(i)} < \rho_i,$$

where the subscript i refers to the i^{th} level in the atmosphere, and when it is in parentheses refers to a parcel moved to the i^{th} level from below. Since both the air in the parcel and that in the environment are at the same

pressure and contain gasses with (very nearly) the same average molecular weight, the inequality in densities is equivalent to an inequality in temperatures,

$$T_{(i)} > T_i. \qquad (4.4)$$

If the parcel of air came up from below with any reasonable speed and a minimum of mixing with its environment on the way, its temperature should be governed by the relations associated with adiabatic expansion. Thus, during ascent (as we change pressure), we have,

$$p\, dV + c_v\, dT = 0, \qquad (4.5)$$

where p is pressure, V is specific volume, c_v is specific heat at constant volume, and T is temperature. Incorporating the ideal gas law, the hydrostatic approximation, and the relation between constant volume and constant pressure specific heats, into equation 4.5, we get

$$c_p\, dT + g\, dz = 0, \qquad (4.6)$$

for the relationship between between temperature and height in the rising parcel of air (where g is gravitational acceleration and z is height). Thus, if the original temperature of the parcel (at level j) was T_j, then (assuming that c_p remains relatively constant) inequality 4.4 gives us

$$T_j - g\,(z_i - z_j)/c_p > T_i,$$

or

$$c_p\, T_j + g\, z_j > c_p\, T_i + g\, z_i. \qquad (4.7)$$

Note that this is the minimum requirement for convection (in the absence of condensation) since we have not included the

effects of mixing of the air parcel with its environment during ascent. If we define the dry static energy, S, as

$$S = c_p T + g z, \tag{4.8}$$

then the requirement for dry convection is

$$\frac{\partial S}{\partial z} < 0. \tag{4.9}$$

For those used to static stability, we can show

$$\frac{\partial S}{\partial z} = c_p g \rho^2 T \sigma,$$

where σ is the static stability as defined in Holton (1972). Although inequality 4.9 holds (on the large scales we are dealing with) only in the rarest of circumstances, I felt that a measure of the dry static energy gradient in the lower troposphere was a useful measure of how close to instability the atmosphere was at any given sub-target area.

If the parcel is saturated with water vapor then the situation is different. Equation 4.5 must be modified to yield

$$p\, dV + c_v\, dT + L\, dq^* = 0, \tag{4.10}$$

where L is the heat of condensation of water and q is the mass mixing ratio of water vapor in the air parcel. Any variable followed with an asterisk superscript is the value of that variable at saturation. If we make the same assumptions as in the dry case (plus the assumption that L does not change strongly with temperature) and we neglect the minor effect of the varying average molecular weight of

the air in the parcel associated with the removal of a portion of the water vapor, then inequality 4.4 reduces to

$$c_p T_j + g z_j + L q_j^* > c_p T_i + g z_i + L q_i^*. \qquad (4.11)$$

Now we can define the moist static energy, H, as

$$H = c_p T + g z + L q. \qquad (4.12)$$

Thus moist convection results when

$$\frac{\partial H^*}{\partial z} < 0 \quad \text{and} \quad q = q^* \quad (\text{i.e., } r = 100\%). \qquad (4.13)$$

Again, these results can be slightly modified by the effect of entrainment of environmental air in a rising air parcel. However, the relationships in 4.13 certainly hold in actively forming cumulus clouds.

It is possible to initiate and sustain moist convection even if not all of the relationships in 4.13 hold. If there is a region of the atmosphere which is unstable with respect to moist convection but this region contains no saturated air, convection can be initiated if the underlying air is moist enough and this lower air can be raised to a high and cold enough level that it begins condensing. This situation is called a conditional instability. Then if

$$\left.\frac{\partial H^*}{\partial z}\right|_i < 0 \quad \text{and} \quad q_j > q_i^* \qquad (4.14)$$

we can initiate convection by raising air from level j up to level i. Because moist static energy is conserved in both dry and moist ascent, the inequalities in 4.14 reduce to

$$H_j > H_i^*. \qquad (4.15)$$

If inequality 4.15 holds and the vertical wind between levels i and j is positive (and therefore the vertical pressure velocity is negative), moist convection should take place and cumulus clouds should form.

Because most of the solar energy that is absorbed by the Earth is absorbed at the surface, steep vertical temperature gradients (and therefore any possibility of negative static energy gradients) occur mainly in the lower troposphere. Moreover, the sources of water (mainly the oceans) are at the surface. Therefore, the best place to look for regions which satisfy relations 4.9, 4.13, and 4.15 is near the surface. I calculated the values of S, H, and H^* at the surface and S and H^* at a level in the middle troposphere. I used the relations

$$q = r\, q^*$$

and

$$q^* = \mu_{H2O}\, p^*(T)/\mu_{air}\, p, \qquad (4.16)$$

where r, T, and p are the ambient relative humidity, temperature, and pressure, respectively, and μ_{air} is the average molecular weight of dry air. Thus, I could calculate the static energies of interest from the data on the EFL3Ts and the surface variables which I had calculated (as described in subsection IV.B.c).

I used the energies at the 500 mbar level for middle atmosphere values everywhere except where the surface of the Earth lay above the 700 mbar surface. For these unusually high elevation (or low pressure) regions I used the 400 mbar

level for middle atmosphere variables. Since the differences in height between the middle troposphere level and the surface varies significantly for different sub-target areas and different times, rather than simply looking at the differences in energies between the two altitudes, I divided these energy differences by the difference in altitudes between the mid-troposphere level and the surface. If we define x_s as the value of x at the surface and x_a as the value of x in the middle troposphere, then the variables 30 - 32 were calculated as

$$\frac{\partial S}{\partial z} = \frac{S_a - S_s}{z_a - z_s}, \tag{4.17}$$

$$\frac{\partial H^*}{\partial z} = \frac{H_a^* - H_s^*}{z_a - z_s}, \tag{4.18}$$

and

$$\delta_H = \frac{H_a^* - H_s}{z_a - z_s}. \tag{4.19}$$

I refer to δ_H as the available moist static energy gradient since it gives the amount of energy actually necessary (the negative of that available for release) to raise an air parcel per unit height raised. A lower value of the dry static energy indicates a higher probability of convection, with the possibility of cloud production if there is enough moisture. A lower value of the saturated moist energy gradient indicates a higher probability of moist convection and cloud production. A low (i.e., negative) value of the available moist static energy gradient indicates the

probability of moist convection and cloud production provided there exists a motive force for lifting the low altitude air to its level of condensation (either large scale convergence at low altitudes and its attendant vertical winds or dry convection at low altitudes).

As a way of pulling together the importance of the available moist static energy gradient (AMSEG) and the vertical wind in a single variable, I invented variable 33 (see Table 4.1). I used the vertical pressure velocity (ω) at the 850 mbar level everywhere except in those sub-target areas in which the surface lay above this level. For these higher elevation areas, I used the vertical pressure velocity at the FGGE level which lay above but closest to the surface. I wanted a variable that grows with increasing negative AMSEG and with increasing negative vertical pressure velocity. Therefore, I chose a function which approaches zero for increasing negative AMSEG or increasing positive ω and which approaches one for increasing positive AMSEG and increasing negative ω. The function I chose was the product of the two non-linear flag functions

$$f(\delta_H) = \frac{1}{2} + \frac{1}{\pi} \tan^{-1} (-2\ \delta_H/\sigma_\delta), \qquad (4.20)$$

and

$$g(\omega) = \frac{1}{2} + \frac{1}{\pi} \tan^{-1} (-2\ \omega/\sigma_\omega), \qquad (4.21)$$

where σ_δ ($1.49 \cdot 10^4$) is the standard deviation of δ_H for those areas of the Earth in which the AMSEG most often

favors cumulus convection (the equatorial areas from 18° S to 18° N) and σ_ω ($6.12 \cdot 10^{-4}$) is the standard deviation of ω for all areas of the Earth. I chose these particular flag functions because they satisfied my requirements as stated above, they are easy to calculate, and (although they go from zero to one relatively rapidly for values of δ_H or ω near zero) they are not step functions and so do not overemphasize the significance of near zero values of δ_H or ω.

IV.C) The development of an albedo table from the published literature

Using published data, I determined the diurnal average albedoes for the three non-land surface classifications in the STRT "geography" files and for the nine vegetation classifications in the STRT "topography" files. The data sets I used included angularly resolved and angularly integrated radiometric data taken from airplanes, towers, and small platforms. Because I wanted to pull out the effect of surface albedo separate from the various effects of the atmosphere and clouds above the surface, I utilized data sets taken from inside the atmosphere (rather than from space) whenever possible.

Davis and Cox (1981) measured solar radiation reflected from a variety of surfaces with two different instruments mounted on a high flying airplane. The two instruments were a "bugeye" instrument which measured angularly resolved

radiances simultaneously from a variety of angles and a flat plate Eppley pyranometer which measured an angularly integrated flux. It is noteworthy that the pyranometer has a response that is dependant on the angle from its normal. Since I was dealing with an angularly resolved data set (the ERB scanner data), and I trust data in which the angular dependence of reflected radiation is explicitly specified, I used data from instruments like the Davis and Cox "bugeye" whenever such data was available. Davis and Cox (1981) published a regression equation for relating instantaneous albedoes (directional reflectances) measured by their Eppley pyranometer to those measured by their bugeye. Most of the data sets that I utilized that were not angularly resolved utilized measurements made by Eppley pyranometers or similar instruments. Therefore, I used the Davis and Cox regression equation to convert the directional reflectances in these data sets to what might have been measured by an angularly resolved radiance measuring device like the bugeye.

Most of the data sets I used had directional reflectances for several solar zenith angles. However, it was unusual to find one that covered the full range of solar zenith angles (from 0° to 90°) and the different data sets used different values of solar zenith angles in those ranges in which they overlapped. Thus I had three steps to develop a standard set of albedoes (directional reflectances) as a function of solar zenith angle for each of the twelve surface categories. First, I converted albedoes derived

from flat plate radiometers using the Davis and Cox regression. Then, I interpolated each data set onto a standard set of solar zenith angles (10 of them, corresponding to steps of 0.1 in the cosine of the solar zenith angle, $\mu_\odot$, from 0.05 to 0.95). Lastly, I averaged the various data sets for each surface type together.

When I had a set of directional reflectances for the ten standard solar zenith angles for all twelve surfaces, I made diurnal average albedoes for the twelve surfaces for all forty latitude bands. The diurnal average albedoes were weighted by the cosine of the solar zenith angle, in order to emphasize those times of day in which the most solar flux was incident on the Earth. The equation for conversion into diurnally averaged albedo is similar to equation 3.36. Thus the diurnally averaged albedo of a surface type is given by

$$\overline{\alpha} = \frac{1}{\overline{\mu_\odot}} \sum_{k=1}^{n} \alpha_k \, [\sin \lambda_\odot \sin \lambda \, (\tau_k - \tau_{k-1}) - \cos \lambda_\odot \cos \lambda \, (\sin \tau_k - \sin \tau_{k-1})], \quad (4.22)$$

where most of the variables are defined as they are in equation 3.36, the diurnal average of $\mu_\odot$ is given in equation 3.23, and α_k is the albedo of the surface being investigated in the k^{th} solar zenith angle bin. I put the diurnally averaged surface albedoes for the twelve different surface types for all 40 latitude bands down on disk, where I could use them when running the programs that analyzed the ERB scanner data.

In Appendix A, I give a thumbnail sketch description of each data set (in terms of the instruments and platforms used), a reference to the publication in which I found the data, and a brief summary of the data. For a more complete explanation of the data, the reader should refer to the original publications.

IV.D) The determination of average values for all the visible and infrared radiances and other variables for each target area for each day

The STR tapes were organized as follows. Data were presented in separate records binned by sub-target area (STA) and by the orbital pass on which they were obtained. The records were written on the tape in order of ascending target area (TA) number, within each TA by ascending STA number, and within each STA by ascending time of day of the orbital pass. TA numbers increase going south to north, and within each latitude band going east to west. The same is true of the order of STA numbers within each TA. For any TA, for which there was any ERB scanner data on a given day, the first record written on the STRT was the "Topography" record. This record gave the fraction of the surface of the TA coming up which was covered with the various vegetation categories (along with other surface cover data of little use to my investigations). I used this data (along with the surface albedo table on disk) to determine the average surface albedo for the land regions in the TA. The

"Topography" record was followed with the records for the STAs falling in the target area. The first record for each STA was the "Geography" record. This record gave the fraction of the surface of the STA which was covered by land, water, snow, and ice. From this information (along with the surface albedo table on disk and the information from the "Topography" record for the TA) I determined the average surface albedo for the sub-target area under investigation. Following each "Geography" record were the "Radiance" records for the STA. Each "Radiance" record contained the ERB scanner radiance data for an orbital pass of the STA along with the THIR parameters determined by Stowe's group at NOAA/NESDIS (if there were THIR data available for the STA during that flyover by Nimbus 7).

I collected the appropriate data and averaged them for each target area for each day (24 hours). The data were averaged in a vector of length equal to the number of visible angular bins I was using plus 54 (40 for the non ERB radiance data and 14 for the infrared angular bins). In each radiance record, there was written the number of angular bins (out of the 419 bins in the upward hemisphere) for which data was available, and for each angular bin there was a separate listing of each of the measurements of visible radiance and infrared radiance measured from the STA during that orbital pass, along with the fraction (in 9^{th}s) of the IFOV of the ERB scanner which fell in the STA for that measurement. I determined into which of my angular

bin any given ERB data fell and added that data to the vector of averages, weighted by the number of 9^{th}s of the scanner IFOV corresponding to each measurement. I utilized all infrared radiances, but I used only those visible radiances taken when the solar zenith angle over the STA was less than or equal to 87° (to avoid using pointless noisy nightime data). Each visible radiance I used was corrected with the appropriate diurnal correction (as discussed in Chapter 3, section C) before being added to the average vector.

For every radiance record, I looked up the value of all the FGGE derived parameters for the appropriate STA and time of day (to the nearest 6 hours) from tables on disk and looked up the diurnal average of the cosine of the solar zenith angle and the surface elevation from their tables on disk. Furthermore, I calculated the latitude of the STA (and therefore variables 37 and 38) and I already had the diurnal average surface albedo. All these parameters were added to the average vector, weighted by the number of (the original 419) ERB angular bins that were represented in the record.

If any THIR data were available, I added the cloudiness fractions to the vector of averages, weighted the same way that the FGGE and other (always available) data were weighted. If the THIR flag was on indicating that the high clouds were ice, I let the fraction of high ice clouds be equal to the fraction of high clouds listed in the record

and I let the fraction of high liquid water clouds be zero. The opposite held true in cases where this flag was off. These fractional cloudinesses were also added to the vector of averages weighted the same as the other THIR data. Some of the THIR data was multiplied by some FGGE (or other non-radiance data) to get the mixed variables (like variables 11 - 17 in table 4.1). These mixed data were treated the same as the other THIR data.

After having read all the records for a target area on the STRT, the vector containing the averages of all the data for that TA was stored, along with the weighting for each of the variables for that TA. The only data not stored was radiance data for which the weighting was less than or equal to 3. This kept the average radiances from being dominated by data coming from other target areas (since a weighting less than 3 indicated the only data for that angular bin had less than 3/9 of an ERB scanner IFOV lying in the TA under investigation). Such data were zeroed out in the average vector, as were the corresponding weights in the weighting vector. The resulting average vectors (which I will refer to as the target area or TA vectors) for each target area during each 24 hour period became my basic data set.

IV.E) The determination of the summation matrices

I used the basic TA vectors for statistical analyses of various subsets of the complete data set (2070 target areas over the six days in June 1979 and the one day in November

1978). Since the primary purpose of this thesis was to do linear regressions of visible flux and infrared flux against each other and against all of the other previously mentioned variables, I needed the averages and variances of the fluxes and the other variables and the covariances of all of the variables (including fluxes) with each other, for each subset of the total that I investigated. As explained in chapter 3 section A, to determine the averages of the outgoing fluxes, we need to know the averages of all of their constituent radiances. To determine the variances of these fluxes (and the covariance of visible and infrared fluxes), we need to know the covariances of all their constituent radiances with each other (including themselves). To determine the covariances of the fluxes with the various other variables, we need to know the covariances of their constituent radiances with each of the other variables. Thus, for each subset of the data, I determined the vector of averages for all $40 + 14 + N_{vis}$ variables, and I determined the matrix of covariances for all these variables with each other (including themselves - i.e., their variances).

For each variable in the average vector, we need the sum of all the measurements contained in the TA vectors and the number of measurements contained in those TA vectors. For the covariance of two variables, we need the sum of each, the population of each, and the sum of their products. This is to say,

$$\langle x_i \rangle = \frac{\sum x_i}{n_i}, \tag{4.23}$$

and

$$\sigma_{ij} = \frac{\sum x_i x_j}{n_{ij}} - \langle x_i \rangle \langle x_j \rangle$$

$$= \frac{\sum x_i x_j}{n_{ij}} - \frac{\sum x_i}{n_i} \frac{\sum x_j}{n_j}. \tag{4.24}$$

Since I was dealing with data sets of less than infinite size, any estimate of the average of a variable I made contained some error. Therefore, if I used the estimates of averages from equation 4.23 in order to determine the covariance as shown in equation 4.24, I included an unnecessary element of error in my analysis. It is even possible to show that if one determines covariances this way, it is possible to calculate (erroneously, of course) correlation coefficients greater than one or less than negative one. Thus, to determine the covariance, σ_{ij}, I calculated

$$\sigma_{ij} = \frac{P_{ij}}{n_{ij}} - \frac{S_{ij}}{n_{ij}} \frac{S_{ij}}{n_{ij}}, \tag{4.25}$$

where S_{ij} is the sum of all measurements of variable i when variable j was also measured (in the same TA vector), S_{ij} is the sum of all measurements of variable j when variable i was also measured, P_{ij} is the sum of all the products of variables i and j when both were measured, and n_{ij} is the number of times (i.e., the number of TA vectors) in which both variables i and j were measured. Thus, it was

necessary in the analyses of any subset of the data to collect summation matrices of three types: the population matrix n_{ij}, the sum matrix S_{ij}, and the product matrix P_{ij}.

The sun azimuth relative to the Nimbus 7 spacecraft as seen from the ground was dependant upon the latitude of the ground target (due to Nimbus 7 being in a sun synchronous orbit). Because of this and because of the fixed (and somewhat inflexible) nature of the ERB scan patterns, the ability of Nimbus 7 to measure the radiance from a target area for a given angular bin during the same day as it measured the radiance (from the same target) in a given other bin was dependent on the latitude of the target under consideration. Thus the population of any element of the summation matrices that involved radiance (especially visible radiance) measurements was heavily influenced by the latitudes measured in the subset of the data that the summation matrices covered. Some of the subsets I investigated involved data from many different latitudes (sometimes the entire earth) being combined, but I didn't want to give undue weight to those regions of the earth that were much better sampled than the others. Therefore, I used weighting factors in summing the elements of the summation matrices that depended on the latitude of the measurement being summed. Thus,

$$S_{ij} = \sum_{k(i,j)} W_{ij}(\lambda^{(k)})\, x_i^{(k)}, \qquad (4.26)$$

$$P_{ij} = \sum_{k(i,j)} W_{ij}(\lambda^{(k)})\, x_i^{(k)}\, x_j^{(k)}, \qquad (4.27)$$

and

$$n_{ij} = \sum_{k(i,j)} W_{ij}(\lambda^{(k)}), \qquad (4.28)$$

where $W_{ij}(\lambda)$ is the latitude dependent weighting factor for the i,j element of the summation matrices, $y^{(k)}$ is the k^{th} measurement of y, and the summations occur over k(i,j) meaning that one sums only those measurements where both i and j were measured. These (equations 4.26 - 4.28) then were the relations used to determine the necessary data to calculate the elements of the covariance matrix (as shown in equation 4.25) and of the average vector, for each subset that I investigated.

IV.F) Filling in blanks in the summation matrices

As I explained at the end of section A of chapter 3, it is necessary to work with a data set including at least a few measurements of radiance for each angular bin taken at the same time as measurements from any given other angular bin (for each angular bin) in order to determine the statistics of the flux being investigated. For some regions of the Earth, not all combinations of angular bins were sampled (i.e., there were zero elements in the population summation matrix for such a region). When such a situation arose, I dealt with it by making a slight change in the angular bin pattern I used. Any bin which had a lot of empty elements in the population matrix, I combined with an adjoining angular bin (preferably not combining bins from an azimuth of 180°, and not combining bins from different

zenith angles). I added the elements in the row and column of the combined bins together. The sums were placed in the elements of the matrices corresponding to one of the small bins being combined. The elements of the summation matrices corresponding to the other small bins being combined were then ignored for the rest of the analysis (and in fact zeroed out for safety). The result is similar to having used the new angular bin pattern to begin with, with the new matrices corresponding to the summation matrices that would have been calculated with that bin pattern (with the addition of a few null rows and columns). Then in order to convert the statistics of the radiances into flux statistics (as described in section A of chapter 3), I used bin characteristics (solid angular size and cosine of the zenith angle) of the larger combined bins rather than the original small bins. In some instances (especially where the geographical subsets were quite small) it was necessary to combine so many bins that it was worthwhile to convert the summation matrices for the 49 visible angular bins into the corresponding matrices for the 19 visible angular bin pattern. This was done in the same way as the less drastic conversions discussed above. The covariance matrix and average vector were then calculated using the characteristics of the 19 angular bin pattern.

IV.G) Which summation matrices were calculated

In addition to the aforementioned three goals of this thesis, a major thrust of my research was to determine if the techniques I outlined in Chapter 3 (for the analysis of top-of-the-atmosphere radiative flux and its variance using the statistics of top-of-the-atmosphere radiances and for the corrections for diurnal coverage) were sensitive to the various specifics of my analysis (i.e., I investigated the systematic errors of this research). Therefore, summation matrices were calculated using different angular bin patterns for the visible radiances, different diurnal corrections for the visible radiances, and using other different specifics of the calculation. The different techniques used in my calculations are enumerated and described in Table 4.2.

For most of my calculations, I determined the three summation matrices for 80 different regions on earth. These regions consisted of the land areas and the ocean areas in each of 40 latitude bands 4.5° wide. To investigate the characteristics of any larger region, the summation matrices of the land or ocean areas or both from the appropriate latitudes were added and the resulting summation matrices were used to determine the covariances and averages appropriate to the region in question. In order to compare the results from different sorts of calculations, covariance matrices and average vectors were determined for various standard regions of the earth. These regions are easily

TABLE 4.2

ANALYSIS TECHNIQUES, GEOGRAPHIC GROUPINGS, AND WAVELENGTH CATEGORIES USED IN THIS THESIS AND THE HEADINGS FOR THEM AS USED IN TABLES

The analysis techniques

32BIN NOV	data from 28 November 1978 were analyzed using the angular bin pattern in Figure 3.3b for the visible radiances, diurnal correction factors from the constant model were used; no FGGE data was analyzed along with the ERB data here
32BIN JUN	data from 12 June 1979 were analyzed using the angular bin pattern in Figure 3.3b for the visible radiances, diurnal correction factors from the constant model were used
49BIN CON	data from 12 June 1979 were analyzed using the angular bin pattern in Figure 3.3c for the visible radiances, diurnal correction factors from the constant model were used
49BIN MUL	data from 12 June 1979 were analyzed using the angular bin pattern in Figure 3.3c for the visible radiances, diurnal correction factors from the multiplicative model were used
49BIN ADD	data from 12 June 1979 were analyzed using the angular bin pattern in Figure 3.3c for the visible radiances, diurnal correction factors from the additive model were used
19BIN ADD	data from 12 June 1979 were analyzed using the angular bin pattern in Figure 3.3d (see the text for caveats) for the visible radiances, diurnal correction factors from the additive model were used
6DAY 49BA	data from 12 - 18 June 1979 were analyzed using the angular bin pattern in Figure 3.3c for the visible radiances, diurnal correction factors from the additive model were used; this is the data set from which I derived most of my conclusions

6DAY 19BA — data from 12 - 18 June 1979 were analyzed using the angular bin pattern in Figure 3.3d (see the text for caveats) for the visible radiances, diurnal correction factors from the additive model were used

LAT 49BA — data from 12 - 18 June 1979 were analyzed using the angular bin pattern in Figure 3.3c for the visible radiances, diurnal correction factors from the additive model were used; rather than averaging data for 500 km squares over 24 periods as the basic data, I used data averaged over entire 4.5° latitude bands for 3 day periods

The geographic groupings

20 LATITUDE — the earth was divided by latitude into 20 bands, each 9° wide, all data were used

8 LATITUDES — the earth was divided by latitude into 8 bands, each 22.5° wide, all data were used

CONTINENTAL — the earth was divided by latitude into 5 bands, of width 40.5°, 36°, 27°, 36°, and 40.5° (going from south to north), only data from target areas with surfaces covered mostly by land (or land ice) were used

10 CONTINEN — the earth was divided by latitude into 10 bands, each 18° wide, only data from target areas with surfaces covered mostly by land (or land ice) were used

OCEANIC — the same latitude bands as in the "CONTINENTAL" grouping were used, only data from target areas with surfaces covered mostly by water (or sea ice) were used

10 OCEANIC — the earth was divided by latitude into 10 bands, each 18° wide, only data from target areas with surfaces covered mostly by water (or sea ice) were used

HEMISPHERIC — the earth was divided into the northern and southern hemispheres, all data were used

WHOLE EARTH — the entire earth was used as a single grouping, all data were used

The wavelength categories

VISIBLE — statistical variables pertaining to outgoing visible flux

ALBEDO	statistical variables pertaining to visible albedo
INFRARED	statistical variables pertaining to outgoing infrared flux
NET GAIN	statistical variables pertaining to the net (top-of-the-atmosphere) incoming flux; this involves the negative sum of the results under the VISIBLE and INFRARED headings

grouped into sets based on the way they are distributed about the earth. These geographic groupings are listed and described in Table 4.2.

IV.H) How the covariance matrices and average vectors were used

The values for the covariances of visible flux and infrared flux each with all 42 variables are not particularly interesting, except for comparing with the internal statistics of powerful climate models such as GCMs. Their real utility lies in their use for determining correlation coefficients and linear regression coefficients (for both single and multiple parameter regressions). The correlation coefficients are useful for determining the power of various variables as diagnostics for the presence, amount, and type of cloudiness (or at least, those aspects of cloudiness that are important for changing amounts of infrared and visible radiation). The linear regressions are useful both for determining the net effect of clouds on the radiation balance of the Earth (under various conditions) and as diagnostic equations for radiative flux in simple climate models (especially energy balance climate models).

The correlation coefficient of two variables, x and y, is simply

$$r_{xy} = \frac{\sigma_{xy}}{\sigma_x \, \sigma_y}. \qquad (4.29)$$

For a linear regression of the form $y - \langle y \rangle = a\,(x - \langle x \rangle)$, the linear regression coefficient, a, is

$$a = r_{xy} \frac{\sigma_y}{\sigma_x} = \frac{\sigma_{xy}}{\sigma_x^2}. \qquad (4.30)$$

Discussions of linear regression of this sort can be found in Bevington (1969) and Lindgren, et al. (1978).

For multiple linear regression, we consider a linear function for y in terms of the variables, x_i,

$$y = a_0 + a_1 x_1 + a_2 x_2 + \ldots + a_n x_n. \qquad (4.31)$$

Then the first term, a_0, is given by

$$a_0 = \langle y \rangle - a_1 \langle x_1 \rangle - a_2 \langle x_2 \rangle - \ldots - a_n \langle x_n \rangle. \qquad (4.32)$$

A linear least squares analysis of equation 4.31 gives the regression coefficients, a_j, in terms of a matrix equation. We let

a_j = the j^{th} element of the vector $\underset{\sim}{A}$,

σ_{jk} = covariance of x_j and x_k
= the element in the j^{th} row and k^{th} column of the matrix $\underset{\approx}{\Sigma}$,

σ_{yk} = covariance of y and x_k
= the k^{th} element of the vector $\underset{\sim}{\Sigma}^y$,

where $j = 1,\ldots,n$ and $k = 1,\ldots,n$. Then the vector of regression coefficients for this multiparameter regression is given by

$$\underset{\sim}{A} = \underset{\approx}{\Sigma}^{-1}\, \underset{\sim}{\Sigma}^y. \qquad (4.33)$$

The variables, x_j, in these multiple regressions do not need to be simple. For example, a polynomial regression of y in terms of some variable z can be accomplished by simply

letting $x_j = z^j$ in the discussion above. This requires, of course, collecting statistics on all the powers of z in which one is interested. I have done this in this research for the surface temperature. Obviously, the statistical parameters referred to above, that I used in the various regressions I performed, were selected from the appropriate covariance matrices and average vectors that I had calculated.

How does one compare the results of different multiple regressions with each other and with single parameter regressions, in terms of goodness of fit? Analogous with the linear-correlation coefficient there is the multiple-correlation coefficient R. It is calculated as

$$R^2 = \sum_{j=1}^{n} aj \frac{\sigma_{yj}}{\sigma_y^2} \qquad (4.34)$$

By comparing R for different multiple regressions with each other and with the absolute value of r for single regressions, one can determine which regression fits the data better. The presentation I have made above for multiple linear regression is similar (but not identical) to that found in Bevington (1969).

Chapter 5

RESULTS

This chapter is the presentation of the results of my thesis. In the first part of the chapter, I describe how I calculated the best version of my results, explain why I analyzed the data the way I did to arrive at these results, and discuss the sources and magnitudes of error in my results. Explaining the reasons for analyzing the data the way I did consists of describing the effects of changing the number of angular bins for the analysis of the visible data, the effects of changing the diurnal variation model used to correct the visible data (to get diurnallly averaged visible radiances), and the differences in the results for different time and space scales of averaging. In the second part of this chapter (sections C and D), I discuss what my results imply for the effect of clouds on the Earth's radiation budget and what sort of simple predictive equations for top-of-the-atmosphere radiation can be derived from my results. This chapter's third part (section E) is a presentation of some results of my single and multiple parameter regressions of flux and the use of these regressions for comparison with the results of general circulation models of the Earth's atmosphere, the results of simple climate models, and earlier analyses of top-of-the-atmosphere radiation.

V.A) What sort of results were best and why

I analyzed ERB scanner data from 7 days - 12, 13, 14, 16, 17, and 18 June 1979 and 28 November 1978. The November results are not emphasized in this chapter because I did not have correlative FGGE data for that time period, and because the radiative data that I used were of slightly lower quality than the data from June. Most of my results are the results of analysis of the June data for one set of analysis techniques. I used three different patterns of angular bins for the visible radiances, three different schemes for converting instantaneous visible data into diurnal averages, two different spatial and time scales for averaging data to get my statistics, and I combined data in different groupings of latitudes and longitudes for analysis. Of those techniques I used, the best way in which to analyze the data was to use the angular bin pattern containing 49 bins for the visible radiances, the additive diurnal variation model to derive the diurnal correction factors for the visible data, and to use all 6 days worth of data (from June 1979) to get good statistics. The two different spatial and time scales for averaging data to get my statistics were both valid and the results of both are presented here, for the various groupings of latitude and longitude that I found useful.

(a.) How changes in the pattern of angular bins for the visible radiances affected the analysis of variance

I used three different patterns of angular bins for the visible radiances. Rather than print out all the covariances and correlation coefficients I derived with the various (and mostly inferior) analysis techniques, I have determined the statistical relationships between the averages, covariances, and correlation coefficients for the good technique (that described above) and the other techniques. The relationships are tabulated in Appendices B and C. The exact form of the statistical relationships investigated in these appendices are explained in the appendices themselves.

Appendix B presents the results of changing the number and pattern of angular bins for the visible radiances on the results of my analysis. The first two tables in Appendix B present a comparison of the 49BIN CON and 32BIN JUN data sets. The only difference between these data sets is the angular bin pattern used for analysis of visible radiances. The same sort of diurnal corrections were used (those based on the constant diurnal model) and the exact same ERB, FGGE, and THIR data were analyzed. Two major results are apparent from a quick appraisal of these two tables. The first is that the effect of changing the pattern of angular bins (used in the analysis of visible radiance) on the averages of the visible flux and the covariances and correlation coefficients of the visible flux with the 42 variables is

quite small. For nearly all the variables and geographic regions, the effect is less than 10%, and for the majority the effect is less than 5%. The second result shows that using the 49 bin angular pattern is better than using the 32 bin angular pattern. The reason for saying this is that the correlation coefficients (of the visible flux with the other variables) for the 49 bin analysis are usually higher than those for the 32 bin analysis. I can think of two possible reasons for this. In general, using more bins samples the radiation field better. Secondly, as a quick perusal of figure 3.3 shows, the 32 bin pattern I employed combined radiances from too broad a range of zenith angles in most areas and from too broad a range of azimuths in sensitive regions (specifically, near the region of specular reflection) to be completely safe.

The last two tables in Appendix B present a comparison of the 6DAY 49BA and 6DAY 19BA data sets. The same ERB, FGGE, and THIR data were analyzed for both analyses. The only difference is that after calculating the summation matrices for the 6DAY 49BA data set, various elements of the matrices were added together to yield the summation matrices that would be expected for the 19 visible angular bin pattern shown in figure 3.3b. The point of this comparison is to test how much combining bins in this way impacts the results. It was often necessary to combine a few bins in order to eliminate zero population matrix elements. The results are similar to the comparison in the first half of

the appendix. There are very few cases in which the effect is greater than 10% and for the majority of variables and geographic groupings the effect on the averages, covariances, and correlation coefficients is less than 5%. Moreover, the correlation coefficients for the 49 bin analysis are generally higher than for the 19 bin analysis, although not by much. Presumably, this is simply due to not mixing too large a range of azimuths in the bins of the 49 bin analysis.

(b.) How changes in the diurnal correction techniques affected the analysis of variance

Appendix C presents the results of changing the sort of diurnal corrections used on the visible radiances on the results of my analysis. Three data sets are compared: 49BIN CON, 49BIN ADD, and 49BIN MUL. Again, the exact same basic data were analyzed in all three cases. Only the diurnal correction factors (as discussed in Chapter 3, Section C) were changed. The effect of changing from the constant diurnal model to either the additive or the multiplicative models is both noticeable and somewhat variable. However, certain things are clear. First, using either non-constant model causes increases in the calculated average visible fluxes and covariances of the visible fluxes with other variables. The reason for this, I believe, is that at high solar zenith angles, for most sorts of surface-atmosphere ensembles, the albedo is higher than at low solar zenith

angles. For example, in regions of a dark surface overlain by patchy clouds of finite thickness, at high zenith angles the sun is illuminating more high albedo clouds and less of the dark underlying surface (due to shadowing between the clouds) than at low zenith angles.

A comparison of the correlation coefficients indicates that effect of the different diurnal corrections exceeds 25% for only a very small portion of the different variables and geographic regions and for the most part the effect is less than 15%. Apparently, the choice of diurnal correction factors is important but not overwhelming. Interestingly, the correlation coefficients of the additive data set are slightly higher than for the constant or multiplicative data sets. Perhaps this is due to the better fit to the change in albedo with solar zenith angle provided by the additive model (as seen in Figure 3.5). Another interesting point is that the effect of using different diurnal correction techniques depends on the region of the globe and the variables being investigated.

V.B) Sources and magnitudes of error

There are three main sources of error to consider in this research. The first source consists of the systematic and random errors in the measurements used as the basic data set in this thesis. The probable sizes of these errors were discussed in chapter 2. These errors are generally smaller than the errors from the other two sources. The second type

of error is the systematic errors introduced by the techniques as discussed in the previous section. The third type of error is simply the random statistical error inherent in estimating such parameters as covariances, correlation coefficients, regression coefficients, etc. from a limited data set. It is this last source of error that, in the main, provides the main topic of this section.

(a.) An example of the effects of random statistical error

Before going into the math of estimating the uncertainty of my results due to statistical error, I will present an example of its effects. In appendix D, I present a statistical analysis (similar to those of appendices B and C) of the differences between the 6DAY 49BA and 49BIN ADD data sets. The only difference between these two data sets is that for the 49BIN ADD data set I analyzed only the data for 12 June 1979, whereas, for the 6DAY 49BA data set I analyzed all 6 days of data from June 1979 (including, of course, 12 June). The techniques used in the analyses (angular bin patterns, diurnal correction techniques, scale of time and space averaging, etc.) were all the same. Since there should be no particularly big difference between the large scale climate on 12 June and the other 5 days (through 18 June), any difference between the results should indicate the sort of errors (especially in the 49BIN ADD data set) associated with the comparatively poor sampling of the Earth available in only one day, and the comparatively poor

sampling (and availability for sampling) of the weather patterns responsible for the variation in the top-of-the-atmosphere radiative fluxes in that single day relative to a larger data base. Although problems involving the size of the data set analyzed are important for all variables, I examine here the effects on the statistical parameters for the visible flux, because I had the software already running and the visible flux (along with infrared flux) was the main topic of this research. It is noteworthy that although, on the average, the statistical results are the same for the two data sets, there are significant variations between them. A more careful analysis of the statistics (than that presented in Appendix D) shows that the most dramatic variations occur in those areas which were poorly sampled for visible radiances like southern high latitudes in the 8 LATITUDES geographic grouping or the 13.5° to 49.5° latitude band (which is primarily oceanic) in the CONTINENTAL geographic grouping.

(b.) Standard errors for means and regression coefficients and the statistical significance of correlation coefficients

For a data set with a normal distribution, the standard error for the mean is $s(\langle x \rangle) = \sigma_x / N^{1/2}$, where $\langle x \rangle$ is the estimated mean of x, σ_x is the measured standard deviation of x, and N is the number of observations of x used in the computations. One can also show that the standard error of a (where a is defined in equation 4.30) is

$$s(a) = \{[(\sigma_y/\sigma_x)^2 - a^2]/(N - 2)\}^{\frac{1}{2}}. \qquad (5.1)$$

The expression in equation 5.1 can be found (albeit in slightly different form) in both Bevington (1969) and Lindgren, et al. (1978). A more convenient way to express the uncertainty in the regression coefficient is in fractional form

$$s(a)/a = [(r^{-2} - 1)/(N - 2)]^{\frac{1}{2}}. \qquad (5.2)$$

The probability that the absolute value of a measurement of the correlation coefficient of two uncorrelated variables would exceed the absolute value of the correlation coefficient, r, that was measured for some data set of size N, is given by

$$P_c(r,N) = \frac{1}{\pi^{\frac{1}{2}}} \frac{\Gamma[(N - 1)/2]}{\Gamma[(N - 2)/2]} \int_{|r|}^{1} (1 - x^2)^{\frac{1}{2}(N - 4)}\, dx, \qquad (5.3)$$

where $\Gamma(\nu)$ is the gamma function evaluated at ν (see Bevington, 1969, p. 310). If a measured correlation coefficient has an absolute value exceeding P_c for the appropriate N, it is probable (at a level of $1-P_c$) that the variables being compared are not uncorrelated.

One major problem in utilizing the statistics discussed above is that I determined the covariances of the radiative fluxes with the various variables by using a linear combination of the covariances of the radiances. There is no specific number of observations, N, of the flux that can be easily used in determining the random errors and statistical significance of the results. One possibility is to use the number of observations of the radiances to

determine the random errors of the covariances of the radiances and then to use these errors to determine the random error of the flux covariance (and, therefore, regression coefficient, etc.) in question. If we have some variable x, which is a function of a series of other variables, u, v, ..., then the variance of x is given in terms of the variances and covariances of the independent variables, u, v, ..., as

$$\sigma_x^2 \approx \sigma_u^2(\frac{\partial x}{\partial u})^2 + \sigma_v^2(\frac{\partial x}{\partial v})^2 + 2\ \sigma_{uv}(\frac{\partial x}{\partial u})(\frac{\partial x}{\partial v}) + \ldots, \qquad (5.4)$$

(see Bevington, 1969, p. 59). Thus, it should be possible to determine the variance (and so the standard error) of the flux variances and covariances by simply replacing x with σ_{yF} and replacing the u, v, etc. with σ_{yRi} (for the various bins i) in equation 5.4. However, the variance of a covariance and the covariance of two covariances are pretty nebulous concepts (and perhaps demand too many assumptions about the nature of the parent population of the basic data). Thus I have used a much simpler (and more heuristic) technique. The outgoing flux is very highly correlated with the radiance from a given angular bin, for most angular bins. In a sense, then, every time I take a measurement of the radiance in some bin, I have taken a measurement of the flux. What I have done, then, is to estimate the number of flux measurements by determining the number of measurements of each radiance and multiplying it by the contribution of that radiance to the flux (i.e., $u_i\ \Delta\Omega_i$ for bin i), then

adding the results for all the angular bins to get an effective number of flux measurements. I can then use this number as the effective number of measurements for the flux in equations 5.1 - 5.3.

(c.) Displays of some of the basic data

In order to better visualize the relationships between radiative flux and the other variables, it would be nice to make scatter plots of flux (visible or infrared) vs. any other measured variable or plots of predicted flux (for some multi-variable regression) vs. measured flux. However, there are no measurements of top-of-the-atmosphere radiative flux (at least of the sort and scale dealt with here). To get around this lack, what I have done is to make estimates of the flux using measured radiances from angular bins whose radiances are very highly correlated with the total flux. Using the techniques outlined in Chapter 3, section A, I determined the covariances between infrared flux and all the constituent infrared radiances (equation 3.3, with x replaced by R_k for the k^{th} bin). I used these covariances along with the averages of the flux and the radiances to determine which angular bins had radiances which were most highly correlated with the infrared flux and then determined linear regressions for the infrared flux as a function of each of those infrared radiances which were highly correlated and which were measured often enough to be useful. The same thing was done with the visible flux and

visible radiances. Using the average radiances in the target area vectors, I estimated the infrared flux and visible flux leaving each target area, each day by taking an average of the estimate of each flux from the various highly correlated radiances that had been measured for that TA during that day. These are the "measured" fluxes plotted in the latter part of this chapter.

(d.) The true number of independant samples of radiative and meteorological data and the autocorrelation function

The number of data samples, N, used in the determination of statistics is useful in applications such as equations 5.1 - 5.3 if the samples of the data were actually independant of each other. In order to accurately measure the statistics of the atmosphere, we need a large number of samples describing the full range of variability inherent in that portion of the atmosphere being reviewed. To estimate how well the atmosphere has been sampled, we use some number, N, indicating the number of samples of the atmosphere that were far enough separated in time and space from all the other samples so that none of the samples was simply a near repeat of some previous measurement. The time scale over which my samples were taken was 24 hours, and the space scale was about 500 km (in both horizontal directions). As it turns out, the diurnal average radiative flux leaving some region 500 km on a side (and, presumably, the meteorological variables that determine the flux)

doesn't vary very much on a time scale of just one day or on a spatial scale of only 500 km. In order to determine the number of independent measurements which I had in my data set (rather than the number of partially overlapping measurements), it was necessary to determine the approximate time and space scales of variability of the atmospheric radiation.

My only reason for determining these natural scales of variability was to determine the number of measurements I had used in my analysis, so that I could assign values for the random errors and the statistical significance of my results. Therefore, I used a fairly easy technique. I calculated something similar to an autocorrelation function for the "measured" flux estimate (both visible and infrared; as discussed in the previous section) in both space (the East-West direction) and time. What I did was simply to determine the correlation coefficients between the flux measured at a point in space and time and that measured at the same place a while later, for various lag times. I then determined the correlation coefficients between the flux measured at a point in space and time and that measured simultaneously a distance away, for various displacements. I then used these correlation coefficients to determine at what lag time and what distance the correlation coefficients have decreased sufficiently to declare the measurements independent of each other.

To determine the timescale (or spatial scale in longitude) of variability, we need to look at the correlation coefficients for various lag times and spatial separations. We define f as,

$$f_i = \frac{x_i - \langle x \rangle}{\sigma_x} \quad \text{and} \quad f(t) = \frac{x(t) - \langle x \rangle}{\sigma_x}, \qquad (5.5)$$

where x is some arbitrary variable, and t is time or some other independent variable (such as distance in longitude). We can then define a variable S for any limited sample of N *independent* measurements,

$$S = \sum_{i=1}^{N} f_i .$$

After a near infinite number of measurements of S, it should be possible to define a variance for the quantity,

$$\sigma_S^2 = \langle S^2 \rangle - \langle S \rangle^2 = \langle S^2 \rangle = \langle \sum_{i=1}^{N} \sum_{j=1}^{N} f_i \, f_j \rangle$$

$$= \sum_{i=1}^{N} [\langle f_i^2 \rangle + \sum_{j \neq i} \langle f_i \, f_j \rangle]$$

$$= \sum_{i=1}^{N} \langle f_i^2 \rangle = \frac{N \, \sigma_x^2}{\sigma_x^2} = N. \qquad (5.6)$$

In general, however, we have a nearly continuous set of measurements that may or may not be truly independent of each other from some interval of time (or any independent variable, t) of length T. Therefore, rather than dealing with the sum, S, of the independent measurements, we deal with an integral, I, of effectively independent measurements,

$$I = \frac{1}{\Delta t} \int_0^T f(t)\, dt,$$

where Δt is the natural scale of variability of x (and therefore f). If the measurements we are making are to be of any use for statistics, then T (the size of each sampling interval) is much larger than Δt, the natural scale of variability. From a near infinite sample, we should be able to define the variance of I,

$$\sigma_I^2 = \langle I^2 \rangle = \frac{1}{(\Delta t)^2} \langle \int_{t=0}^{T} \int_{t'=0}^{T} \langle f(t)\, f(t') \rangle\, dt\, dt'$$

$$= \frac{1}{(\Delta t)^2} \langle \int_{t=0}^{T} \int_{t'=0}^{T} \frac{\sigma[x(t),\, x(t')]}{\sigma_x\ \ \sigma_x}\, dt\, dt'. \qquad (5.7)$$

The expression in the integral is simply a correlation coefficient. Since the correlation coefficient of a variable measured at any given time, t, and that variable at any other time, t', should depend only on the difference in these two times and not on their actual values, we can simply use the expression, r(t - t') for this expression. If we make the change of variables $\tau = t - t'$, then equation 5.7 becomes,

$$\sigma_I^2 = \frac{1}{(\Delta t)^2} \int_{t=0}^{T} [\int_{\tau=t-T}^{T} r(t - t')\, d\tau]\, dt. \qquad (5.8)$$

For the scale of variability, Δt, to mean anything, r(t - t') should rapidly approach zero for $|t - t'| >> \Delta t$. Therefore, since $T >> \Delta t$, for the vast majority of the range of t in the outer integral of equation 5.8, the limits on the inner integral are effectively $\tau = -\infty$ to $+\infty$. Taking

into account that $r(t - t')$ does not depend on the actual value of t (only its separation from t'), the variance becomes

$$\sigma_I^2 = \frac{1}{(\Delta t)^2} \int_{t=0}^{T} \left[\int_{\tau=-\infty}^{+\infty} r(t - t')\, d\tau \right] dt$$

$$= \frac{T}{(\Delta t)^2} \int_{-\infty}^{+\infty} r(t - t')\, d(t - t'). \qquad (5.9)$$

If we have chosen our variability scale (Δt) well, then the integral I is analogous to the sum S used in the case of a finite number of independent measurements. Therefore, the result for the variance of I should be the same as for the variance of S. Then the number of independent measurements in a finite time span T should be $T/\Delta t$. Equating this with the result in equation 5.9 we get

$$\Delta t = \int_{-\infty}^{+\infty} r(t - t')\, d(t - t'). \qquad (5.10)$$

In my investigations, the result in equation 5.10 is not immediately useful. The measured autocorrelation functions are far too noisy to integrate out to infinity. In general, a useful technique is to fit a Gaussian to the autocorrelation function and integrate that. If we can approximate $r(\tau)$ as

$$r(\tau) = \exp[(\tau/\tau_0)^2],$$

then

$$\Delta t = \tau_0 \sqrt{\pi}. \qquad (5.11)$$

I used this method to estimate Δt (for t being both time and East-West distance) as described in equation 5.11. If

the data I dealt with in my analysis were sampled at intervals greater than Δt in both space and time, then the number of independent samples in my data set is equal to the number I counted while analyzing the data. However, if the sampling interval was, in general, smaller, then the maximum number of independent measurements in a single latitude band of length L, in a time T is

$$N_{max} = \frac{L\ T}{\Delta t\ \Delta l}. \qquad (5.12)$$

For purposes of error analysis, I use the smaller of two numbers for the number of measurements in any given subset of the data: the number measured during analysis as discussed near the end of subsection (b.) above, and the number given by the sum of N_{max} (as in equation 5.12) in each of the latitude bands in the subset. The resulting number of independent samples in the 6 days (over a time span of 7 days) of sampling for each latitude band for both land and sea is listed in Table 5.1.

V.C) How cloudiness affects the planetary albedo and fluxes at the top of the atmosphere

The first purpose of this thesis was to determine the effect of clouds, as they presently occur in the earth's atmosphere, on the net radiative flux at the top of the atmosphere. As tabulated in Table 5.2 and illustrated in Figure 5.1, increased total cloudiness is associated, in general, with increased albedo and visible flux and

TABLE 5.1

NUMBER OF INDEPENDENT OBSERVATIONS OF VISIBLE AND INFRARED FLUX FOR 4.5° LATITUDE BANDS

LAT	OCEAN		CONTINENT	
	VIS	INFR	VIS	INFR
1	0.00	0.00	9.48	1.40
2	0.00	0.00	51.05	3.57
3	5.50	0.30	85.22	4.56
4	40.46	1.68	74.80	3.12
5	106.76	4.32	61.74	2.50
6	5.65	13.12	0.34	0.37
7	96.98	23.00	0.00	0.00
8	101.55	24.71	0.00	0.00
9	96.07	48.12	2.04	1.02
10	110.05	110.75	1.87	1.88
11	107.04	90.00	1.81	1.53
12	91.02	59.58	3.14	2.05
13	83.40	36.96	10.43	4.62
14	62.18	20.64	16.36	5.43
15	54.44	20.62	15.55	5.89
16	54.34	28.65	16.80	8.86
17	56.97	24.10	15.37	6.50
18	47.21	14.11	10.90	3.26
19	30.07	12.01	8.73	3.49
20	20.25	11.95	5.47	3.22
21	22.64	13.72	5.66	3.43
22	25.48	17.25	7.40	5.01
23	16.85	14.20	3.89	3.28
24	12.32	10.54	4.67	4.00
25	13.66	8.69	6.01	3.82
26	12.44	7.43	7.92	4.73
27	12.64	7.41	9.56	5.61
28	24.99	10.26	16.85	6.92
29	36.30	20.57	21.02	11.91
30	27.33	23.41	23.91	20.48
31	23.82	21.41	31.15	28.00
32	24.99	21.60	38.14	32.97
33	31.50	28.46	36.00	32.53
34	13.91	18.79	25.83	34.90
35	5.09	10.23	15.27	30.69
36	4.22	7.49	7.30	12.94
37	7.23	8.02	1.81	2.00
38	7.02	7.97	1.62	1.84
39	6.81	6.54	0.85	0.82
40	2.78	2.51	0.00	0.00

decreased infrared flux at the top of the atmosphere. Its association with the net flux (into the atmosphere) depends on the region of the earth being observed and the season in that region. (The visible and albedo results at -67.5° in the 20 LATITUDE grouping, at -63° in the 10 CONTINEN grouping, and at -81° in the 10 OCEANIC grouping should be ignored due to the lack of data in these categories.) The parameters tabulated and graphed here are not simple regression coefficients but rather the regression coefficients multiplied by the appropriate standard deviation of the parameter being regressed. This allows direct comparisons between the effects of different parameters on a given flux, it allows comparisons between the results of single parameter and multiple parameter regressions involving more than one term in a single parameter, and it simplifies the elucidation of the importance of the results for different regions of the Earth on the Earth as a whole (since in some regions there might be very large, negative or positive, coefficients but only very small actual variations in cloudiness, for example). In Figure 5.2, I have graphed the "measured" (as described in section V.B.b above) outgoing fluxes versus total cloudiness for some selected regions of the globe in order to give a better idea what the data used to determine the results (Table 5.2 and Figure 5.1) looked like. Clearly, the data is well distributed and fits the regressions fairly well for most regions.

TABLE 5.2

EFFECT OF TOTAL CLOUD FRACTION ON TOP-OF-THE-ATMOSPHERE ALBEDO AND FLUXES FOR VARIOUS REGIONS OF THE EARTH

20 LATITUDE

LATITUDE	VISIBLE	ALBEDO	INFRARED	NET GAIN
-85.50	0.00	0.0000	-2.93	2.93
-76.50	0.00	0.0000	-4.17	4.17
-67.50	0.18	0.0362	0.23	-0.41
-58.50	0.97	0.0287	-9.28	8.30
-49.50	3.78	0.0509	-11.83	8.05
-40.50	10.71	0.0778	-18.80	8.08
-31.50	15.63	0.0737	-19.98	4.36
-22.50	15.38	0.0583	-19.18	3.80
-13.50	13.47	0.0400	-16.46	2.99
-4.50	18.99	0.0485	-21.21	2.22
4.50	19.57	0.0458	-20.44	0.87
13.50	13.50	0.0311	-21.93	8.44
22.50	12.04	0.0252	-26.81	14.77
31.50	17.94	0.0363	-28.25	10.31
40.50	29.38	0.0586	-21.96	-7.42
49.50	32.84	0.0657	-17.15	-15.69
58.50	32.06	0.0650	-10.26	-21.80
67.50	28.06	0.0566	-9.46	-18.60
76.50	10.08	0.0194	-5.27	-4.80
85.50	7.81	0.0147	-2.82	-4.99

8 LATITUDES

LATITUDE	VISIBLE	ALBEDO	INFRARED	NET GAIN
-78.75	0.00	0.0000	4.07	-4.07
-56.25	1.65	0.0456	-10.56	8.91
-33.75	12.71	0.0804	-22.39	9.68
-11.25	19.26	0.0484	-19.27	0.01
11.25	15.70	0.0412	-24.61	8.90
33.75	21.99	0.0443	-26.76	4.77
56.25	33.39	0.0677	-14.66	-18.74
78.75	18.11	0.0343	-6.42	-11.69

CONTINENTAL

LATITUDE	VISIBLE	ALBEDO	INFRARED	NET GAIN
-69.75	0.42	0.0177	-0.78	0.35
-31.50	10.61	0.0461	-18.49	7.88
0.00	30.51	0.0633	-19.81	-10.70
31.50	26.17	0.0534	-32.79	6.61
69.75	40.45	0.0807	-13.52	-26.93

OCEANIC

LATITUDE	VISIBLE	ALBEDO	INFRARED	NET GAIN
-69.75	2.66	0.0329	-6.36	3.71
-31.50	11.23	0.0861	-24.25	13.02
0.00	24.46	0.0529	-25.74	1.28
31.50	22.68	0.0473	-17.65	-5.03
69.75	14.16	0.0277	-5.62	-8.54

HEMISPHERIC

LATITUDE	VISIBLE	ALBEDO	INFRARED	NET GAIN
-45.00	8.98	0.0865	-19.46	10.48
45.00	24.21	0.0549	-24.40	0.20

WHOLE EARTH

LATITUDE	VISIBLE	ALBEDO	INFRARED	NET GAIN
0.00	22.38	0.0686	-21.02	-1.36

10 CONTINEN

LATITUDE	VISIBLE	ALBEDO	INFRARED	NET GAIN
-81.00	0.00	0.0000	-3.99	3.99
-63.00	0.02	0.0026	-0.78	0.75
-45.00	8.29	0.0784	-26.71	18.42
-27.00	10.23	0.0430	-18.12	7.89
-9.00	22.58	0.0530	-15.94	-6.64
9.00	13.45	0.0371	-19.48	6.03
27.00	23.35	0.0482	-32.05	8.70
45.00	32.53	0.0651	-24.76	-7.77
63.00	38.56	0.0776	-11.53	-27.03
81.00	22.17	0.0428	-6.62	-15.55

10 OCEANIC

LATITUDE	VISIBLE	ALBEDO	INFRARED	NET GAIN
-81.00	0.00	0.0000	-5.75	5.75
-63.00	0.16	0.0413	-8.16	7.99
-45.00	6.06	0.0750	-17.00	10.93
-27.00	16.31	0.0729	-20.81	4.50
-9.00	17.45	0.0451	-20.99	3.54
9.00	19.70	0.0471	-22.64	2.94
27.00	21.42	0.0446	-18.61	-2.81
45.00	31.49	0.0629	-15.08	-16.41
63.00	18.50	0.0375	-5.94	-12.56
81.00	9.26	0.0168	-4.63	-4.63

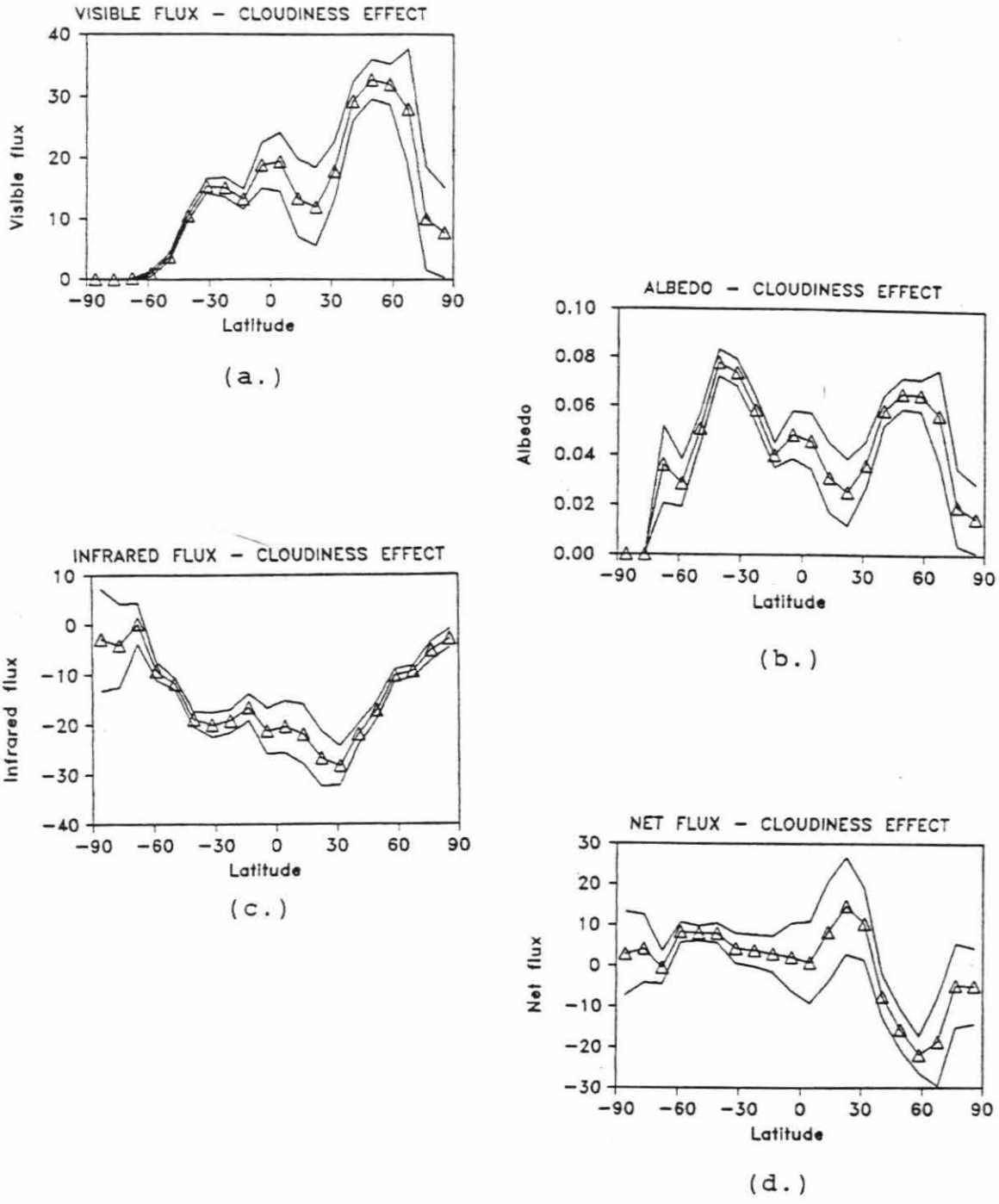

Figure 5.1 Regression coefficient for flux versus total fractional cloud cover times the standard deviation of the cloudiness. The upper and lower lines are the one sigma error limits (where only the error in the regr. coeff. is considered). For the 20 LATITUDE grouping.

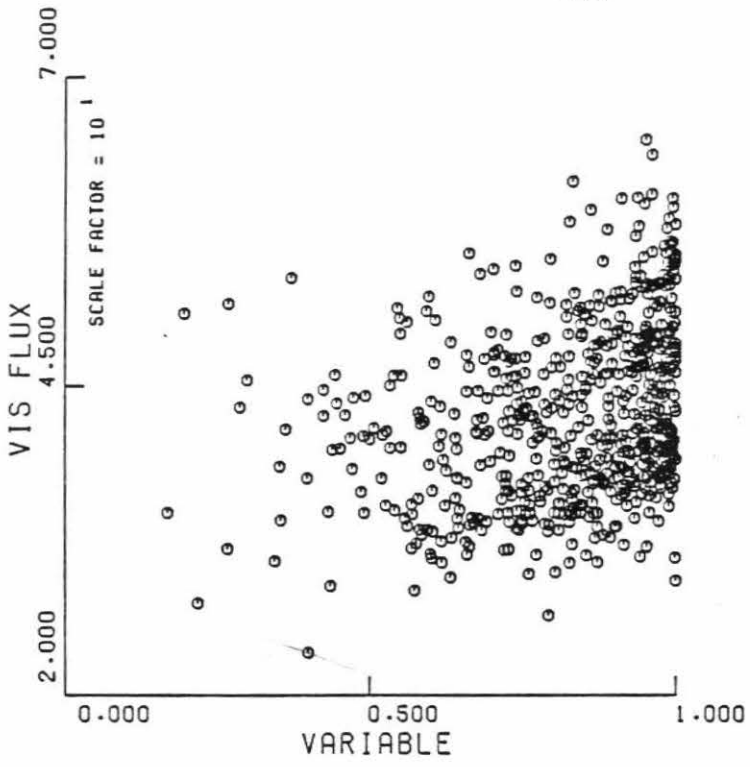

(a.) 54° S - 45° S, all areas

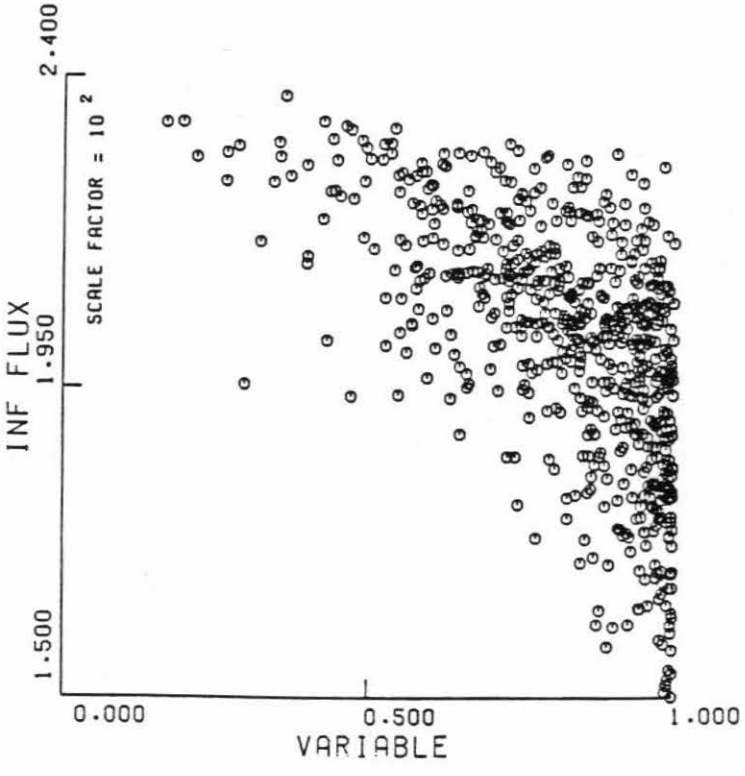

(b.) same as in (a.)

Figure 5.2 "Measured" flux versus total fractional cloud cover. The fluxes should be multiplied by the listed scale factors.

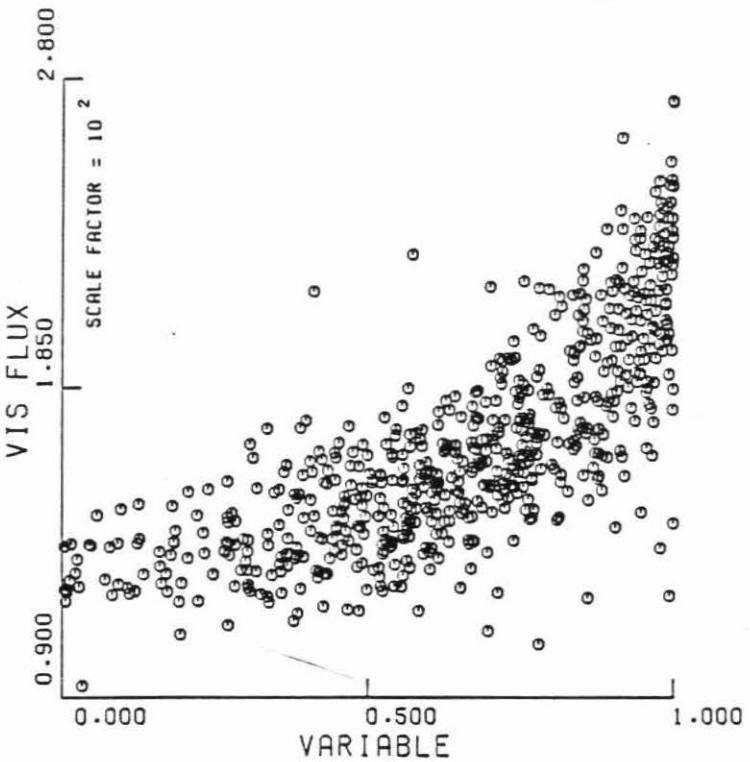

(c.) 36° N - 54° N, continents only

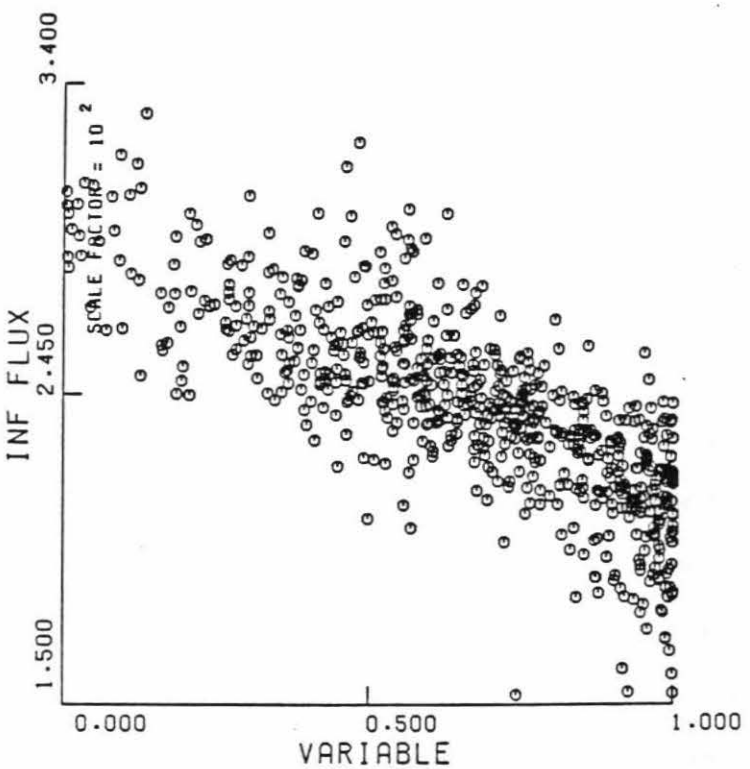

(d.) same as in (c.)

Figure 5.2 (cont.)

One noteworthy aspect of Figure 5.1 is the size of the standard errors relative to the results. This is the unavoidable consequence of having used six days spaced over only one week in June 1979. It turns out that the autocorrelation time for visible and infrared flux in most regions of the Earth is several days. If I had used six days spaced more widely over the month of June, I would have been able to estimate the statistical parameters of interest with greater accuracy.

The seasonal dependence of the cloud-radiation relationships are perhaps their most interesting properties. In winter, when there is little visible flux to change with variations in cloudiness, the effect on the infrared flux dominates, and increased cloudiness is associated with increases in the net flux. In summer, there is a lot of visible flux to be varied and, thus, increases in cloudiness are sometimes associated with decreases in net flux (i.e., the albedo effect dominates). Keeping in mind that the data come from near the northern summer solstice, this is obvious in Table 5.2 and Figure 5.1. This seasonal dependence is especially well demonstrated by the contrast between the cloudiness effects on flux in one day in June 1979 with the same statistics from one day in November 1979 (see Table 5.3 and Figure 5.3). For the Earth as a whole, increased cloudiness is associated with only very small changes in the top-of-the-atmophere net flux, although given the accuracy of the results, these results are consistent

TABLE 5.3

THE AVERAGE OF THE TOTAL CLOUD FRACTION AND ITS EFFECT ON TOP-OF-THE-ATMOSPHERE ALBEDO AND FLUXES FOR ONE DAY IN JUNE 1979 AND ONE DAY IN NOVEMBER 1978

Land and sea - 8 latitudes

	June		November	
	$\langle f_{tot} \rangle$	$\delta F_n(f)$	$\langle f_{tot} \rangle$	$\delta F_n(f)$
1	5.41E-01	1.91E-01	5.25E-01	1.01E+00
2	8.22E-01	8.01E+00	8.89E-01	-4.97E+00
3	6.44E-01	1.08E+01	7.18E-01	-8.61E+00
4	6.54E-01	6.06E-01	7.54E-01	1.39E-02
5	8.57E-01	1.06E+01	7.06E-01	1.22E+01
6	6.46E-01	9.17E+00	6.68E-01	3.68E+00
7	7.66E-01	-2.61E+01	7.61E-01	6.68E+00
8	9.09E-01	-1.58E+01	6.10E-01	4.59E+00

Southern and northern hemispheres

	June		November	
	$\langle f_{tot} \rangle$	$\delta F_n(f)$	$\langle f_{tot} \rangle$	$\delta F_n(f)$
1	6.78E-01	1.12E+01	7.54E-01	-2.54E+00
2	7.73E-01	-2.36E+00	6.98E-01	9.64E+00

Whole earth

	June		November	
	$\langle f_{tot} \rangle$	$\delta F_n(f)$	$\langle f_{tot} \rangle$	$\delta F_n(f)$
1	7.25E-01	-1.58E+00	7.26E-01	-1.22E-01

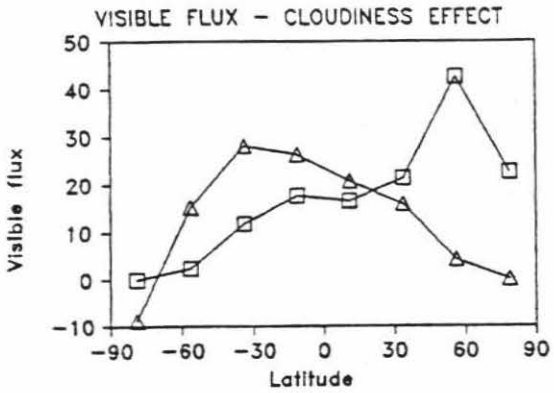

(a.)

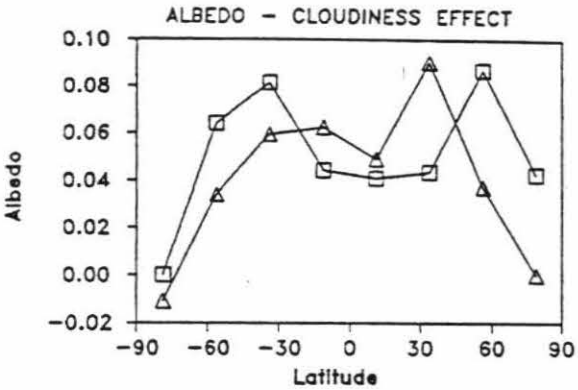

(b.)

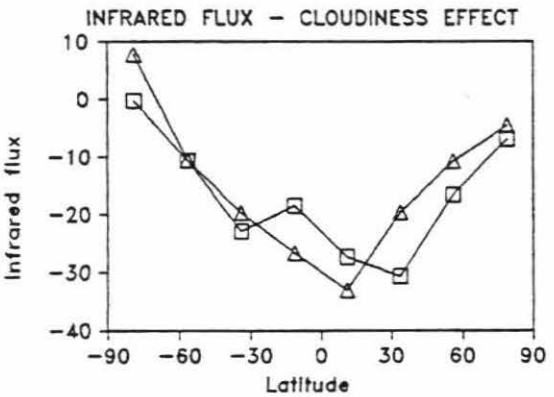

(c.)

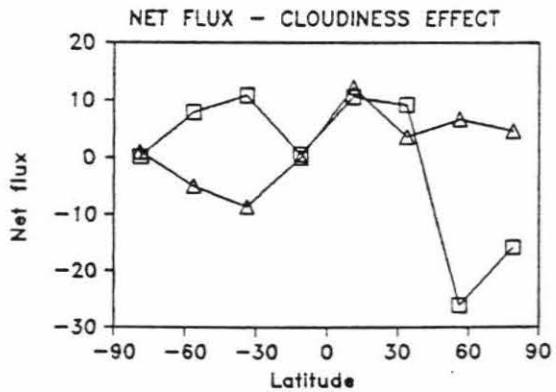

(d.)

Figure 5.3 Same quantities as in Figure 5.1. Contrast between 12 June 1979 (squares) and 28 Nov. 1978 (triangles). For the 8 LATITUDES grouping.

with a zero net effect of clouds over the Earth as a whole. In Table 5.4, I have listed the linear regression coefficients for the various fluxes (and planetary albedo) as functions of total fractional cloud cover. Because the statistical relationship between clouds and outgoing flux, on this scale, could be dominated by the dependence of both on latitude, I have included the coefficients for cloudiness from multiple parameter regressions in which latitude (actually the first and second order Legendre polynomials in the sine of the latitude) was included as an independent variable. For each geographic region in Table 5.4 (NH for northern hemisphere, SH for southern hemisphere, and WE for whole Earth), the first row gives the cloudiness coefficient for the single parameter regression (these are the total derivatives of flux with respect to cloudiness). The second row, in each section, gives the coefficient for regressions involving f_{tot}, $P_1(\sin \lambda)$, and $P_2(\sin \lambda)$, and the third row (where it exists) gives the f_{tot} coefficient for regressions involving f_{tot}, $P_1(\sin \lambda)$, $P_2(\sin \lambda)$, and T_s. It is noteworthy that for each geographic region (and for each analysis - six days in June, one day in June, and one day in November) the inclusion of latitude variables did not have much effect on the derivative of the fluxes with respect to total cloudiness. However, since the greenhouse and albedo effects are nearly balanced (outside of the winter hemispheres) the new coefficients for the net flux were often of opposite sign to the original. In general, for all

TABLE 5.4

REGRESSION COEFFICIENTS FOR FLUX VS. TOTAL CLOUD FRACTION

6DAY 49BA

	VISIBLE	ALBEDO	INFRARED	NET GAIN
SH	33.314	0.32064	-72.176	38.863
	43.180	0.28815	-56.838	13.659
	42.898	0.27462	-57.919	15.021
NH	93.286	0.21172	-94.044	0.758
	89.102	0.18497	-91.046	1.944
	78.443	0.16526	-92.417	13.974
WE	83.838	0.25687	-78.734	-5.104
	70.412	0.25464	-79.549	9.138
	69.202	0.25608	-78.288	9.086

32BIN JUN

	VISIBLE	ALBEDO	INFRARED	NET GAIN
SH	32.354	0.39277	-73.747	41.393
	41.872	0.34361	-57.498	15.626
NH	115.587	0.24814	-106.479	-9.109
	108.120	0.22307	-103.180	-4.939
WE	89.909	0.29767	-84.026	-5.883
	69.261	0.30257	-86.349	17.089

32BIN NOV

	VISIBLE	ALBEDO	INFRARED	NET GAIN
SH	75.035	0.16942	-65.701	-9.334
	73.193	0.16495	-65.053	-8.140
NH	43.418	0.22859	-73.697	30.279
	45.350	0.24304	-71.008	25.658
WE	69.060	0.19177	-68.651	-0.409
	53.852	0.19679	-70.278	16.427

these analyses, it is possible to say that the effect of cloudiness on the net flux balance at the top of the Earth's atmosphere, averaged over the Earth, lies somewhere between -10 W m^{-2} and 20 W m^{-2} for a unit change in cloudiness. This is a quite small result, especially when compared with the results for some of the regions listed in Tables 5.2 and 5.3 (keep in mind that, in Tables 5.2 and 5.3, the changes in flux correspond to changes in cloudiness of less than unity).

As a quick perusal of Table 5.2 reveals, the flux effects of cloudiness are more pronounced for continental areas than for oceanic ones. This is illustrated in Figure 5.4, where I have compared the results of oceanic and continental regions with the results of Figure 5.1.

One problem with these regressions is that they rely on estimates of cloud cover using only infrared THIR data. In the absence of two channel estimates of cloud cover, several systematic errors are possible. Perhaps the most serious problem with these estimates is confusion between regions of clear surface and regions of low-altitude clouds (L. Stowe, personal communication 1982). Low clouds have an especially lopsided effect on the net radiation. Since the temperature of a low cloud is nearly that of the underlying surface, its effect on the emitted longwave flux is small. However, its effect on the albedo is not substantially diminished by being low altitude. For this reason, I have performed multiple regressions on the fluxes for the three altitude

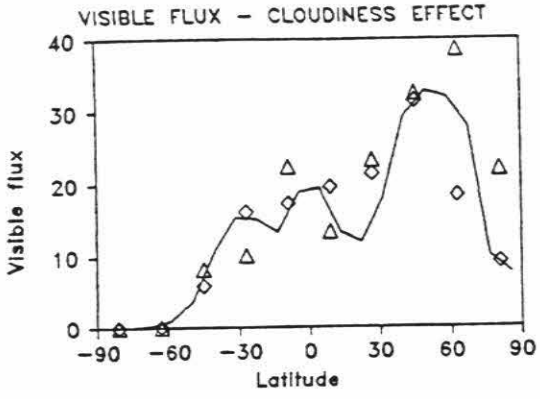

(a.)

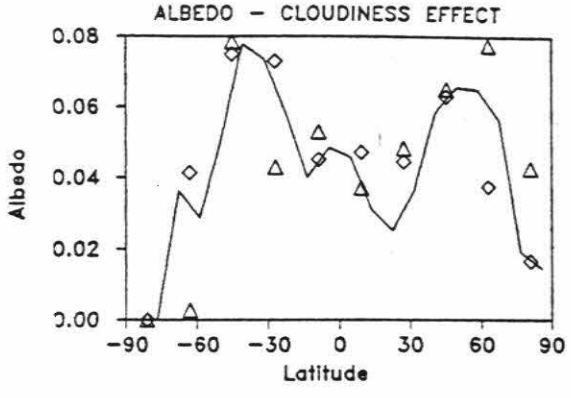

(b.)

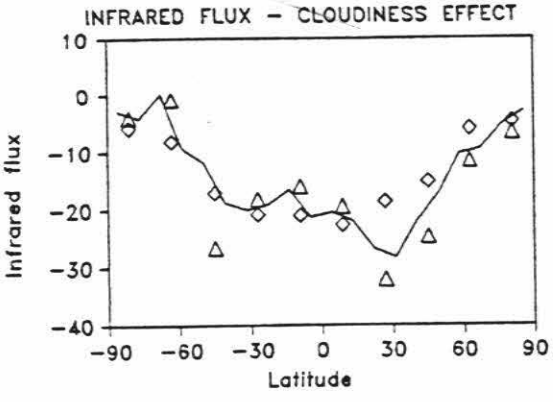

(c.)

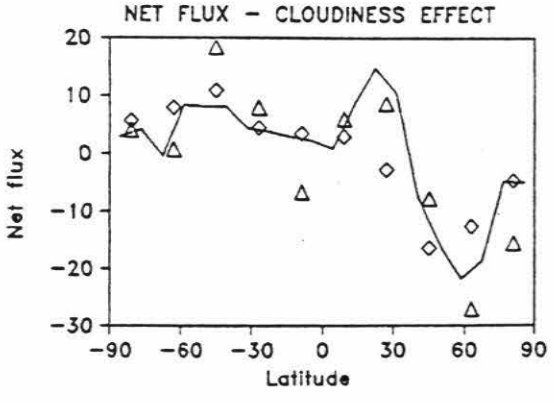

(d.)

Figure 5.4 Same quantities as in Figure 5.1. Contrast between oceans (squares), land (triangles), and all areas (line).

classifications of cloud cover. The regression coefficients (a_{low}, a_{mid}, and a_{high}) for planetary albedo, emerging shortwave and longwave flux, and the net (gain) flux for the 8 LATITUDE geographic grouping are presented in Table 5.5. Clearly, there are some problems with the low cloud statistics. There should not be increases in emitted longwave flux with increasing amounts of low altitude cloudiness, when the amounts of mid and high altitude cloud cover are held constant. Furthermore, there should be greater positive changes in planetary albedo with increases in low cloud cover (when the other two cloudinesses are held constant).

To what extent are the associations between top-of-the-atmosphere fluxes and total cloudiness non-causal, but due to the association of each of these parameters with other variables? To illustrate this, I have performed multiple parameter regressions on the visible flux, albedo, and infrared flux. The parameters I chose for these regressions were the simplest I could think of for a nearly complete explanation of the flux leaving any given area. If the cloudiness measured is closely related to the actual cloudiness existing in a given area, if surface temperature is closely related to the entire vertical temperature structure in the same area, and if the surface albedo measured is the real surface albedo, then these three parameters should define the top-of-the-atmosphere albedo and infrared flux for the area. I did multiple regression

TABLE 5.5

REGRESSION COEFFICIENTS FOR TOP-OF-THE-ATMOSPHERE RADIATION FOR THREE CLOUD TYPE MULTIPLE REGRESSION FOR THE 8 LATITUDES

GEOGRAPHIC GROUPING

		a_{low}	a_{mid}	a_{high}
1	a	0.000E+00	0.000E+00	0.000E+00
	v	0.000E+00	0.000E+00	0.000E+00
	i	4.953E+01	6.292E+01	-1.484E+01
	n	-4.953E+01	-6.292E+01	1.484E+01
2	a	1.878E-02	1.991E-01	3.327E-01
	v	2.614E+01	1.129E+01	1.869E+01
	i	3.844E+00	-3.977E+01	-8.739E+01
	n	-2.998E+01	2.848E+01	6.870E+01
3	a	1.955E-01	2.473E-01	4.189E-01
	v	1.707E+01	4.804E+01	5.697E+01
	i	-3.987E+01	-5.290E+01	-1.405E+02
	n	2.280E+01	4.860E+00	8.353E+01
4	a	2.699E-02	1.730E-01	2.915E-01
	v	2.200E+01	6.120E+01	1.209E+02
	i	-2.260E+01	-4.603E+01	-1.547E+02
	n	6.000E-01	-1.517E+01	3.380E+01
5	a	-8.056E-03	1.078E-01	2.893E-01
	v	-1.497E+01	3.611E+01	1.162E+02
	i	-3.560E+01	-6.214E+01	-1.701E+02
	n	5.057E+01	2.603E+01	5.390E+01
6	a	-1.690E-02	1.221E-01	2.604E-01
	v	-8.881E+00	6.059E+01	1.296E+02
	i	-4.936E+01	-6.759E+01	-1.386E+02
	n	5.824E+01	7.000E+00	9.000E+00
7	a	2.046E-01	2.741E-01	3.741E-01
	v	9.995E+01	1.356E+02	1.841E+02
	i	-2.441E+01	-4.968E+01	-9.336E+01
	n	-7.554E+01	-8.592E+01	-9.074E+01
8	a	-4.408E-02	1.824E-01	1.763E-01
	v	-2.789E+01	9.980E+01	8.369E+01
	i	-4.035E+00	-2.726E+01	-5.078E+01
	n	3.192E+01	-7.254E+01	-3.291E+01

analysis for albedo (and for visible flux) versus surface albedo, total cloudiness, and the product of these two. I did multiple regression analysis for infrared flux versus surface temperature, total cloudiness, and the product of these two. I then determined the effect on the net flux of a one standard deviation change in the total cloudiness given average conditions in the other variables. I used the the regressions,

$$F_v = c_0 + c_1 f_{tot} + c_2 \alpha_s + c_3 \alpha_s f_{tot},$$

and

$$F_i = d_0 + d_1 f_{tot} + d_2 T_s + d_3 T_s f_{tot}.$$

Therefore,

$$\delta F_n(f_{tot}) = -(c_1 + d_1 + c_3 \langle\alpha_s\rangle + d_3 \langle T_s\rangle) \delta f_{tot}. \quad (5.13)$$

These results are compared with the comparable results for the single parameter regression (as illustrated in Figure 5.1d) in Figure 5.5. Interestingly, the effects of changes in total cloudiness on the top-of-the-atmosphere fluxes did not differ much, for most regions of the world, between the single parameter regressions and the multiple regressions. It is probably safe to assume, then, that the relationships between top-of-the-atmosphere albedo and infrared flux and total fractional cloudiness are causal.

These relationships are quite interesting in terms of their effect on climate prediction. If cloudiness does not vary too much between summer and winter, then the major effect of clouds on the climate should be to dampen seasonal climatic excursions. If there are usually more clouds in

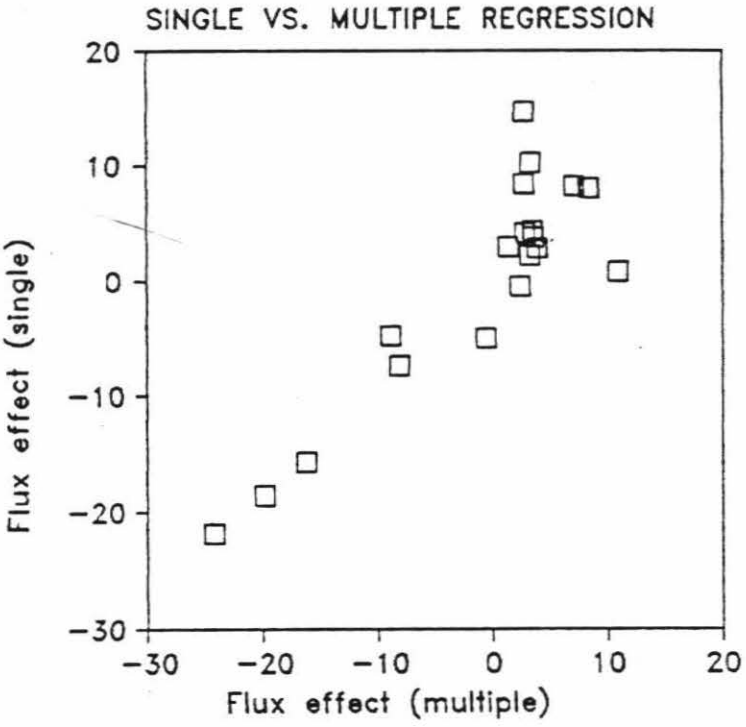

Figure 5.5 Comparison of the effect on the net flux of a one standard deviation change in total fractional cloud cover for the single parameter regression versus the same thing for the regression versus cloudiness, surface albedo, and surface temperature.

the winter than in the summer, then clouds should be warming the globe by the greenhouse effect. However, if there are usually more clouds in the summer than in the winter, then clouds should be cooling the globe by their effect on the albedo. In the limited data set I analyzed, there seems to be only a slight increase of total cloudiness in summer over that in winter. The lack of a clear correlation between the average cloudiness in an area and the effect of increasing cloudiness on the net flux in that area (a function of the local season for the most part) is illustrated in Figure 5.6. Another interesting possibility is that with clouds influencing the radiation balance in a region, the radiation balance influencing the temperature structure, and the temperature influencing the cloudiness, potentially feedback loops could be set up. In Figure 5.7, I plot the total derivative of net flux with respect to total cloudiness against the total derivative of cloudiness with respect to surface temperature. Several interesting features are apparent. First, in the tropics (18° S to 18° N) the potential for cloudiness - temperature feedback is clear. Increases in surface temperature are associated with increases in cloud cover (not surprising in a region in which the dominant form of cloud depends on a warm moist boundary layer to initiate moist convection). The increase in cloudiness results in (or is associated with) an increase in the net flux retained by the cloudy region (the penetrative moist convection common to tropical cloud

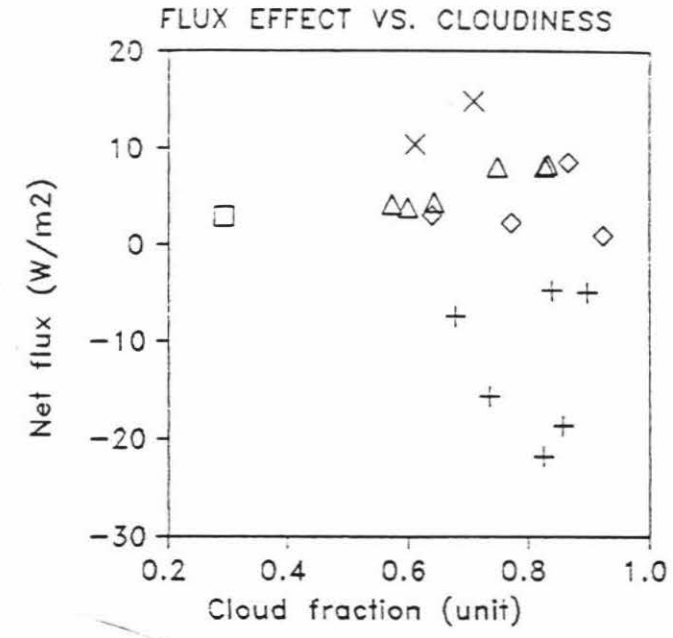

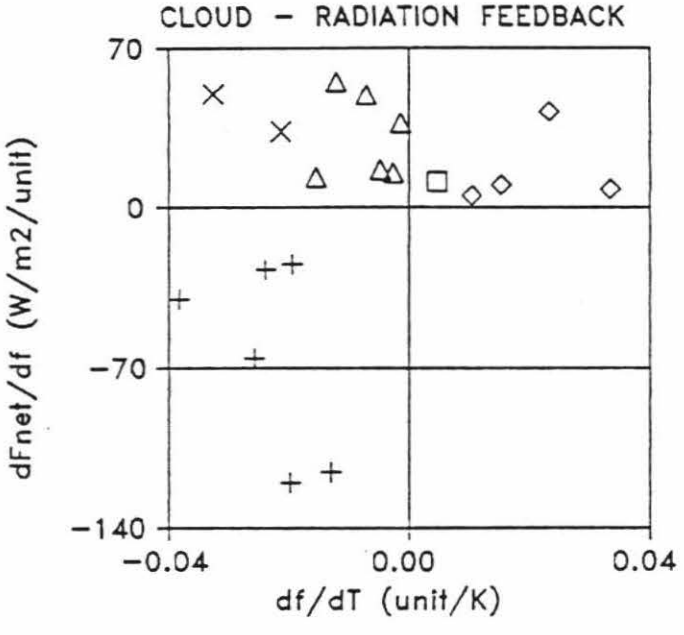

Figure 5.6 (top) Effect of cloudiness on the net flux versus the average cloudiness for various latitudes. Squares: 90° S - 81° S. Triangles: 81° S - 18° S. Diamonds: 18° S - 18° N. Exes: 18° N - 36° N. Crosses: 36° N - 90° N.

Figure 5.7 (bottom) Regression coefficient for net flux against cloudiness versus the same for cloudiness against surface temperature. Same symbols as in Figure 5.6.

clusters results in very high cold cloud tops). This, then, can result in the raising of the surface temperature which in its turn can increase cloud cover still further. The high latitudes in the northern (summer) hemisphere (36° N to 90° N) have the potential for a feedback loop of the opposite sign. Here, decreases in temperature are associated with increases in cloudiness (perhaps due to greater cloud cover in polar air masses or simply the result of the condensation, by cooling, of moisture in the atmosphere). The increase in cloud cover leads to a decrease in the net flux absorbed in the region. This decreased absorption could lead to further decreases in temperature and increases in cloudiness. The middle and high latitudes in the southern (winter) hemisphere (81° S to 18° S) show evidence of radiation - cloudiness - temperature relationships that should stabilize all three. Here a decrease in temperature would be associated with an increase in cloudiness (with the same sort of rationale as in the northern high latitudes). The increase in cloudiness should be associated with an increase in the net flux (as expected in the winter when sunlight is less important) which should offset the decrease in temperature that began it all. Clearly, this has to be investigated further.

V.D) Simple diagnostic equations for albedo and outgoing infrared flux at the top of the atmosphere

One of the basic assumptions of simple energy balance climate models is that one can calculate (to within the error budgeted for the model) the planetary albedo of an area and the radiation of terrestrial (infrared) energy to space from such an area given some simple meteorological and climatic data for that area. The sort of data commonly used for calculating the top-of-the-atmosphere radiation in such models includes the surface temperature and surface albedo. In some more complex models in this class, more sophisticated data, such as mid-level atmospheric temperature and height and the nature (continent or ocean) of the surface, are used.

I investigated several different regressions that might be of use in simple climate models. The first and most obvious is of the form

$$F_i = a_0 + a_1 T_s$$
$$\alpha = b_0 + b_1 T_s. \qquad (5.14)$$

More complicated regressions include

$$F_i = a_0 + a_1 T_s + a_2 T_s^2 + \ldots + a_n T_s^n$$
$$\alpha = b_0 + b_1 T_s + b_2 T_s^2 + \ldots + b_n T_s^n, \qquad (5.15)$$

$$F_i = a_0 + a_1 T_s + a_2 f_{tot}$$
$$\alpha = b_0 + b_1 T_s + b_2 f_{tot}, \qquad (5.16)$$

and

$$F_i = a_0 + a_1 T_s + \ldots + a_n T_s^n + a_{n+1} \alpha_s$$
$$\alpha = b_0 + b_1 T_s + \ldots + b_n T_s^n + b_{n+1} \alpha_s. \qquad (5.17)$$

The regressions described in equations 5.14 and 5.16 are not original with this study. Moreover, the 5.16 regressions are of dubious value in simple climate models (since predicting cloudiness generally requires more sophisticated models). The primary purpose of these regressions is for comparison with previous studies by other investigators. However, the regressions 5.15 and 5.17 are new, explain a larger fraction of the variance than regressions 5.14, and may prove to be useful in simple climate models carried on time and space scales similar to those used in this study.

In Table 5.6, I list the results for the infrared regression coefficient a_1 and for the albedo regression coefficient b_1 (in equations 5.14 and 5.16) for various single and multiple parameter regressions, for the whole globe and both hemispheres, for both time and space scales investigated. Table 5.7 consists of the results of previous studies for comparison. The format of Table 5.7 owes much to the tables in Ohring and Gruber (1983) and in Warren and Schneider (1979). The most obvious comparison is that my global infrared regression coefficients are larger than most of the corresponding coefficients from other studies. The results of others that come closest to my values include those of Warren and Schneider (1979) for all of the Earth excluding latitudes south of 70° S, the coefficient of Oerlemans and Van den Dool (1978) in which Antarctic data were specially treated to simulate the sort of temperatures one would expect without the severe low level inversion

TABLE 5.6

REGRESSION COEFFICIENTS FOR TOP-OF-THE-ATMOSPHERE ALBEDO AND EMITTED LONGWAVE FLUX IN TERMS OF SURFACE TEMPERATURE

		3 day zonal targets	1 day 500km targets
Albedo coefficients:			
T_s	global	-.00637	-.00603
T_s, f_{tot}		-.00642	-.00585
T_s, λ			-.00024
T_s, f_{tot}, λ			.00097
T_s	Northern hemisphere	-.00867	-.00845
T_s, f_{tot}		-.00856	-.00775
T_s, λ			-.00789
T_s, f_{tot}, λ			-.00540
T_s	Southern hemisphere	-.00672	-.00618
T_s, f_{tot}		-.00594	-.00584
T_s, λ			.00753
T_s, f_{tot}, λ			.00537
excluding Antartica:			
T_s	global	-.01046	-.00932
T_s, f_{tot}		-.00954	-.00851
T_s	Southern hemisphere	-.01285	-.01097
T_s, f_{tot}		-.01087	-.00961
Longwave flux coefficients:			
T_s	global	2.50	2.27
T_s, f_{tot}		2.51	2.21
T_s, λ			1.23
T_s, f_{tot}, λ			0.86
T_s	Northern hemisphere	1.42	1.41
T_s, f_{tot}		1.37	1.07
T_s, λ			1.02
T_s, f_{tot}, λ			-0.38
T_s	Southern hemisphere	3.02	2.69
T_s, f_{tot}		2.96	2.62
T_s, λ			-0.03
T_s, f_{tot}, λ			0.43
excluding Antartica:			
T_s	global	2.36	2.01
T_s, f_{tot}		2.05	1.71
T_s	Southern hemisphere	3.21	2.57
T_s, f_{tot}		2.69	2.17

TABLE 5.7

REGRESSION COEFFICIENTS FOR OUTGOING INFRARED FLUX IN TERMS OF SURFACE TEMPERATURE FROM EARLIER STUDIES

Budyko (1975)			
	T_s	zonal means, global	1.67
Cess (1976)			
	T_s, f_{tot}	annual zonal means, N. hem.	1.57
Warren and Schneider (1979)			
	T_s	annual zonal means, global	1.78
		same, excluding 70° - 90° S	2.17
		monthly means, global, varying latitudes	1.83
Oerlemans and Van den Dool (1978)			
	T_s	annual zonal means, global	2.23
Ohring and Clapp (1980)			
	T_s, f_{tot}	seasonal means, N. hem., varying latitudes	1.8
Simmonds and Chidzey (1982) (using data from Winston et al., 1979)			
annual average data:			
	T_s	global	1.56
	T_s, f_{tot}	global	1.49
	T_s, f_{tot}, T_s f_{tot}	global	1.98
	T_s, f_{tot}, T_s f_{tot}	Northern hemisphere	2.96
	T_s, f_{tot}, T_s f_{tot}	Southern hemisphere	1.60
seasonal data:			
	T_s	global	1.59
	T_s, f_{tot}	global	1.55
	T_s, f_{tot}, T_s f_{tot}	global	2.06
	T_s, f_{tot}, T_s f_{tot}	Northern hemisphere	2.42
	T_s, f_{tot}, T_s f_{tot}	Southern hemisphere	1.85

Chen and Ohring (1983)

			zonal average	90 km target
T_s	4/17/79	N. hem.		3.08
T_s	7/30/79	N. hem.		3.24
T_s, f_{tot}	4/17/79	N. hem.	1.69	1.79
T_s, f_{tot}	7/30/79	N. hem.	0.71	0.76
T_s	4/17/79	S. hem.		2.93
T_s	7/30/79	S. hem.		1.68
T_s, f_{tot}	4/17/79	S. hem.	2.31	2.12
T_s, f_{tot}	7/30/79	S. hem.	2.47	2.43

typical of Antarctica, the results of Simmonds and Chidzey (1982), and those of Chen and Ohring (1983) for the two parameter regression (the single parameter regression coefficients were derived from a data set in which $f_{tot} < 5\%$). As a quick perusal of Figure 5.8 indicates, eliminating the 10 data points from south of 67.5° S (what was done in the "excluding Antartica" calculations of Table 5.5) lowers the infrared regression coefficient for the global regression of the 3 day zonal average data, thus bringing it closer to the other global estimates. Another indication of the unusual nature of the southern data is the fact that the regression coefficients from this study for the Northern hemisphere (3 day zonal averages) agree quite well with Northern hemisphere coefficients from other studies. The Southern hemisphere relation is steeper than that for the Northern hemisphere, and the relations for the 3 day zonal average data are slightly steeper than those for the 500 km target area daily averaged data. If we compare the results of a more detailed regression between outgoing infrared flux, surface temperature, and cloudiness, we see a similar relationship. Budyko (1969) utilized average monthly meteorological data and calculations of outgoing radiation for 260 stations distributed uniformly about the Earth to derive

$$F_{inf} = -386 + 387\, f_{tot} + 2.23\, T_s\, (1 - 7.13\, f_{tot}),$$

where F_{inf} is expressed in W m^{-2}, f_{tot} is expressed in fractions of a unit, and T_s is expressed in K. This

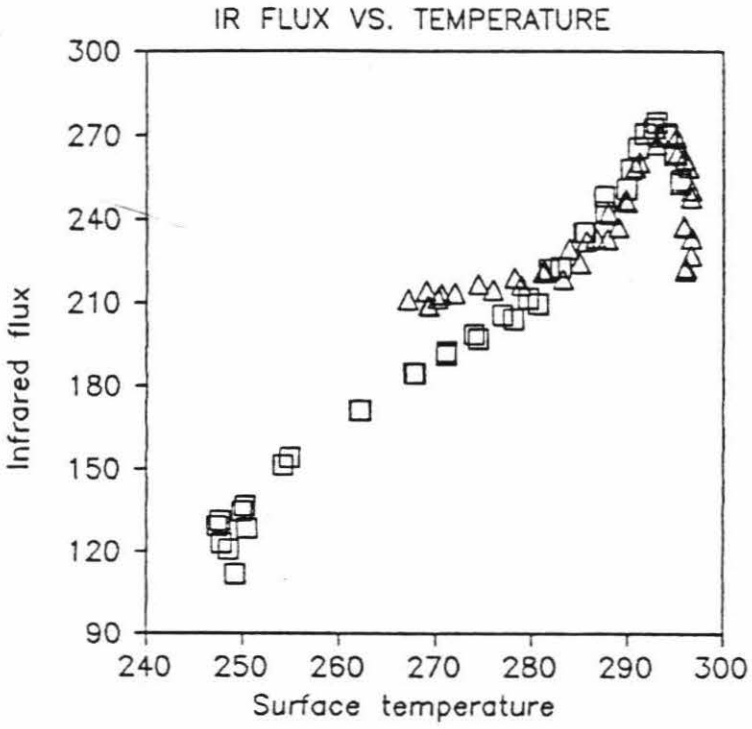

Figure 5.8 Zonal 3 day average of emerging infrared flux versus zonal 3 day average of surface temperature. Squares: 90° S - equator. Triangles: equator - 90° N.

compares to my regression (using daily averaged target area data)

$$F_{inf} = -687 + 406\ f_{tot} + 3.40\ T_s\ (1 - 0.491\ f_{tot}),$$

using the same units. Note that both the partial derivative of F_{inf} with respect to T_s and the total derivative is larger in my regression than in Budyko's. Perhaps as we deal with a smaller range of time over which we average the data, and as we use data from an increasing range of environments, we are dealing with greater extremes of temperature and the true relation (to the extent that there is just one definable relation) between temperature and emitted longwave flux steepens with increasing temperature deviation. My data came from a single week (and a week near one of the solstices, at that) and the data were not averaged over such a long time span that large temperature deviations would be overwhelmed by all the other data. Simmonds and Chidzey utilized a data set (from Winston et al., 1979) that included data believable over a broader range of latitudes (including the poles) than had been used for most of the earlier studies. Chen and Ohring utilized data from only a couple of days, averaged over less than a day, thus accentuating the importance of any possible small temperature excursions on the results.

Before using a linear relationship between surface temperature and outgoing infrared flux derived from this data set, I would like to examine the effect of including data from the rest of the year on the regression

coefficients and on the differences between regressions carried out for different scales of time and space averaging. However, it might be argued that using data from the winter hemisphere near the solstice is best for determining diagnostic radiation equations applicable to times such as ice ages, in which latitudinal temperature gradients are enhanced. In this case, the large infrared flux vs. temperature regression coefficients would indicate a significantly less sensitive and more stable Earth climate in conditions of reduced insolation or less equable climate for Budyko-Sellers type models than most investigations of that sort usually investigate. The reader is referred to the discussion in Warren and Schneider (1979), especially their figure 6 (p. 1390). This brings up the second comparison possible in Tables 5.6 and 5.7. That is that the Northern hemisphere (in northern summer) is probably less stable (more sensitive to temperature perturbations) than the Southern hemisphere. The reason is the decreased infrared flux buffering of surface temperature in the Northern hemisphere relative to the Southern. The values for the albedo - temperature regression coefficient in the Southern hemisphere (and for the entire Earth) are greater when including Antartic data than when not doing so. I would claim that using the Antarctic data is useful here though. The point is that in mid-winter, the effect of any variable in a region including the pole, on the top-of-the-atmosphere albedo should be reduced because some part of the

region has an unvarying (and undefined) albedo due to the lack of insolation. Then the Southern hemisphere is also more stable relative to temperature perturbations in the albedo effect of the temperature as well as the infrared flux effect.

Whether or not the simple regressions are useful, I believe that the data set I utilized in this study is adequate for determining more detailed relationships between surface temperature and surface albedo (easily predicted variables in energy balance climate models) and outgoing infrared flux and top-of-the-atmosphere albedo. Specifically, I have derived polynomial descriptions of this relationship for the smaller spatial and time scale. Although I may not have enough data to define how to weight data from different temperature and radiation regimes so as to derive the correct average linear relationship, I do have data from a broad enough range of temperatures to define a polynomial in surface temperature that should be usable for most temperatures found on the Earth. The following are examples of these regressions along with their multiple correlation coefficients.

Global (1 day, 500 km) data set:

$$F_i = 1090 - 54.4\ T_s + .341\ T_s^2 - 5.63 \cdot 10^{-4}\ T_s^3 + 186\ \alpha_s \qquad (R = .714)$$

$$\alpha = 1.77 - .107\ T_s + 7.28 \cdot 10^{-4}\ T_s^2 - 1.30 \cdot 10^{-6}\ T_s^3 + .230\ \alpha_s \qquad (R = .631).$$

Northern hemisphere (1 day, 500 km) data set:

$$F_i = -1490 + 3.25\ T_s + 9.81\cdot10^{-3}\ T_s^2 + 7.74\cdot10^{-5}\ T_s^3 - 2.74\cdot10^{-7}\ T_s^4 + 119\ \alpha_s \qquad (R = .417)$$

$$\alpha = 6.12 - .0117\ T_s - 3.13\cdot10^{-5}\ T_s^2 - 2.55\cdot10^{-7}\ T_s^3 + 9.09\cdot10^{-10}\ T_s^4 + .147\ \alpha_s \qquad (R = .632).$$

Southern hemisphere (1 day, 500 km) data set:

$$F_i = 260 - 4.19\ T_s - 6.52\cdot10^{-4}\ T_s^2 + 1.20\cdot10^{-4}\ T_s^3 - 2.36\cdot10^{-7}\ T_s^4 + 14.1\ \alpha_s \qquad (R = .800)$$

$$\alpha = -.0776 - .0161\ T_s + 1.72\cdot10^{-4}\ T_s^2 - 3.43\cdot10^{-7}\ T_s^3 - 1.48\cdot10^{-10}\ T_s^4 + .445\ \alpha_s \qquad (R = .719).$$

For comparison with the regressions above single parameter regressions (in T_s) and two parameter regressions (in T_s and α_s) have the following correlation coefficients:

		F_i	α
Global	r:	0.632	-0.538
	R:	0.632	0.548
N. hem.	r:	0.318	-0.601
	R:	0.398	0.618
S. hem.	r:	0.779	-0.551
	R:	0.782	0.631.

V.E) Statistics of use in testing general circulation models and synoptic scale variables diagnostic of cloudiness

Probably a better way of simulating climate and climatic change than using simple energy balance climate models is the use of general circulation models, in which the atmosphere (and increasingly in recent years, the oceans and the land surface) is modeled on a much finer scale using the momentum, energy, and continuity equations derived from first principles. However, in order to calculate what is

happening in the atmosphere in a finite amount of time, various approximations are made. Two major problems are associated with the calculations of atmospheric radiation in GCMs. First, there are the approximations used to determine the radiation field given various meteorological parameters (including cloudiness). The second major problem in GCMs involves predicting the amount and form of cloudiness (especially those forms that are controlled on scales finer than the spatial scale used in the model). Any statistics obtained from the real atmosphere, involving measurements of the radiation field (including upwelling radiation to space), should be of use in testing the parameterizations and approximations used in a GCM. In the past, GCMs have been tuned in order to match the average values of various meteorological variables for large regions over long times. However, to my knowledge this is the first attempt to gather statistics (i.e., covariances) of more than one variable at a time (including top-of-the-atmosphere radiation) at a synoptic scale for eventual use in comparisons with the internal statistics generated by GCMs.

Averages of the variables listed in Table 4.1 and the covariances of these variables with each other have been calculated for the various regions of the earth described in Table 4.2. As yet, no comparisons of these statistics have been made with any GCM results. The results are available, however, to anyone wishing to do such a comparison. Another use of the sort of study that I have made, is to determine

the degree to which different meteorological variables (that various models use as diagnostics for cloudiness and the radiation field) are correlated with upwelling radiation and to determine how such correlations depend on the region of the earth and time of year being observed.

(a.) The success and failure of various cloudiness and radiation diagnostics

Variables 26 through 33 were included in this study specifically because they should be fairly highly correlated with cloudiness. Variables 26 through 29 were chosen to be diagnostic of synoptic scale (resolved at the spatial scale of the FGGE Level III-b analyses) cloudiness and variables 30 through 33 were chosen to be diagnostic of convective and mesoscale cloudiness (of smaller horizontal extent than the resolution of the FGGE Level III-b analyses). Although the use of these variables as diagnostic of cloudiness is a simpler scheme than the sort of techniques used in most general circulation models, the choice of variables was influenced by discussions in Sarachik (1981) and Lindzen (1981) on the generation and parameterization of clouds in atmospheric models. One of the more interesting points in Lindzen's review of convective cloud generation schemes is that simple convective adjustment schemes seem to work better than more complicated schemes such as that developed by Arakawa and Schubert (1974), at least for simulating vertical heat and moisture budgets in the tropical marine

atmosphere (the most important environment for radiatively important convective and mesoscale cloudiness). Thus, although the parameters I used in this study are relatively simple, there is no reason to believe that they are useless in the prediction of cloud and radiation fields.

In Figure 5.9, I have plotted the variation with latitude of the correlation coefficients for planetary albedo and emerging infrared flux with four of these eight variables (chosen for their larger correlation) for all regions, continents only, and oceans only. The first point about these correlations is that, excluding infrared flux in the Antartic, nowhere do any of these variables explain as much as 50% of the variance of the radiation. Clearly, for these parameterizations to be useful, they must be used in concert. Note that large scale cloudiness predictors do a better job in the higher latitudes and convective cloudiness predictors do a better job in the low latitudes. This is especially over the oceans. Moreover, it is encouraging that the flag type cloudiness diagnostic variables (n_{cld} and $f(\delta_H) \cdot g(\omega)$) are generally better correlated with the radiation than physical quantity variables (such as z_{cld}, σ_{H2O}, or δ_H). This is especially encouraging when one takes into account that no tuning of the cutoff points or curvature of the flag functions (as described in Chapter 4) was done.

The correlation coefficients for multiple regressions using some of these cloudiness predictors are presented in

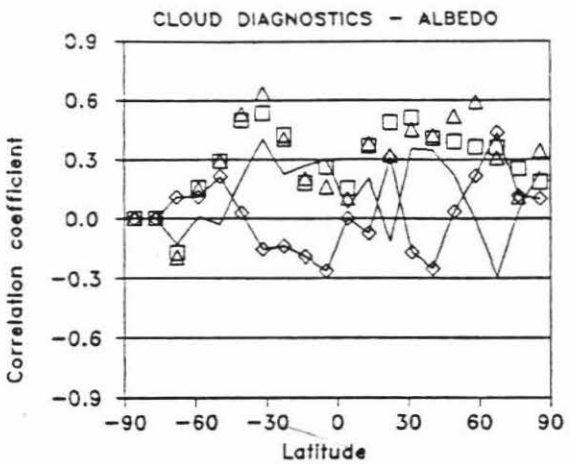

(a.) all areas,
20 LATITUDE grouping

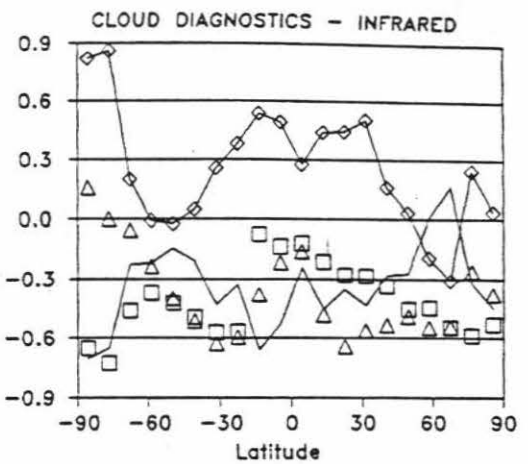

(b.) same as in (a.)

Figure 5.9 Single parameter correlation coefficients for albedo and infrared flux with various cloudiness predictors versus latitude. Squares: z_{cld}. Triangles: n_{cld}. Diamonds (on a line): δ_H. Simple line: $f(\delta_H) \cdot g(\omega)$.

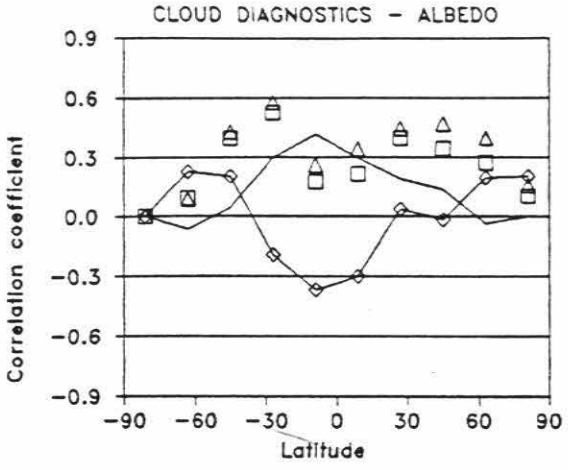

(c.) oceans only,
10 OCEANIC grouping

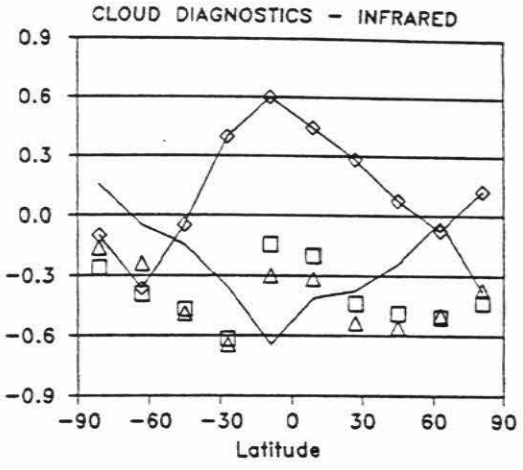

(d.) same as in (c.)

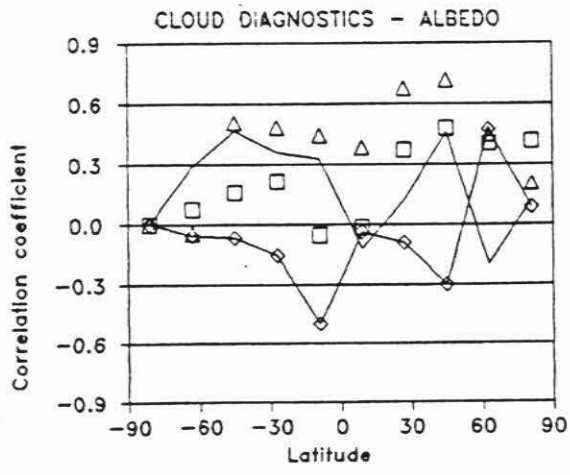

(e.) continents only,
10 CONTINEN grouping

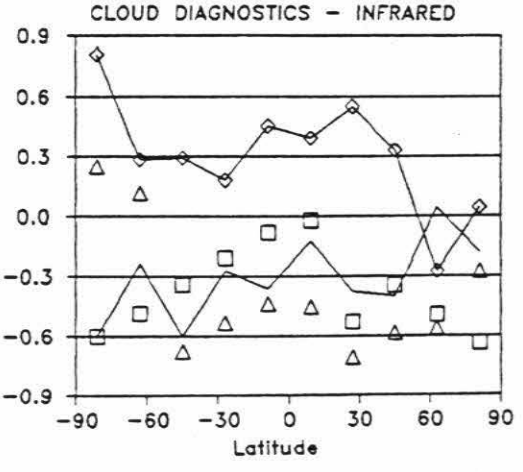

(f.) same as in (e.)

Figure 5.9 (cont.)

Figure 5.10. The multiple regression coefficients for four different sorts of regressions are plotted. The first regression serves as a sort of upper limit to how well one can hope to simulate the planetary albedo and the emerging infrared flux. This regression uses f_{low}, f_{mid}, f_{hi}, and α_s and $f_{tot} \cdot \alpha_s$ for albedo, and T_s and $f_{tot} \cdot T_s$ for infrared flux as the independent variables. The second regression is a mindless application of FGGE Level III-b variables along with some surface information to determine how much better intentional cloudiness diagnostic parameters work than the basic data from which they are derived. This regression uses z_{500}, T_{500}, T_{1000}, p_s, r_s, u_{500}, v_{500}, α_s, and z_s as independent variables. The third regression includes physical predictors for large scale cloudiness and for convective cloudiness along with basic surface parameters. The independent variables are T_s, σ_{H2O}, δ_H, and α_s here. The fourth regression includes flag type predictors for large scale cloudiness and for convective cloudiness along with basic surface parameters. The independent variables here are T_s, n_{cld}, $f(\delta_H) \cdot g(\omega)$, and α_s.

A number of interesting features can be seen in Figure 5.10. There are regions of the Earth in which the meteorological parameter regressions explain fairly large fractions (often more than half) of the variance of the radiation (unlike the case for single parameter regressions). The correlations are better in the northern mid latitudes, over continents, and for infrared flux.

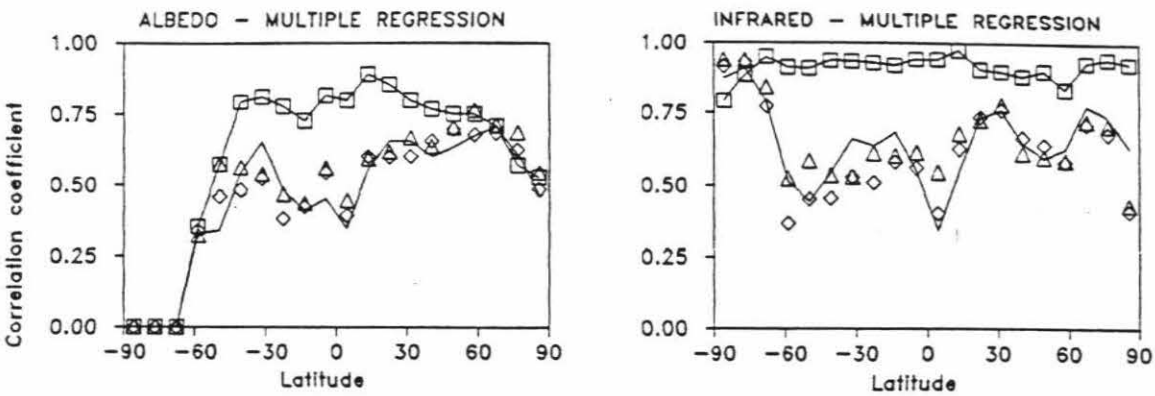

(a.) all areas,
20 LATITUDE grouping

(b.) same as in (a.)

Figure 5.10 Multiple correlation coefficients for albedo and infrared flux for various cloudiness multiple regressions. Squares (on a line): regression versus THIR derived cloudiness variables. Triangles: "mindless" regression versus numerous simple FGGE variables. Diamonds: regression versus several cloudiness predictors of physically meaningful nature. Simple line: regression versus the "flag" type cloudiness predictors.

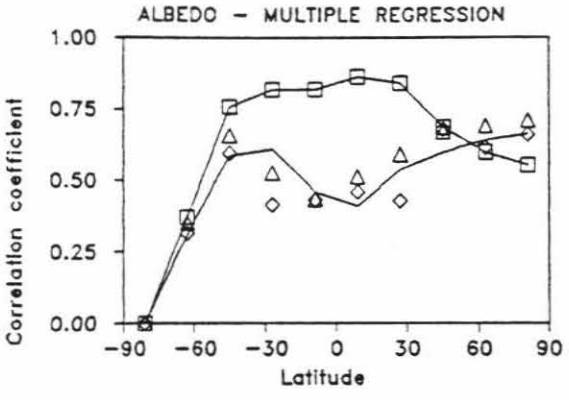

(c.) oceans only,
10 OCEANIC grouping

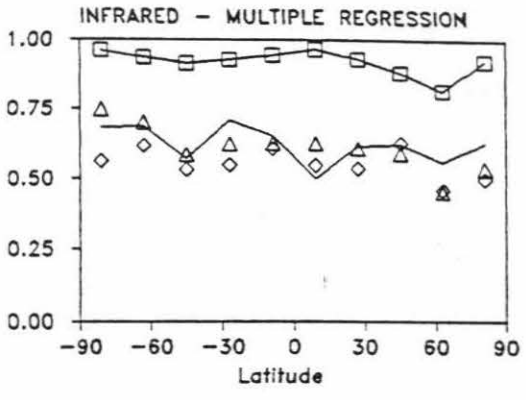

(d.) same as in (c.)

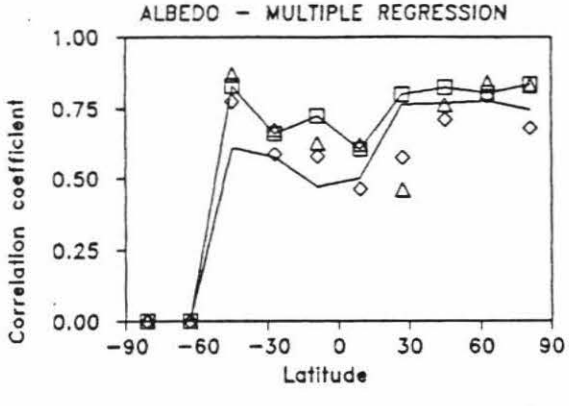

(e.) continents only,
10 CONTINEN grouping

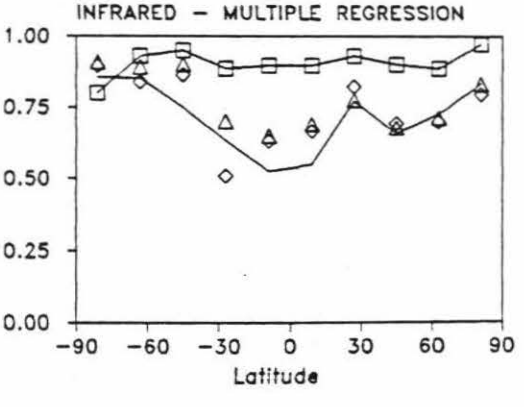

(f.) same as in (e.)

Figure 5.10 (cont.)

Although the flag type regression is generally slightly better than the regression using physical cloud diagnostic variables, it is not demonstrably better than the mindless weather parameter regression. The only region in which the flag regression did significantly better than the mindless regression is over continents between 18° N and 36° N, a region which has very little cloudiness (an inspection of Tiros-N photomosaics shows significant cloudiness only over India and Southeast Asia associated with the summer monsoon). However, the flag regression does not do demonstrably worse than the mindless regression. Clearly, this regression contains significant information. Perhaps, better choices for the turning points and curvatures of the flag functions, or use of better data for their calculation might improve the correlation of flag type diagnostic variables.

The general superiority of regressions using various sorts of FGGE derived data in continental and mid latitude regions over oceanic and low latitude regions may be due to the increased amount of real data available from over the continents in mid latitudes. Those grid points lacking good conventional data in the FGGE analysis used satellite derived data and interpolations and extrapolations. This could introduce errors leading to poor correlation with observed planetary albedo and emerging infrared flux. The superiority of the regressions using the fractional cloudinesses as independent variables for predicting

infrared flux over predicting planetary albedo could be due to the fact that the fractional cloudinesses used in this regression were derived from measurements by THIR, an infrared scanner instrument having no visible channel.

(b.) A short comparison with some work by Linder, et al. (1981)

In order to see how well my multi-parameter regressions of outgoing flux compared with previous measurements by others, I made calculations of the covariance matrix and average vector for the land areas in the region of North America between the latitudes of 27° N and 54° N (i.e., the United States and its immediate surroundings). This was compared with a regression derived by Linder et al. (1981). Linder et al. used scanning radiometer (SR) data from NOAA polar orbiting satellites along with the short range weather prediction output of the National Meteorological Center Limited Fine Mesh (LFM 1) model from the summer of 1976 for the United States.

Linder et al. analyzed their data at a horizontal scale of roughly 190 km. They derived the following diagnostic equation for the planetary albedo over North America:

$$\alpha = .3967 + 8.367 \cdot 10^{-3} r_{mod} - 4.45 \cdot 10^{-4} z_{850} + 8.8 \cdot 10^{-5} \zeta_{500} + 1.198 \cdot 10^{-3} v_{200},$$

where r_{mod} is the modified mean (from 1000 mb to 500 mb) relative humidity (in %, where values $\leq$ 55% are set to 55%), z_{850} is the 850 mb height (m), ζ_{500} is the relative

vorticity at 500 mb (s^{-1}), and v_{200} is the meridional wind at 200 mb ($m\ s^{-1}$). The reduction of variance provided by this regression is 0.487 (corresponding to a multiple correlation coefficient of 0.698).

I have two regressions for the summertime planetary albedo over North America. The first is the mindless regression:

$$\alpha = 6.5 - 9.94\cdot10^{-6}\ z_{500} + 7.51\cdot10^{-4}\ T_{500} - 4.9\cdot10^{-3}\ T_{1000} - 4.93\cdot10^{-3}\ p_s + 2.76\cdot10^{-3}\ r_s - 3.21\cdot10^{-3}\ u_{500} + 1.04\cdot10^{-3}\ v_{500} - 0.406\ \alpha_s + 4.67\cdot10^{-5}\ z_s,$$

which has a multiple correlation coefficient of 0.803 (a reduction of variance by 0.645). The second regression utilizes my flag type variables:

$$\alpha = 0.944 - 2.32\cdot10^{-3}\ T_s + 0.189\ n_{cld} + 0.192\ f(\delta_H)\cdot g(\omega) - 0.0855\ \alpha_s,$$

and has a multiple correlation coefficient of 0.854 (which corresponds to a reduction of the variance by 0.729).

Because they use very different independent variables, a comparison of the regression coefficients between my regressions and that of Linder et al. is difficult and of dubious value. However, it is interesting to note that the regression coefficients for the near surface humidity terms in my "mindless" regression and that of Linder et al. are within a factor of 3 of each other and that the coefficients for the upper air meridional velocity terms differ by only 16%. More important, is the contrast in the ability to

explain the variance in the planetary albedo. My regressions (especially the "flag" regression) explain a noticeably larger fraction of the variance. There are several possibile reasons. One reason is that I have used better visible radiances (broader spectral coverage and a greater range of viewing geometries). Another possibility is that I have treated the radiance data in a more sophisticated fashion as befits the better data. The third possible reason is that the FGGE data are far superior to the 1976 LFM 1 data. The FGGE data consisted of analyses updated every 6 hours and were acquired during a period of the most intense atmospheric observation in human history. The LFM 1 data were short range predictions. Thus they were made up entirely of extrapolations from observational data (acquired during a normal period of atmospheric observation), while the FGGE data were dominated by actual observations (especially in such a well observed region as the continental United States). Another fact of note is that the correlation coefficients for the regressions I made for the United States were quite a bit larger than those for regressions of most other parts of the world. I believe that this is due to the higher quality of the FGGE data in this area.

Chapter 6

CONCLUSIONS

What did this thesis accomplish? First, I have shown that it is possible to take the statistics of angularly resolved radiances and determine the relationships between diurnally averaged reflected shortwave flux and emitted longwave flux (above the atmosphere) and various other parameters (including cloud cover). The techniques I used have been shown to be robust against changes in various specifics of the analysis. Second, it has been shown that, although variation in the total cloudiness across the entire Earth may have no great net effect on the net flux absorbed by the Earth, the variation of cloud cover is important on seasonal and regional scales. Moreover, there is evidence for the relationship between clouds and radiation leading to both positive and negative feedback loops that may have a noticable effect on the Earth's climate. Third, the data sets I used have been shown to be usable for deriving empirical diagnostic equations for the emitted longwave flux and the planetary albedo in terms of simple predictable parameters (such as surface air temperature). However, linear equations of this sort may well depend on time of year and region of the globe and may be a poor representation of the atmosphere. Fourth, it is clear that, given meteorological data of high quality, it is possible to explain a large fraction of the variance in the planetary

albedo and emitted longwave flux. The relationships that do so can be used to indicate the ability of certain variables to parameterize various quantities related to cloudiness and/or atmospheric radiation. Such relationships can also serve to fine tune general circulation models of the atmosphere, since the statistics they express represent the real world and the internal statistics of any realistic GCM should match them.

VI.A) The implications of these results for the Earth's climate

The influence of clouds on the Earth's radiation budget is quite complicated. It depends on fractional areal coverage of the clouds, cloud height, cloud thickness, distribution of clouds over the diurnal and seasonal cycles, geographic (especially latitudinal) distribution of clouds, and albedo and temperature of the underlying surface. Since all these are determined by any number of features of the atmospheric dynamics, it would be fortuitous indeed if there were a permanent answer to the question of whether clouds cool the planet (by their effect on the albedo) more or less than they warm the planet (by their greenhouse effect). Probably, the best we can hope for is to elucidate under which conditions clouds have what effect and to determine how these cloud - radiation effects change other characteristics of the atmosphere and surface.

How do my results for the cloud - radiation relationship compare with the results of others? Cess (1976), using zonal mean data from both hemispheres, estimated a near zero net effect of clouds on the net radiation across the globe. Ohring and Clapp (1980) and Ohring et al. (1981), using monthly mean radiation data at a resolution of 2.5° latitude by 2.5° longitude (including the radiation data from NOAA satellites Scanning Radiometers) found, for all the regions investigated, a consistent and significant preponderance of the albedo effect over the greenhouse (corresponding to a net effect of -65 W m^{-2}/unit averaged over the globe). Hartmann and Short (1980) found, using day to day variation of NOAA Scanning Radiometer data, a global effect of between about - 35 W m^{-2}/unit and - 100 W m^{-2}/unit. As pointed out by Hartmann and Short, Cess did not really derive a partial derivative of net flux with respect to cloud cover, since he combined data from many different cloud regimes (including varying cloud top height, thickness, patchiness, etc.) without accounting for these variations in the statistical analysis. On the other hand, both Ohring and Clapp (1980) and Hartmann and Short (1980) utilized data from small geographic regions, using temporal variation in cloud cover to determine the statistics of cloudiness and radiation. My analysis, which agreed more closely with the results of Cess (1976) in terms of a global average, involved combining data from different longitudes in zones 9° wide (in latitude), or combining data from larger parts of the globe but taking

into account, in a statistical sense, the variation of cloudiness, flux, and the other variables with latitude. Although, the hope was that important cloud parameters (other than areal coverage) would be constant in narrow zones, this may not be strictly true. Therefore, my estimate of the global effect of clouds on net flux may be more akin to a total derivative than the estimates of Ohring and Clapp or Hartmann and Short. There are potentially other reasons, however, for the difference. First of all, both of the other studies, did not explicitly use measurements of areal cloud coverage. Rather, they assumed a linear relationship between cloud amount and planetary albedo to utilize the relationship between visible radiances and infrared radiances (along with a priori assumptions about the albedoes of clouds and their underlying surfaces or about the variation of infrared flux with cloudiness) as a proxy for the relationship between either of the two and areal cloud coverage. Another possibility is that THIR was unable to distinguish between low clouds and clear skies often enough, that the relationship between low cloud cover and the net flux was substantially lost. This would be a major disappointment, since it is these clouds (especially the marine stratocumulus seen off the western coasts of continents in the low mid-latitudes; check the maps in Hartmann and Short, 1980 and in Ohring et al., 1981) that have the most albedo dominated relationship between areal coverage and net flux.

ERB data and correlative cloudiness and meteorological data sets can be used with the techniques of this study to determine empirically what sort of cloud - radiation feedback loops exist in the atmosphere. The example of the positive feedback loop involving tropical cloudiness, radiation, and surface temperature is encouraging. Just this sort of cloud - radiation interaction has been predicted by Liou and Zheng (1984) to maintain an intense Hadley circulation in the tropics.

I have demonstrated the possibility of determining empirical relationships between simple climate parameters such as surface temperature and top-of-the-atmosphere radiative flux, using the Nimbus 7 ERB radiances and the FGGE Level IIIb data set and my own techniques of analysis. However, it is worth remembering that there may be no such parameterization that is good for predicting the net flux over a broad enough range of the climate parameters to be useful in answering such questions as the effects of major decreases in the solar flux, or how ice-albedo feedback worked in the presence of clouds in the Pleistocene. As argued by Stephens and Webster (1981), simple energy balance climate models are useless without an understanding of how cloudiness relates to surface temperature, and (so they claim) a usable relationship of that sort probably does not exist. Certainly, the visual relation between three day zonal averages of emitted infrared flux and surface

temperature (Figure 5.8) does not inspire confidence in the veracity of single valued linear functions.

It can be argued, however, that such simple climate models, although not providing the best simulation of the Earth's climate system, can provide insight into the important physical processes involved in the climate. For this reason, it is still worthwhile determining more realistic parameterizations, based on the best data, analyzed in the most careful way. There are arguments for using data of the sort I have used here for such parameterizations (see Chapter 5).

It is especially encouraging that using relatively easily determined meteorological variables, it is possible to explain a large portion of the variance of the planetary albedo. Although this was not possible in all the regions investigated, it worked best in just those areas with the best meteorological data. This lends hope to the belief that the sort of statistical relations between top-of-the-atmosphere radiation and the state of the weather, investigated in this thesis, can be used in fine tuning general circulation models of the Earth's atmosphere.

VI.B) Future directions in this research

A number of problems and opportunities were exposed in this study that suggest future possibilities for research. One problem is that, due to the long time scale for changes in radiation, the accuracy of my results is not as high as

the number of measurements might suggest. Clearly, data should be analyzed from a wider span of time than just one week. Furthermore, it would be nice to investigate further the seasonal variation in such things as cloud - radiation interactions. Given enough data, it would not be necessary to combine data from different locations (even if only different longitudes in the same zone) in order to build up the accuracy of the statistics under investigation. By using data from only one small region at a time, it should be possible to have a better idea of what is producing the variations in cloudiness, radiative flux, and other variables. Furthermore, it would then be possible to map various statistical parameters and see how they relate to the atmospheric and surface characteristics of the planet.

The quality of the areal fractional cloud cover estimates derived from THIR is not as high as it could have been if THIR had had a visible channel. It might be possible to use cloudiness data sets from the same time frame as the Nimbus 7 ERB data from different satellites. In this case, the time of retrieval of the data might vary from that of the ERB data by up to 6 hours (although, since most NOAA satellites are put in 0900 - 2100 or 0300 - 1500 orbits, hopefully the time differential would be much less). One example of such a data set is that developed by Chahine et al. (1983) and Susskind et al. (1983), using the HIRS2 and MSU instruments on the Tiros N/NOAA 6 - 9 satellite series. The data retrieved include temperature profiles,

humidity profiles, surface temperature, snow and ice cover, sea surface winds, cloud amount, and cloud top height and temperature. In addition to helping to solve the problems in the lack of accurate cloud amounts, these data might be useful in lieu of FGGE data in regions of sparse conventional data coverage.

Another possibility for improving the data used in this sort of analysis, is to stick to the FGGE Level IIb data set. This is the actual data taken by the vast variety of platforms deployed during FGGE. It hasn't been interpolated, extrapolated, or averaged. Although such data would probably leave holes in the coverage of the globe, by using a large enough data set (presumably the entire FGGE year) and appropriate weighting, such problems could be overcome. Another data set that might be useful is that taken by the Nimbus 7 SMMR (Scanning Multichannel Microwave Radiometer). This instrument collected data on column water vapor abundance, column liquid water abundance (in clouds), sea surface temperature, sea surface wind speed, and sea ice coverage (see Gloersen et al., 1984). Furthermore, being on the same platform as ERB (just as THIR is) there should be no problem in the time delay between SMMR and ERB data.

Another way of improving the analysis would be to use the less massaged ERB data, in the form of the Master Archival Tapes. These data have not been divided up into various angular bins and sub-fields of view, the way the data on the STRTs were. Although the STRTs were remarkably

easy to use, their structure really was designed in order to carry out studies of the angular distribution models of various reflecting and emitting surface-atmosphere ensembles.

In terms of opportunities, it is clear that the use of ERB scanner data in conjunction with high quality meteorological and cloudiness data has potential in elucidating many complicated interactions between clouds, radiation, and dynamics. Moreover, the same data can certainly be used for GCM tuning.

References

A. Arakawa and W. H. Schubert, J. Atmos. Sci. 31, 674 - 701 (1974).

A. Arking and S. Vemury, J. Geophys. Res. 89, 5089 - 5097 (1984).

L. Bengtsson, M. Kanamitsu, P. Kallberg, and S. Uppala, Bull. Amer. Meteorol. Soc. 63, 29 - 43 (1982a).

L. Bengtsson, M. Kanamitsu, P. Kallberg, and S. Uppala, Bull. Amer. Meteorol. Soc. 63, 277 - 305 (1982b).

P. R. Bevington, Data Reduction and Error Analysis for the Physical Sciences, McGraw - Hill Book Co., New York, NY, 336 p. (1969).

B. Brennan and W. R. Bandeen, Applied Optics 9, 405 - 412 (1970).

M. I. Budyko, Tellus 21, 611 - 619 (1969).

M. I. Budyko, Meteorol. Hydrol. 10, 1 - 10 (1975).

J. J. Carroll and B. W. Fitch, J. Geophys. Res. 86, 5271 - 5276 (1981).

R. D. Cess, J. Atmos. Sci. 33, 1831 - 1843 (1976).

M. T. Chahine, R. Haskins, J. Susskind, and D. Reuter, Preprints - Fifth Conference on Atmospheric Radiation, 10 - 16 (1983).

T. S. Chen and G. Ohring, Preprints - Fifth Conference on Atmospheric Radiation, 284 - 286 (1983).

T. S. Chen, L. L. Stowe, V. R. Taylor, and P. F. Clapp, IRS 1980 International Radiation Symposium - Volume of Extended Abstracts, Colorado State University, Fort Collins, Colo., 315 - 317 (1980).

G. T. Cherrix, The Nimbus - 7 User's Guide, NASA Goddard Space Flight Center, Greenbelt, Md., 247 - 263 (1978).

H. L. Crutcher and J. M. Meserve, Selected Level Heights, Temperatures, and Dewpoints for the Northern Hemisphere, NAVAIR, 50-1C-52 (1970).

J. M. Davis and S. K. Cox, Atmospheric Science Paper No. 338, Colorado State University, Fort Collins, Colo., 125 p. (1981).

P. Gloersen, et al., J. Geophys. Res. 89, 5335 - 5344 (1984).

J. Hansen, G. Russell, D. Rind, P. Stone, A. Lacis, L. Travis, S. Lebedeff, and R. Ruedy, "An efficient three dimensional global model for climate studies: I. Model I", preprint, 1980

Harshvardhan, J. Atmos. Sci. 39, 1853 - 1861 (1982).

D. L. Hartmann and D. A. Short, J. Atmos. Sci. 37, 1233 - 1250 (1980).

J. R. Holton, An Introduction to Dynamic Meteorology, Academic Press, New York, 319 p. (1972).

S. B. Idso, D. G. Baker, and B. L. Blad, Quart. J. Roy. Met. Soc. 95, 244 - 257 (1969).

H. Jacobowitz, L. L. Stowe, and J. R. Hickey, The Nimbus - 7 User's Guide, NASA Goddard Space Flight Center, Greenbelt, Md., 33 - 69 (1978).

H. Jacobowitz, R. J. Tighe, and the Nimbus 7 ERB Experiment Team, J. Geophys. Res. 89, 4997 - 5010 (1984a).

H. Jacobowitz, H. V. Soule, H. L. Kyle, F. B. House, and the Nimbus 7 ERB Experiment Team, J. Geophys. Res. 89, 5021 - 5038 (1984b).

P. E. James, A Geography of Man, Ginn and Co., New York, NY, 631 p. (1951).

R. L. Jenne, H. L. Crutcher, H. Van Loon, and J. J. Taljard, A Selected Climatology of the Southern Hemisphere: Computer Methods and Data Availability, NCAR-TN/STR-92, Boulder, Colo., 91 p. (1974).

J. S. Jensenius, J. J. Cahir, and H. A. Panofsky, Quart. J. Roy. Met. Soc. 104, 119 - 130 (1978).

K. Ya. Kondrat'ev (ed.), Radiation Characteristics of the Atmosphere and the Earth's Surface (English translation), Amerind Publishing Co. Pvt. Ltd., New Delhi, India, 580 p. (1973).

K. Th. Kriebel, Beitrage zur Physik der Atmosphare 47, 14 - 44 (1974).

D. I. Linder, R. J. Stouffer, J. J. Cahir, and H. A. Panofsky, Quart. J. Roy. Met. Soc. 107, 243 - 258 (1981).

B. W. Lindgren, G. W. McElrath, and D. A. Berry, Introduction to Probability and Statistics, Macmillan Publishing Co., New York, NY, 356 p. (1978).

R. S. Lindzen, Clouds in Climate: Modeling and Satellite Observational Studies, NASA Goddard Institute of Space Studies, New York, NY, 42 - 51 (1981).

K. - N. Liou and Q. Zheng, J. Atmos. Sci. 41, 1513 - 1535 (1984).

K. - N. Liou and R. J. Curran, Bull. Amer. Meteorol. Soc. 65, 475 - 483, (1984).

A. Lorenc, Mon. Weather Rev. 109, 701 - 721 (1981).

J. L. Monteith and G. Szeicz, Quart. J. Roy. Met. Soc. 87, 159 - 170 (1961).

C. J. Moore, Quart. J. Roy. Met. Soc. 102, 889 - 899 (1976).

E. I. Mukammal, Arch. Met. Geoph. Biokl., Ser. B 19, 29 - 52 (1971).

L. C. Nkemdirim, Arch. Met. Geoph. Biokl., Ser. B 20, 23 - 40 (1972).

J. Oerlemans and H. M. Van den Dool, J. Atmos. Sci. 35, 371 - 381 (1978).

G. Ohring and P. Clapp, J. Atmos. Sci. 37, 447 - 454 (1980).

G. Ohring and A. Gruber, Advances in Geophysics 25, 237 - 304 (1983).

G. Ohring, P. F. Clapp, T. R. Heddinghaus, and A. F. Krueger, J. Atmos. Sci. 38, 2539 - 2541 (1981).

J. Otterman and R. S. Fraser, Remote Sensing of Environment 5, 247 - 266 (1976).

R. T. Pinker, O. E. Thompson, and T. F. Eck, Quart. J. Roy. Met. Soc. 106, 551 - 558 (1980).

E. Sarachik, Clouds in Climate: Modeling and Satellite Observational Studies, NASA Goddard Institute of Space Studies, New York, NY, 8 - 27 (1981).

I. Simmonds and C. Chidzey, J. Atmos. Sci. 39, 2144 - 2151 (1982).

J. J. Simpson and C. A. Paulson, Quart. J. Roy. Met. Soc. 105, 487 - 502 (1979).

R. C. J. Somerville and L. A. Remer, J. Geophys. Res. 89, 9668 - 9672 (1984).

G. L. Stephens and P. J. Webster, J. Atmos. Sci. 38, 235 - 247 (1981).

L. L. Stowe, M. Chen, H. Jacobowitz, and I. Ruff, Preprints - Third Conference on Atmospheric Radiation, 103 - 106 (1978).

L. L. Stowe, et al., IRS 1980 International Radiation Symposium - Volume of Extended Abstracts, Colorado State University, Fort Collins, Colo., 413 - 415 (1980).

J. Susskind, D. Reuter, and M. T. Chahine, Preprints - Fifth Conference on Atmospheric Radiation, 23 - 26 (1983).

V. R. Taylor and L. L. Stowe, J. Geophys. Res. 89, 4987 - 4996 (1984).

S. K. Vemury, L. Stowe, and H. Jacobowitz, J. Geophys. Res. 89, 5345 - 5353 (1984).

S. G. Warren and S. H. Schneider, J. Atmos. Sci. 36, 1377 - 1391 (1979)

P. J. Webster and G. L. Stephens, The Global Climate (ed. J. T. Houghton), Chapter 5, Cambridge University Press, (1984).

J. S. Winston, et al., Earth - Atmosphere Radiation Budget Analyses Derived from NOAA Satellite Data, June 1974 - Feb. 1978, U. S. Dept. of Commerce, NOAA, NESS, Washington, DC, (1979).

Appendix A

BRIEF DESCRIPTION OF THE DATA SETS USED TO DETERMINE SURFACE ALBEDOES

A.1) Quality of the data sets in each of the twelve surface categories

GEOGRAPHY categories from GEOGRAPHY files

LAND	see Vegetation categories
WATER	1 great, 3 good
SNOW	1 good, 1 fair
ICE	1 poor

VEGETATION categories from TOPOGRAPHY files

MOUNTAIN	1 fair, 2 poor
SELVA	1 good
TIAGA	2 good, 1 fair
SCRUB	1 poor
MIXED	1 good, 1 poor
SAVANNAH	1 good
PRAIRIE	1 good, 3 fair, 2 poor
TUNDRA	1 poor
DESERT	1 good, 2 poor

A.2) Description of the data sets

For those data sets with many measurements of albedo at different solar zenith angles, I list the angles on the first line and the albedoes on the next line. All angles are in degrees and all albedoes are in percent.

Mountains Davis and Cox (1981)
Himalayas
measured by bugeye from airplane
15.0 25.0
22.0 26.0

Mountains Brennan and Bandeen (1970)
De Soto National Forest
solar zenith angles of 51.6 - 68.6
albedo of around 18%

Forest (Mountains?) Moore (1976)
Mt.Gambier, South Australia - 10 yr. old forest
measured by radiometers from 2m above tallest trees

18.0	25.2	35.3	47.5	59.0	71.0	82.6
10.5	10.8	12.1	12.4	13.2	13.9	13.1

Selva Pinker, et al. (1980)
Thai rain forest
measured by Eppley pyranometers from height of 16m above forest canopy

10.0	20.0	30.0	40.0	50.0	60.0	70.0	80.0
11.1	11.3	11.8	12.4	13.6	14.9	16.5	18.7

Taiga Mukammal (1971)
pine forest in Ontario in September
measured by Eppley pyrheliometers and CSIRO pyrradiometers from 18m above canopy, 36m above ground

41.7	42.4	45.0	46.8	51.4	54.1	59.9	63.0	69.6
10.1	10.1	10.5	10.8	11.3	12.1	12.5	14.1	14.0
	72.9							
	17.6							

Taiga Mukammal (1971)
spruce forest in Ontario in September
measured by Eppley pyrheliometers and CSIRO pyrradiometers from 36m? above ground

47.5	48.1	50.5	52.2	56.5	59.0	64.6	67.5	73.9
14.0	14.0	14.4	14.5	15.8	15.8	18.4	17.8	22.0
	77.2	87.4						
	21.5	26.6						

Taiga Kondrat'ev (1973)
measurements of leafy, coniferous forests in USSR and around the world
Kondrat'ev uses monthly average albedo of 14% for the months of May through September

June	solar zenith angles of 35 - 51 albedoes of 14% - 17%
August	solar zenith angles of 49 - 60 albedoes of 12% - 16%
September	solar zenith angles of 52 - 64 albedoes of 19% - 20%

Scrub Otterman and Fraser (1976)
measured from Landsat
overgrazed region of Sahel in winter had albedo of 34%, should use this for Scrub albedo (but adjust it down somehow for not being bugeye measurement and being measured at max solar zenith angle)

Mixed Land Area Davis and Cox (1981)
India
measured by bugeye from aircraft

5.0	15.0	25.0	35.0
15.0	13.0	13.0	12.0

Mixed Land Area Kondrat'ev (1973)
large regions of European USSR with seasonal snowcover
monthly average albedoes for the months May through October are all 18%

Savannah Kriebel (1974)
Namibian savannah
measured by bugeye from airplane

10.0	20.0	30.0	40.0	50.0	60.0	70.0	80.0
17.0	16.8	16.4	16.0	15.6	15.7	16.0	17.8

Prairie Monteith and Szeicz (1961)
Hertfordshire, UK
measured by radiometer at height of 1.5m
short grass solar zenith angles 31 to 71
albedoes of 25% or 27%
long grass solar zenith angles 42 to 71
albedo of 26%

Prairie Idso, et al. (1969)
University of Minnesota
measured by Eppley pyranometer at 0.75m above ground
short grass sod on clear day
diurnal mean albedo 26% - 27%
bare soil on clear day
diurnal mean albedo 28% - 29%

Prairie Nkemdirim (1972)
Calgary, Alberta
measured by pyranometer from 0.45m above ground
prairie grass (cut to 5cm height) in the summer
diurnal mean albedoes of 21% - 23%

Prairie Moore (1976)
near Mt. Gambier, S. Australia
measured by radiometers at 2m height in the summer
grazed pasture of rye grass and 2 kinds of clover
mean summer albedo = 24%

15.1	24.8	35.2	47.2	59.0	70.7	83.5
22.8	23.7	24.4	25.6	28.3	29.5	34.3

Crops — Monteith and Szeicz (1961)
Hertfordshire, UK
measured at height of 1.5m
bare soil solar zenith angles 31 to 71
albedo of 17%
kale solar zenith angles 31 to 71
albedo of 19% or 28% or 25%

Crops — Idso, et al. (1969)
southwest US
measurements on irrigated fields
daily mean albedoes of

alfalfa	24%
barley	23%
wheat	21%
oats	23%
cotton	22%
sorghum	21%
all crops	22%

Tundra — Kondrat'ev (1973)
Soviet Union
measured from airplane
solar zenith angles of roughly 54.0 - 66.0
albedoes of 11% - 23%; should use about 18%

Desert — Davis and Cox (1981)
Saudi Arabia Empty Quarter - sand
measured by bugeye from airplane

5.0	15.0	25.0	35.0	45.0	55.0	65.0	75.0
26.0	26.0	24.0	26.0	27.0	30.0	30.0	34.0

Desert — Kondrat'ev (1973)
Soviet Union
measured from airplane
yellow-gray sand (August) solar zenith angle about 34
albedo = 25%
light yellow sand (August) solar zenith angle about 40
albedo = 37%
gray sand (September) solar zenith angle about 45 - 54
albedo = 20% - 28%
monthly average albedoes for May thru November = 28%

Desert — Otterman and Fraser (1976)
Sinai (several times of year), Thar desert,
N.W. Mexico, Sahel, Afghanistan,
W. coast of Africa
measured from Landsat
albedoes of 34% - 52% including regions of scrub

Water Davis and Cox (1981)

Indian Ocean
measured by bugeye from airplane

5.0	15.0	25.0	35.0	45.0	55.0
4.0	4.0	6.0	5.0	6.0	10.0

Water Simpson and Paulson (1979)

Pacific Ocean
measured by pyranometer from height of 11m

48.0	50.0	52.0	54.0	56.0	58.0	60.0	62.0	64.0
6.0	5.5	6.1	6.4	6.7	7.3	8.0	8.5	9.2

66.0	68.0	70.0	72.0	74.0	76.0	78.0	80.0
10.4	11.6	13.6	14.8	18.8	16.0	26.0	30.0

82.0	84.0	86.0
33.2	19.7	26.3

Water Kondrat'ev (1973)

Black Sea - deep water

30.0	40.0	50.0	60.0	70.0	80.0
4.0	5.0	6.0	10.0	12.0	36.0

Water Kondrat'ev (1973)

Norwegian Sea - moderately windy and turbulent surface

50.0	60.0	70.0	75.0
4.0	7.0	11.0	18.0

Snow Carroll and Fitch (1981)

South Pole
measured by Eppley pyranometers at 1m height
for cloud cover <25%

67.6	71.9	75.9	79.8	84.6
82.9	84.2	89.6	88.6	93.5

Snow Kondrat'ev (1973)

near Moscow, Soviet Union
in regions of fields and forests

snow condition	field	forest
freshly fallen, dry or wet	82%	82%
fine-grained, wet	73%	65%
mid-grained, wet	64%	56%
large-grained, wet	55%	47%
mottled region	47%	39%
distinct spots of snow	36%	31%

Ice — Kondrat'ev (1973)

Arctic Region (of USSR?)

Surface Type	Surface Color	Albedo Mean	Albedo Max.	Albedo Min.
ice floe w/out snow	green, dry	45%	50%	40%
melting ice floe	gray, moist	50%	55%	45%
melting packed type ice w/out snow	gray, moist (knobby)	56%	67%	49%
frozen snowflakes (naslud, fresh pool ice)	gray	44%	50%	42%

Appendix B

A STATISTICAL COMPARISON OF THE RESULTS DERIVED FROM ANALYSES USING DIFFERENT PATTERNS OF ANGULAR BINS FOR THE VISIBLE RADIANCES

In this appendix I compare statistical results from four analyses of the ERB data. The statistical results I investigate include the averages of the visible flux, the covariances of this variable with the other variables I investigated, and the correlation coefficients of the visible flux with the other variables. The tables are described individually. The first two tables compare the results obtained by using the 49 angular bin pattern with those obtained using the 32 angular bin pattern (see Figures 3.3a and 3.3c). This comparison indicates the importance (or lack of it) of the choice of the original angular bin pattern for analysis of the visible radiance data. The last two tables compare the results obtained by using the 49 angular bin pattern with those obtained using the same data, but collapsed into the 19 angular bin pattern of Figure 3.3b. This comparison is indicative of the importance of the exact pattern used to collapse the covariance matrices in such a way as to have no zero elements in the population matrix.

TABLE B.1

In this table, I compare the results of the 49BIN CON and 32BIN JUN analyses to determine the effect of using different patterns of angular bins in analyzing the visible data. I looked at average visible flux and the covariances and correlation coefficients of visible flux with non-radiative variables for the 8 LATITUDES geographic grouping. I took the ratios of the 32BIN JUN results to the 49BIN CON results and utilized these ratios in determining average, minimum, and maximum ratios, and standard deviations of the ratios, for each latitude band. At the beginning of each latitude band, I present the number of 49BIN CON correlation coefficients (out of 40) that were greater than or equal to 0.15, since only these cases were investigated for the ratios of the covariances and correlation coefficients.

LATITUDE # 1	NUMBER OF CCS. 0		
	AVERAGE		
AVERAGE RATIO	1.000		
RATIO STD DEV	0.000E+00		
MINIMUM RATIO	1.000E+00		
MAXIMUM RATIO	1.000E+00		

LATITUDE # 2	NUMBER OF CCS. 32		
	AVERAGE	COVARIANCE	CORR COEF
AVERAGE RATIO	0.994	1.014	0.981
RATIO STD DEV	0.000E+00	5.189E-02	5.024E-02
MINIMUM RATIO	9.938E-01	8.870E-01	8.588E-01
MAXIMUM RATIO	9.938E-01	1.131E+00	1.095E+00

LATITUDE # 3	NUMBER OF CCS. 27		
	AVERAGE	COVARIANCE	CORR COEF
AVERAGE RATIO	0.991	0.961	0.947
RATIO STD DEV	0.000E+00	4.528E-02	4.461E-02
MINIMUM RATIO	9.907E-01	8.799E-01	8.667E-01
MAXIMUM RATIO	9.907E-01	1.032E+00	1.017E+00

LATITUDE # 4	NUMBER OF CCS. 27		
	AVERAGE	COVARIANCE	CORR COEF
AVERAGE RATIO	0.998	0.994	0.994
RATIO STD DEV	0.000E+00	2.132E-02	2.134E-02
MINIMUM RATIO	9.977E-01	9.399E-01	9.406E-01
MAXIMUM RATIO	9.977E-01	1.015E+00	1.016E+00

LATITUDE # 5	NUMBER OF CCS. 25		
	AVERAGE	COVARIANCE	CORR COEF
AVERAGE RATIO	0.997	0.999	0.965
RATIO STD DEV	0.000E+00	2.192E-02	2.117E-02
MINIMUM RATIO	9.972E-01	9.636E-01	9.310E-01
MAXIMUM RATIO	9.972E-01	1.059E+00	1.023E+00

LATITUDE # 6	NUMBER OF CCS. 34		
	AVERAGE	COVARIANCE	CORR COEF
AVERAGE RATIO	1.005	1.021	0.993
RATIO STD DEV	0.000E+00	2.883E-02	2.807E-02
MINIMUM RATIO	1.005E+00	9.816E-01	9.555E-01
MAXIMUM RATIO	1.005E+00	1.099E+00	1.070E+00

LATITUDE # 7	NUMBER OF CCS. 33		
	AVERAGE	COVARIANCE	CORR COEF
AVERAGE RATIO	1.006	1.043	0.994
RATIO STD DEV	0.000E+00	2.402E-02	2.290E-02
MINIMUM RATIO	1.006E+00	9.908E-01	9.445E-01
MAXIMUM RATIO	1.006E+00	1.098E+00	1.047E+00

LATITUDE # 8	NUMBER OF CCS. 37		
	AVERAGE	COVARIANCE	CORR COEF
AVERAGE RATIO	0.997	0.915	0.943
RATIO STD DEV	0.000E+00	6.834E-02	7.044E-02
MINIMUM RATIO	9.972E-01	7.164E-01	7.384E-01
MAXIMUM RATIO	9.972E-01	1.089E+00	1.122E+00

TABLE B.2

In this table (as in table B.1), I compare the results of the 49BIN CON and 32BIN JUN analyses to determine the effect of using different patterns of angular bins in analyzing the visible data. I looked at average visible flux and the covariances and correlation coefficients of visible flux with all variables for each of the geographic groupings. I took the ratios of the 32BIN JUN results to the 49BIN CON results and utilized these ratios in determining average, minimum, and maximum ratios, and standard deviations of the ratios, for the average visible flux and each of the visible flux covariances and correlation coefficients. At the beginning of the table, I tabulate the results for the average flux ratios. Then for each variable (with which visible flux was correlated) the covariance results are tabulated followed by the number of 49BIN CON correlation coefficients (out of 20) that were greater than or equal to 0.15 (since, as in the last table, only these cases were investigated for the ratios of the covariances and correlation coefficients) followed by the ratio results for the correlation coefficients.

	20
AVERAGE	0.9926
STAND DEV	0.0333
MINIMUM	0.8502
MAXIMUM	1.0139

	AVG MUSUN	FLUX UP V	FLUX UP I	F CL TOTL	F CL LOW
AVERAGE	0.9844	1.0277	0.9989	0.9871	0.9984
STAND DEV	0.0688	0.0825	0.0368	0.0307	0.0549
MINIMUM	0.8390	0.7476	0.8673	0.9146	0.8614
MAXIMUM	1.0536	1.1261	1.0466	1.0264	1.0840
	14	19	18	18	15
AVERAGE	0.9792	1.0000	0.9858	0.9670	0.9885
STAND DEV	0.0440	0.0000	0.0155	0.0281	0.0341
MINIMUM	0.8647	1.0000	0.9480	0.8969	0.9269
MAXIMUM	1.0199	1.0000	1.0085	1.0142	1.0592

	F CL MID	F CL HIGH	F CL HI I	F CL HI W	FCL**2
AVERAGE	0.9756	0.9984	0.9921	1.0097	0.9873
STAND DEV	0.0806	0.0481	0.0480	0.0407	0.0322
MINIMUM	0.7164	0.8551	0.8562	0.9295	0.9144
MAXIMUM	1.0660	1.0584	1.0541	1.0650	1.0289
	17	17	12	18	18
AVERAGE	0.9660	0.9872	0.9798	0.9891	0.9672
STAND DEV	0.0709	0.0368	0.0231	0.0401	0.0322
MINIMUM	0.7384	0.9168	0.9375	0.9289	0.8852
MAXIMUM	1.0493	1.0909	1.0250	1.0753	1.0315

	FCL*ASURF	FCL*TSURF	FCL*TS**4	FCL*T1000	FCL*TCTOP
AVERAGE	1.0086	0.9891	0.9840	0.9892	0.9886
STAND DEV	0.0356	0.0255	0.0340	0.0258	0.0261
MINIMUM	0.9134	0.9221	0.8744	0.9204	0.9133
MAXIMUM	1.0673	1.0266	1.0270	1.0266	1.0271
	17	18	18	18	18
AVERAGE	0.9864	0.9688	0.9731	0.9690	0.9684
STAND DEV	0.0242	0.0218	0.0227	0.0217	0.0217
MINIMUM	0.9374	0.9308	0.9331	0.9314	0.9387
MAXIMUM	1.0333	1.0138	1.0128	1.0138	1.0143

	FCL*MUSUN	FCL*AS*MU	T SURFACE	TSURF**2	TSURF**3
AVERAGE	0.9859	0.9989	0.9885	0.9885	0.9884
STAND DEV	0.0433	0.0464	0.0691	0.0688	0.0685
MINIMUM	0.8605	0.8607	0.8661	0.8660	0.8659
MAXIMUM	1.0296	1.0449	1.1022	1.1021	1.1020
	19	19	16	16	16
AVERAGE	0.9735	0.9864	0.9783	0.9782	0.9782
STAND DEV	0.0213	0.0251	0.0485	0.0482	0.0478
MINIMUM	0.9310	0.9377	0.8709	0.8717	0.8726
MAXIMUM	1.0102	1.0476	1.0718	1.0717	1.0716

	TSURF**4	Z500	T500	T1000	P SURFACE
AVERAGE	0.9884	1.0058	0.9839	0.9868	0.9888
STAND DEV	0.0682	0.0704	0.0618	0.0688	0.0672
MINIMUM	0.8658	0.8631	0.8592	0.8653	0.8599
MAXIMUM	1.1019	1.1242	1.0593	1.1108	1.0994
	16	14	13	16	16
AVERAGE	0.9781	0.9944	0.9776	0.9767	0.9787
STAND DEV	0.0475	0.0424	0.0359	0.0497	0.0541
MINIMUM	0.8734	0.9231	0.8855	0.8730	0.8588
MAXIMUM	1.0715	1.0681	1.0235	1.0802	1.0702

	SIGMA W V	N CLD LYR	Z CLD TOP	T CLD TOP	DS/DZ
AVERAGE	0.9890	1.0005	1.0055	1.0057	1.0044
STAND DEV	0.0570	0.0592	0.0576	0.0838	0.0580
MINIMUM	0.8239	0.8368	0.8603	0.8151	0.9254
MAXIMUM	1.0471	1.0887	1.0985	1.1795	1.0820
	17	15	14	16	11
AVERAGE	0.9785	0.9899	0.9940	0.9926	0.9886
STAND DEV	0.0383	0.0448	0.0377	0.0639	0.0427
MINIMUM	0.8492	0.9278	0.9346	0.8172	0.9119
MAXIMUM	1.0153	1.1221	1.0471	1.1470	1.0685

	DH*/DZ	DH-AV/DZ	FLAG ST W R	SURFACE	U500
AVERAGE	1.0057	1.0019	1.0121	1.0161	1.0218
STAND DEV	0.0440	0.0569	0.0594	0.0374	0.0434
MINIMUM	0.9018	0.8799	0.9195	0.9431	0.9706
MAXIMUM	1.0575	1.0719	1.1092	1.0914	1.1234
	14	14	14	14	11
AVERAGE	0.9823	0.9801	0.9871	0.9969	1.0058
STAND DEV	0.0316	0.0424	0.0478	0.0369	0.0381
MINIMUM	0.9124	0.8667	0.9057	0.9402	0.9287
MAXIMUM	1.0247	1.0238	1.0664	1.0942	1.0711

	V500	P1 LATITU	P2 LATITU	A SURFACE	ASURF**2
AVERAGE	0.9970	0.9846	0.9841	0.9803	0.9695
STAND DEV	0.0702	0.0692	0.0739	0.1092	0.1012
MINIMUM	0.8649	0.8382	0.8392	0.6857	0.7127
MAXIMUM	1.1310	1.0587	1.0590	1.0952	1.0568
	11	14	13	12	11
AVERAGE	0.9823	0.9793	0.9780	0.9736	0.9650
STAND DEV	0.0525	0.0436	0.0469	0.0924	0.0844
MINIMUM	0.9133	0.8640	0.8649	0.6875	0.7145
MAXIMUM	1.0950	1.0143	1.0227	1.0650	1.0287

	AS*MUSUN Z	SURFACE
AVERAGE	0.9955	0.9648
STAND DEV	0.0607	0.0567
MINIMUM	0.8606	0.8546
MAXIMUM	1.0772	1.0531
	11	12
AVERAGE	0.9909	0.9585
STAND DEV	0.0280	0.0415
MINIMUM	0.9265	0.8808
MAXIMUM	1.0485	1.0090

TABLE B.3

In this table, I compare the results of the 6DAY 49BA and 6DAY 19BA analyses to determine the effect of using different patterns of angular bins in analyzing the visible data. The table is set up the same as Table B.1 and involves the same sort of data from the 8 LATITUDES geographic grouping, analyzed in the same way. I used the ratios of the 6DAY 19BA results to the 6DAY 49BA results in determining these statistics. Unlike the comparison in Table B.1, however, the 19 angular bin pattern was used by averaging the results in the summation matrices for various bins in the 49 angular bin pattern together, and thereby making summation matrices appropriate for the 19 angular bin pattern. The 19 bin summation matrices were not determined (as the 32 bin summation matrices were) completely independently of the 49 bin summation matrices.

LATITUDE # 1	NUMBER OF CCS. 0		
	AVERAGE		
AVERAGE RATIO	1.000		
RATIO STD DEV	0.000E+00		
MINIMUM RATIO	1.000E+00		
MAXIMUM RATIO	1.000E+00		

LATITUDE # 2	NUMBER OF CCS. 28		
	AVERAGE	COVARIANCE	CORR COEF
AVERAGE RATIO	1.045	1.070	0.985
RATIO STD DEV	0.000E+00	1.279E-02	1.178E-02
MINIMUM RATIO	1.045E+00	1.021E+00	9.404E-01
MAXIMUM RATIO	1.045E+00	1.100E+00	1.013E+00

LATITUDE # 3	NUMBER OF CCS. 31		
	AVERAGE	COVARIANCE	CORR COEF
AVERAGE RATIO	1.031	0.995	0.928
RATIO STD DEV	0.000E+00	2.711E-02	2.528E-02
MINIMUM RATIO	1.031E+00	9.331E-01	8.703E-01
MAXIMUM RATIO	1.031E+00	1.051E+00	9.801E-01

LATITUDE # 4	NUMBER OF CCS. 30		
	AVERAGE	COVARIANCE	CORR COEF
AVERAGE RATIO	1.014	0.988	0.953
RATIO STD DEV	0.000E+00	1.532E-02	1.479E-02
MINIMUM RATIO	1.014E+00	9.692E-01	9.349E-01
MAXIMUM RATIO	1.014E+00	1.041E+00	1.004E+00

LATITUDE # 5	NUMBER OF CCS. 25		
	AVERAGE	COVARIANCE	CORR COEF
AVERAGE RATIO	1.008	0.995	0.973
RATIO STD DEV	0.000E+00	1.768E-02	1.730E-02
MINIMUM RATIO	1.008E+00	9.663E-01	9.449E-01
MAXIMUM RATIO	1.008E+00	1.028E+00	1.005E+00

LATITUDE # 6	NUMBER OF CCS. 35		
	AVERAGE	COVARIANCE	CORR COEF
AVERAGE RATIO	1.009	1.008	0.983
RATIO STD DEV	0.000E+00	2.199E-02	2.145E-02
MINIMUM RATIO	1.009E+00	9.695E-01	9.455E-01
MAXIMUM RATIO	1.009E+00	1.065E+00	1.038E+00

LATITUDE # 7	NUMBER OF CCS. 33		
	AVERAGE	COVARIANCE	CORR COEF
AVERAGE RATIO	1.016	1.017	0.957
RATIO STD DEV	0.000E+00	1.529E-02	1.440E-02
MINIMUM RATIO	1.016E+00	9.775E-01	9.200E-01
MAXIMUM RATIO	1.016E+00	1.054E+00	9.916E-01

LATITUDE # 8	NUMBER OF CCS. 37		
	AVERAGE	COVARIANCE	CORR COEF
AVERAGE RATIO	1.020	1.025	0.909
RATIO STD DEV	0.000E+00	2.078E-02	1.843E-02
MINIMUM RATIO	1.020E+00	9.701E-01	8.598E-01
MAXIMUM RATIO	1.020E+00	1.075E+00	9.531E-01

TABLE B.4

In this table (as in table B.3), I compare the results of the 6DAY 49BA and 6DAY 19BA analyses to determine the effect of using different patterns of angular bins in analyzing the visible data. The table is set up the same as Table B.2 and involves the same sort of data (from the 8 LATITUDES, CONTINENTAL, OCEANIC, and HEMISPHERIC geographic groupings) analyzed in the same way. I used the ratios of the 6DAY 19BA results to the 6DAY 49BA results in determining these statistics. Unlike the comparison in Table B.2, however, the 19 angular bin pattern was used by averaging the results in the summation matrices for various bins in the 49 angular bin pattern together, and thereby making summation matrices appropriate for the 19 angular bin pattern. The 19 bin summation matrices were not determined (as the 32 bin summation matrices were) completely independently of the 49 bin summation matrices.

	20
AVERAGE	1.0166
STAND DEV	0.0138
MINIMUM	0.9890
MAXIMUM	1.0480

	AVG MUSUN	FLUX UP V	FLUX UP I	F CL TOTL	F CL LOW
AVERAGE	1.0169	1.1033	1.0184	0.9987	1.0190
STAND DEV	0.0392	0.0651	0.0325	0.0230	0.0223
MINIMUM	0.9376	0.9958	0.9745	0.9690	0.9913
MAXIMUM	1.0663	1.2730	1.0995	1.0559	1.0682
	17	19	19	17	16
AVERAGE	0.9662	1.0000	0.9702	0.9507	0.9717
STAND DEV	0.0378	0.0000	0.0224	0.0181	0.0277
MINIMUM	0.8745	1.0000	0.9106	0.9063	0.9021
MAXIMUM	1.0382	1.0000	1.0124	0.9784	1.0146

	F CL MID	F CL HIGH	F CL HI I	F CL HI W	FCL**2
AVERAGE	0.9987	1.0059	0.9939	1.0151	0.9975
STAND DEV	0.0234	0.0205	0.0250	0.0248	0.0233
MINIMUM	0.9532	0.9819	0.9636	0.9833	0.9660
MAXIMUM	1.0445	1.0647	1.0613	1.0701	1.0526
	17	15	13	18	17
AVERAGE	0.9551	0.9592	0.9541	0.9646	0.9495
STAND DEV	0.0197	0.0260	0.0204	0.0249	0.0179
MINIMUM	0.9179	0.8719	0.9200	0.8715	0.9066
MAXIMUM	0.9830	0.9865	0.9852	0.9914	0.9753

	FCL*ASURF	FCL*TSURF	FCL*TS**4	FCL*T1000	FCL*TCTOP
AVERAGE	1.0134	1.0019	0.9970	1.0019	1.0020
STAND DEV	0.0273	0.0270	0.0288	0.0270	0.0283
MINIMUM	0.9804	0.9689	0.9564	0.9693	0.9682
MAXIMUM	1.0766	1.0703	1.0683	1.0704	1.0743
	17	18	18	18	18
AVERAGE	0.9635	0.9519	0.9520	0.9519	0.9519
STAND DEV	0.0229	0.0199	0.0220	0.0201	0.0205
MINIMUM	0.9000	0.9051	0.8963	0.9043	0.9044
MAXIMUM	0.9913	0.9855	0.9837	0.9857	0.9893

	FCL*MUSUN	FCL*AS*MU	T SURFACE	TSURF**2	TSURF**3
AVERAGE	1.0025	1.0077	1.0201	1.0194	1.0191
STAND DEV	0.0284	0.0282	0.0258	0.0261	0.0263
MINIMUM	0.9616	0.9764	0.9878	0.9859	0.9848
MAXIMUM	1.0644	1.0686	1.0699	1.0695	1.0692
	19	19	16	16	16
AVERAGE	0.9551	0.9601	0.9690	0.9684	0.9681
STAND DEV	0.0215	0.0241	0.0239	0.0246	0.0249
MINIMUM	0.9081	0.9008	0.9106	0.9109	0.9111
MAXIMUM	0.9862	0.9877	1.0004	1.0006	1.0007

	TSURF**4	Z500	T500	T1000	P SURFACE
AVERAGE	1.0190	1.0125	1.0130	1.0149	1.0252
STAND DEV	0.0264	0.0332	0.0324	0.0294	0.0336
MINIMUM	0.9841	0.9529	0.9659	0.9615	0.9851
MAXIMUM	1.0689	1.0741	1.0720	1.0702	1.1123
	16	17	16	18	14
AVERAGE	0.9680	0.9633	0.9609	0.9656	0.9752
STAND DEV	0.0250	0.0303	0.0282	0.0249	0.0227
MINIMUM	0.9113	0.9005	0.9059	0.9166	0.9391
MAXIMUM	1.0009	1.0043	0.9937	1.0060	1.0256

	SIGMA W V	N CLD LYR	Z CLD TOP	T CLD TOP	DS/DZ
AVERAGE	1.0133	1.0102	1.0155	1.0212	1.0065
STAND DEV	0.0320	0.0151	0.0196	0.0321	0.0393
MINIMUM	0.9668	0.9880	0.9897	0.9503	0.9376
MAXIMUM	1.0808	1.0396	1.0697	1.0812	1.0701
	16	14	15	14	13
AVERAGE	0.9635	0.9652	0.9738	0.9719	0.9515
STAND DEV	0.0262	0.0191	0.0326	0.0249	0.0346
MINIMUM	0.9015	0.9199	0.8772	0.9167	0.8824
MAXIMUM	0.9977	1.0011	1.0301	0.9956	1.0074

	DH*/DZ	DH-AV/DZ	FLAG ST W R	SURFACE	U500
AVERAGE	1.0176	1.0250	1.0279	1.0150	1.0140
STAND DEV	0.0374	0.0335	0.0413	0.0248	0.0278
MINIMUM	0.9275	0.9844	0.9611	0.9822	0.9727
MAXIMUM	1.0801	1.0869	1.0997	1.0849	1.0707
	14	12	14	13	11
AVERAGE	0.9649	0.9686	0.9721	0.9654	0.9681
STAND DEV	0.0272	0.0239	0.0220	0.0230	0.0176
MINIMUM	0.8931	0.9265	0.9285	0.9230	0.9404
MAXIMUM	0.9970	1.0009	1.0126	1.0052	0.9946

	V500	P1 LATITU	P2 LATITU	A SURFACE	ASURF**2
AVERAGE	1.0121	1.0160	1.0188	1.0136	1.0150
STAND DEV	0.0248	0.0394	0.0387	0.0444	0.0470
MINIMUM	0.9620	0.9331	0.9390	0.9028	0.8946
MAXIMUM	1.0500	1.0715	1.0713	1.0785	1.0863
	11	17	16	12	12
AVERAGE	0.9696	0.9653	0.9664	0.9608	0.9622
STAND DEV	0.0251	0.0379	0.0377	0.0404	0.0431
MINIMUM	0.9295	0.8703	0.8758	0.8693	0.8615
MAXIMUM	1.0209	1.0294	1.0276	0.9988	1.0054

	AS*MUSUN Z	SURFACE
AVERAGE	1.0201	1.0169
STAND DEV	0.0287	0.0275
MINIMUM	0.9738	0.9701
MAXIMUM	1.0714	1.0627
	14	9
AVERAGE	0.9704	0.9735
STAND DEV	0.0274	0.0426
MINIMUM	0.9003	0.8598
MAXIMUM	1.0006	1.0233

Appendix C

A COMPARISON OF THE RESULTS DERIVED FROM ANALYSES USING DIFFERENT MODELS FOR THE DIURNAL VARIATION OF BIDIRECTIONAL REFLECTANCE AND THEREFORE DIFFERENT DIURNAL CORRECTION FACTORS FOR VISIBLE RADIANCES

In this appendix I compare statistical results from three analyses of the ERB data. The statistical results I investigate include the averages of the visible flux, the covariances of this variable with the other variables I investigated, and the correlation coefficients of the visible flux with the other variables. The tables are described individually. The purpose of the comparison is to determine if the choice of the model for the diurnal variation of bidirectional reflectance (for regions of the earth surface-atmosphere system) is important for the outcome of my analysis and, if it is important, whether any given model seems to work better than the others.

TABLE C.1

In this table, I compare the results of the 49BIN CON, 49BIN MUL, and 49BIN ADD analyses to determine the effect of using different diurnal correction techniques on the visible data. I looked at average visible flux and the covariances and correlation coefficients of visible flux with non-radiative variables for the 8 LATITUDES geographic grouping. I took the ratio of the MUL result to the CON result and the ratio of the ADD result to the CON result and utilized these ratios in determining average, minimum, and maximum ratios, and standard deviations of the ratios, for each latitude band. In each latitude band, the ratios involving the 49BIN MUL analysis are presented first and those of the 49BIN ADD analysis are presented second. At the beginning of each latitude band, I present the number of 49BIN CON correlation coefficients (out of 40) that were greater than or equal to 0.15, since only these cases were investigated for the ratios of the covariances and correlation coefficients.

LATITUDE # 1	NUMBER OF CCS. 0
	AVERAGE
AVERAGE RATIO	1.000
RATIO STD DEV	0.000E+00
MINIMUM RATIO	1.000E+00
MAXIMUM RATIO	1.000E+00
	AVERAGE
AVERAGE RATIO	1.000
RATIO STD DEV	0.000E+00
MINIMUM RATIO	1.000E+00
MAXIMUM RATIO	1.000E+00

LATITUDE # 2	NUMBER OF CCS. 32		
	AVERAGE	COVARIANCE	CORR COEF
AVERAGE RATIO	1.020	1.036	0.991
RATIO STD DEV	0.000E+00	1.834E-02	1.756E-02
MINIMUM RATIO	1.020E+00	9.579E-01	9.170E-01
MAXIMUM RATIO	1.020E+00	1.079E+00	1.033E+00
	AVERAGE	COVARIANCE	CORR COEF
AVERAGE RATIO	1.016	1.024	0.993
RATIO STD DEV	0.000E+00	1.838E-02	1.782E-02
MINIMUM RATIO	1.016E+00	9.564E-01	9.274E-01
MAXIMUM RATIO	1.016E+00	1.069E+00	1.036E+00

LATITUDE # 3	NUMBER OF CCS. 27		
	AVERAGE	COVARIANCE	CORR COEF
AVERAGE RATIO	1.116	1.176	1.042
RATIO STD DEV	0.000E+00	1.795E-01	1.591E-01
MINIMUM RATIO	1.116E+00	9.374E-01	8.310E-01
MAXIMUM RATIO	1.116E+00	1.551E+00	1.375E+00
	AVERAGE	COVARIANCE	CORR COEF
AVERAGE RATIO	1.111	1.084	1.066
RATIO STD DEV	0.000E+00	2.566E-01	2.522E-01
MINIMUM RATIO	1.111E+00	7.243E-01	7.119E-01
MAXIMUM RATIO	1.111E+00	1.633E+00	1.605E+00

LATITUDE # 4	NUMBER OF CCS. 27		
	AVERAGE	COVARIANCE	CORR COEF
AVERAGE RATIO	1.286	1.485	1.066
RATIO STD DEV	0.000E+00	1.777E-01	1.276E-01
MINIMUM RATIO	1.286E+00	1.197E+00	8.590E-01
MAXIMUM RATIO	1.286E+00	1.832E+00	1.315E+00
	AVERAGE	COVARIANCE	CORR COEF
AVERAGE RATIO	1.357	1.344	1.184
RATIO STD DEV	0.000E+00	3.296E-01	2.904E-01
MINIMUM RATIO	1.357E+00	7.920E-01	6.978E-01
MAXIMUM RATIO	1.357E+00	1.967E+00	1.733E+00

LATITUDE # 5	NUMBER OF CCS. 25		
	AVERAGE	COVARIANCE	CORR COEF
AVERAGE RATIO	1.411	1.430	1.015
RATIO STD DEV	0.000E+00	7.742E-02	5.496E-02
MINIMUM RATIO	1.411E+00	1.283E+00	9.111E-01
MAXIMUM RATIO	1.411E+00	1.616E+00	1.147E+00
	AVERAGE	COVARIANCE	CORR COEF
AVERAGE RATIO	1.449	1.025	1.022
RATIO STD DEV	0.000E+00	6.026E-02	6.007E-02
MINIMUM RATIO	1.449E+00	9.268E-01	9.240E-01
MAXIMUM RATIO	1.449E+00	1.199E+00	1.196E+00

LATITUDE # 6	NUMBER OF CCS. 34		
	AVERAGE	COVARIANCE	CORR COEF
AVERAGE RATIO	1.301	1.307	1.008
RATIO STD DEV	0.000E+00	2.303E-02	1.776E-02
MINIMUM RATIO	1.301E+00	1.271E+00	9.800E-01
MAXIMUM RATIO	1.301E+00	1.383E+00	1.067E+00
	AVERAGE	COVARIANCE	CORR COEF
AVERAGE RATIO	1.315	1.002	0.997
RATIO STD DEV	0.000E+00	2.095E-02	2.086E-02
MINIMUM RATIO	1.315E+00	9.540E-01	9.499E-01
MAXIMUM RATIO	1.315E+00	1.079E+00	1.075E+00

LATITUDE # 7	NUMBER OF CCS. 33		
	AVERAGE	COVARIANCE	CORR COEF
AVERAGE RATIO	1.126	0.962	0.923
RATIO STD DEV	0.000E+00	1.819E-01	1.745E-01
MINIMUM RATIO	1.126E+00	5.375E-01	5.155E-01
MAXIMUM RATIO	1.126E+00	1.268E+00	1.216E+00
	AVERAGE	COVARIANCE	CORR COEF
AVERAGE RATIO	1.130	0.881	0.940
RATIO STD DEV	0.000E+00	1.267E-01	1.352E-01
MINIMUM RATIO	1.130E+00	5.708E-01	6.091E-01
MAXIMUM RATIO	1.130E+00	1.082E+00	1.154E+00

LATITUDE # 8	NUMBER OF CCS. 37		
	AVERAGE	COVARIANCE	CORR COEF
AVERAGE RATIO	0.955	0.953	0.933
RATIO STD DEV	0.000E+00	2.159E-01	2.115E-01
MINIMUM RATIO	9.546E-01	4.306E-01	4.218E-01
MAXIMUM RATIO	9.546E-01	1.392E+00	1.364E+00
	AVERAGE	COVARIANCE	CORR COEF
AVERAGE RATIO	0.966	0.995	0.979
RATIO STD DEV	0.000E+00	1.751E-01	1.723E-01
MINIMUM RATIO	9.656E-01	5.502E-01	5.412E-01
MAXIMUM RATIO	9.656E-01	1.390E+00	1.367E+00

TABLE C.2

In this table (as in table C.1), I compare the results of the 49BIN CON, 49BIN MUL, and 49BIN ADD analyses to determine the effect of using different diurnal correction techniques on the visible data. I looked at average visible flux and the covariances and correlation coefficients of visible flux with all variables for each of the geographic groupings. I took the ratio of the MUL result to the CON result and the ratio of the ADD result to the CON result and utilized these ratios in determining average, minimum, and maximum ratios, and standard deviations of the ratios, for the average visible flux and for each of the visible flux covariances and correlation coefficients. The ratios involving the 49BIN MUL analysis are presented first and those of the 49BIN ADD analysis are presented second. At the beginning of each presentation, I tabulate the results for the average flux ratios. Then for each variable (with which visible flux was correlated) the covariance results are tabulated followed by the number of 49BIN CON correlation coefficients (out of 20) that were greater than or equal to 0.15 (since, as in the last table, only these cases were investigated for the ratios of the covariances and correlation coefficients) followed by the ratio results for the correlation coefficients.

	20
AVERAGE	1.1706
STAND DEV	0.1446
MINIMUM	0.9546
MAXIMUM	1.4108

	AVG MUSUN	FLUX UP V	FLUX UP I	F CL TOTL	F CL LOW
AVERAGE	1.1588	1.4176	1.1709	1.1676	1.1906
STAND DEV	0.3769	0.4495	0.2095	0.2039	0.2110
MINIMUM	0.5375	0.7913	0.8576	0.7954	0.8406
MAXIMUM	1.8253	2.3572	1.5330	1.4985	1.6532
	14	19	18	18	15
AVERAGE	0.9957	1.0000	0.9975	0.9871	1.0257
STAND DEV	0.2076	0.0000	0.0806	0.0816	0.0879
MINIMUM	0.5155	1.0000	0.7777	0.8466	0.8234
MAXIMUM	1.3102	1.0000	1.1652	1.1676	1.1996

	F CL MID	F CL HIGH	F CL HI I	F CL HI W	FCL**2
AVERAGE	1.2311	1.1432	1.3474	1.1385	1.1670
STAND DEV	0.1778	0.2585	0.2524	0.2590	0.2054
MINIMUM	0.8787	0.5356	1.0330	0.5253	0.7990
MAXIMUM	1.5072	1.5440	2.0037	1.5133	1.5006
	17	17	12	18	18
AVERAGE	1.0436	0.9682	1.1002	0.9550	0.9866
STAND DEV	0.1504	0.1381	0.2935	0.1196	0.0844
MINIMUM	0.8761	0.5247	0.9160	0.5146	0.8332
MAXIMUM	1.4278	1.2715	2.0554	1.0678	1.1756

	FCL*ASURF	FCL*TSURF	FCL*TS**4	FCL*T1000	FCL*TCTOP
AVERAGE	1.1185	1.1782	1.1848	1.1770	1.1791
STAND DEV	0.2304	0.2037	0.2131	0.2049	0.2053
MINIMUM	0.7700	0.7967	0.7590	0.7957	0.7878
MAXIMUM	1.4286	1.4999	1.5039	1.5001	1.4997
	17	18	18	18	18
AVERAGE	0.9419	0.9970	0.9986	0.9959	0.9976
STAND DEV	0.0854	0.0940	0.1048	0.0941	0.0957
MINIMUM	0.6683	0.8337	0.7435	0.8237	0.8345
MAXIMUM	1.0848	1.2443	1.3051	1.2406	1.2549

	FCL*MUSUN	FCL*AS*MU	T SURFACE	TSURF**2	TSURF**3
AVERAGE	1.1897	1.1429	1.1470	1.1473	1.1476
STAND DEV	0.1992	0.2074	0.2751	0.2752	0.2754
MINIMUM	0.8053	0.8112	0.7956	0.7957	0.7959
MAXIMUM	1.5178	1.4588	1.6576	1.6586	1.6597
	19	19	16	16	16
AVERAGE	1.0112	0.9689	0.9915	0.9917	0.9920
STAND DEV	0.0487	0.0468	0.1381	0.1382	0.1384
MINIMUM	0.9012	0.8809	0.8162	0.8163	0.8164
MAXIMUM	1.1074	1.0708	1.3608	1.3603	1.3599

	TSURF**4	Z500	T500	T1000	P SURFACE
AVERAGE	1.1480	1.0637	1.0641	1.1477	1.1850
STAND DEV	0.2755	0.2939	0.3283	0.2767	0.3443
MINIMUM	0.7960	0.7293	0.6110	0.7873	0.6053
MAXIMUM	1.6607	1.8154	1.6695	1.6982	1.7213
	16	14	13	16	16
AVERAGE	0.9923	0.9320	0.9398	0.9932	0.9907
STAND DEV	0.1386	0.1421	0.1699	0.1443	0.1597
MINIMUM	0.8166	0.6577	0.5861	0.7714	0.5930
MAXIMUM	1.3594	1.1824	1.1984	1.3748	1.2355

	SIGMA W V	N CLD LYR	Z CLD TOP	T CLD TOP	DS/DZ
AVERAGE	1.2128	1.2333	1.1715	1.1167	1.2489
STAND DEV	0.3563	0.1840	0.1928	0.2299	0.2735
MINIMUM	0.6262	0.9852	0.8014	0.8280	0.8861
MAXIMUM	1.7014	1.5222	1.4945	1.6261	1.8682
	17	15	14	16	11
AVERAGE	1.0089	1.0488	0.9950	0.9689	1.0908
STAND DEV	0.1870	0.1055	0.0816	0.0809	0.0818
MINIMUM	0.6424	0.8551	0.7850	0.8310	0.9834
MAXIMUM	1.3727	1.3384	1.0808	1.1815	1.2474

	DH*/DZ	DH-AV/DZ	FLAG ST W R	SURFACE	U500
AVERAGE	1.2034	1.1554	1.1719	1.1761	1.2157
STAND DEV	0.2983	0.2728	0.3719	0.2069	0.4341
MINIMUM	0.8188	0.7202	0.2544	0.9145	0.5462
MAXIMUM	1.8486	1.6266	1.6821	1.5213	2.1548
	14	14	14	14	11
AVERAGE	1.0338	0.9936	0.9566	1.0109	1.0213
STAND DEV	0.1396	0.1117	0.2116	0.0579	0.2541
MINIMUM	0.8400	0.7389	0.2609	0.9042	0.6062
MAXIMUM	1.4355	1.2018	1.1517	1.1242	1.6515

	V500	P1 LATITU	P2 LATITU	A SURFACE	ASURF**2
AVERAGE	1.1832	1.1533	1.1062	1.1292	1.0591
STAND DEV	0.1553	0.3837	0.3562	0.2791	0.2135
MINIMUM	0.9579	0.5662	0.5652	0.7573	0.7557
MAXIMUM	1.5179	1.8324	1.7904	1.7282	1.4388
	11	14	13	12	11
AVERAGE	1.0301	0.9884	0.9701	0.9862	0.9601
STAND DEV	0.1003	0.2087	0.2032	0.1070	0.0977
MINIMUM	0.9070	0.5431	0.5422	0.8360	0.8197
MAXIMUM	1.2707	1.3153	1.2851	1.2368	1.2045

	AS*MUSUN Z	SURFACE
AVERAGE	1.0537	1.1097
STAND DEV	0.1920	0.2819
MINIMUM	0.7568	0.4306
MAXIMUM	1.3063	1.4980
	11	12
AVERAGE	0.9430	0.9175
STAND DEV	0.0707	0.1655
MINIMUM	0.8272	0.4218
MAXIMUM	1.0250	1.0867

	20
AVERAGE	1.1864
STAND DEV	0.1578
MINIMUM	0.9656
MAXIMUM	1.4637

	AVG MUSUN	FLUX UP V	FLUX UP I	F CL TOTL	F CL LOW
AVERAGE	1.1590	1.0569	1.0196	0.9742	1.0091
STAND DEV	0.3991	0.2144	0.1931	0.1185	0.1323
MINIMUM	0.5708	0.7210	0.6358	0.6967	0.7920
MAXIMUM	1.9624	1.5729	1.6385	1.1850	1.4129
	14	19	18	18	15
AVERAGE	1.1081	1.0000	0.9993	0.9593	1.0102
STAND DEV	0.2915	0.0000	0.1244	0.1215	0.1039
MINIMUM	0.6091	1.0000	0.6124	0.6249	0.6978
MAXIMUM	1.7289	1.0000	1.3065	1.1278	1.1733

	F CL MID	F CL HIGH	F CL HI I	F CL HI W	FCL**2
AVERAGE	1.0155	0.9613	1.0645	0.9656	0.9716
STAND DEV	0.1422	0.1406	0.1277	0.1431	0.1247
MINIMUM	0.7583	0.6582	0.8901	0.6489	0.6357
MAXIMUM	1.3896	1.2718	1.3324	1.2203	1.1777
	17	17	12	18	18
AVERAGE	1.0029	0.9544	1.0481	0.9453	0.9570
STAND DEV	0.1677	0.1168	0.1660	0.1062	0.1285
MINIMUM	0.6802	0.6476	0.8575	0.6384	0.5702
MAXIMUM	1.3671	1.1412	1.5563	1.0459	1.1295

	FCL*ASURF	FCL*TSURF	FCL*TS**4	FCL*T1000	FCL*TCTOP
AVERAGE	0.9669	0.9871	1.0081	0.9860	0.9883
STAND DEV	0.1888	0.1136	0.1188	0.1141	0.1147
MINIMUM	0.4458	0.7313	0.7501	0.7307	0.7307
MAXIMUM	1.3575	1.1863	1.1912	1.1862	1.1858
	17	18	18	18	18
AVERAGE	0.9490	0.9712	0.9790	0.9702	0.9722
STAND DEV	0.1381	0.1147	0.1028	0.1147	0.1143
MINIMUM	0.4294	0.6560	0.7309	0.6554	0.6555
MAXIMUM	1.0824	1.1753	1.2192	1.1725	1.1825

	FCL*MUSUN	FCL*AS*MU	T SURFACE	TSURF**2	TSURF**3
AVERAGE	1.0428	1.0035	1.0905	1.0911	1.0916
STAND DEV	0.1282	0.1291	0.2716	0.2725	0.2735
MINIMUM	0.7988	0.8079	0.7689	0.7685	0.7681
MAXIMUM	1.3617	1.2554	1.6417	1.6439	1.6462
	19	19	16	16	16
AVERAGE	1.0185	0.9801	1.0633	1.0637	1.0641
STAND DEV	0.0529	0.0626	0.1918	0.1923	0.1928
MINIMUM	0.9145	0.7682	0.8892	0.8895	0.8898
MAXIMUM	1.1039	1.0726	1.5671	1.5671	1.5671

	TSURF**4	Z500	T500	T1000	P SURFACE
AVERAGE	1.0922	1.0292	1.0636	1.0923	1.0902
STAND DEV	0.2744	0.2435	0.3407	0.2695	0.2848
MINIMUM	0.7678	0.7628	0.6386	0.7670	0.7350
MAXIMUM	1.6486	1.4840	1.8653	1.6328	1.7439
	16	14	13	16	16
AVERAGE	1.0646	1.0056	1.0384	1.0655	1.0517
STAND DEV	0.1933	0.1349	0.2367	0.1926	0.1889
MINIMUM	0.8901	0.8299	0.6814	0.8776	0.7402
MAXIMUM	1.5672	1.3311	1.6434	1.6050	1.5365

	SIGMA W V	N CLD LYR Z	CLD TOP T	CLD TOP	DS/DZ
AVERAGE	1.1080	1.0378	1.0319	1.0226	1.1910
STAND DEV	0.2902	0.1330	0.1989	0.2212	0.2855
MINIMUM	0.6581	0.7906	0.7993	0.7243	0.8648
MAXIMUM	1.7417	1.3941	1.5624	1.5561	1.8111
	17	15	14	16	11
AVERAGE	1.0633	1.0389	1.0134	1.0034	1.1606
STAND DEV	0.2157	0.1131	0.1209	0.1331	0.1423
MINIMUM	0.7751	0.7616	0.7700	0.7119	0.9966
MAXIMUM	1.6779	1.2283	1.2458	1.3958	1.5040

	DH*/DZ	DH-AV/DZ	FLAG ST W R	SURFACE	U500
AVERAGE	1.1266	1.0640	1.0292	1.0168	1.1434
STAND DEV	0.3252	0.2187	0.2440	0.1384	0.5326
MINIMUM	0.7947	0.7310	0.5018	0.8503	0.6316
MAXIMUM	1.8413	1.4850	1.4651	1.4349	2.5224
	14	14	14	14	11
AVERAGE	1.1031	1.0325	0.9903	1.0129	1.0875
STAND DEV	0.2329	0.1172	0.1438	0.1074	0.3676
MINIMUM	0.9324	0.8609	0.5910	0.7627	0.7279
MAXIMUM	1.7738	1.3084	1.1886	1.2642	2.0112

	V500	P1 LATITU	P2 LATITU	A SURFACE	ASURF**2
AVERAGE	1.0519	1.1574	1.0970	1.0359	1.0160
STAND DEV	0.1839	0.4049	0.3715	0.2178	0.2067
MINIMUM	0.9490	0.5910	0.5908	0.7761	0.7774
MAXIMUM	1.6125	1.9669	1.9340	1.5989	1.5287
	11	14	13	12	11
AVERAGE	1.0259	1.1049	1.0541	1.0093	1.0054
STAND DEV	0.1427	0.2931	0.2664	0.1360	0.1210
MINIMUM	0.8952	0.6306	0.6304	0.8984	0.9016
MAXIMUM	1.4465	1.7330	1.7040	1.4342	1.3713

	AS*MUSUN Z	SURFACE
AVERAGE	0.9812	0.9843
STAND DEV	0.1548	0.1901
MINIMUM	0.7724	0.5502
MAXIMUM	1.3576	1.3779
	11	12
AVERAGE	0.9721	0.9392
STAND DEV	0.0635	0.1528
MINIMUM	0.8617	0.5412
MAXIMUM	1.0825	1.2360

Appendix D

A STATISTICAL COMPARISON OF THE RESULTS DERIVED FROM ANALYSES USING DIFFERENT QUANTITIES OF DATA

In this appendix I compare statistical results from two analyses of the ERB data. The statistical results I investigate include the averages for the visible flux, the covariances of this variable with the other variables I investigated, and the correlation coefficients of the visible fluxes with the other variables. The tables are described individually. The purpose of this comparison is to determine the magnitude of errors introduced by analyzing only a small portion of the available data.

TABLE D.1

In this table, I compare the results of the 6DAY 49BA and 49BIN ADD analyses to determine the effect of using different amounts of data on the resulting statistics. I looked at average visible flux and the covariances and correlation coefficients of visible flux with non-radiative variables for the 8 LATITUDES geographic grouping. I took the ratios of the 49BIN ADD results to the 6DAY 49BA results and utilized these ratios in determining average, minimum, and maximum ratios, and standard deviations of the ratios, for each latitude band. At the beginning of each latitude band, I present the number of 6DAY 49BA correlation coefficients (out of 40) that were greater than or equal to 0.15, since only these cases were investigated for the ratios of the covariances and correlation coefficients.

LATITUDE # 1	NUMBER OF CCS. 0
	AVERAGE
AVERAGE RATIO	1.000
RATIO STD DEV	0.000E+00
MINIMUM RATIO	1.000E+00
MAXIMUM RATIO	1.000E+00

LATITUDE # 2	NUMBER OF CCS. 28		
	AVERAGE	COVARIANCE	CORR COEF
AVERAGE RATIO	0.954	1.121	1.120
RATIO STD DEV	0.000E+00	3.209E-01	3.376E-01
MINIMUM RATIO	9.544E-01	-1.193E-01	-1.292E-01
MAXIMUM RATIO	9.544E-01	1.604E+00	1.985E+00

LATITUDE # 3	NUMBER OF CCS. 31		
	AVERAGE	COVARIANCE	CORR COEF
AVERAGE RATIO	1.007	0.862	0.990
RATIO STD DEV	0.000E+00	1.714E-01	2.019E-01
MINIMUM RATIO	1.007E+00	2.256E-01	2.810E-01
MAXIMUM RATIO	1.007E+00	1.113E+00	1.366E+00

LATITUDE # 4	NUMBER OF CCS. 30		
	AVERAGE	COVARIANCE	CORR COEF
AVERAGE RATIO	0.996	1.027	1.141
RATIO STD DEV	0.000E+00	3.110E-01	2.958E-01
MINIMUM RATIO	9.958E-01	4.174E-01	5.243E-01
MAXIMUM RATIO	9.958E-01	2.212E+00	2.193E+00

LATITUDE # 5	NUMBER OF CCS. 25		
	AVERAGE	COVARIANCE	CORR COEF
AVERAGE RATIO	0.995	1.059	1.101
RATIO STD DEV	0.000E+00	1.684E-01	1.863E-01
MINIMUM RATIO	9.953E-01	6.832E-01	5.918E-01
MAXIMUM RATIO	9.953E-01	1.450E+00	1.610E+00

LATITUDE # 6	NUMBER OF CCS. 35		
	AVERAGE	COVARIANCE	CORR COEF
AVERAGE RATIO	0.990	0.832	0.976
RATIO STD DEV	0.000E+00	2.071E-01	2.344E-01
MINIMUM RATIO	9.903E-01	3.753E-01	4.609E-01
MAXIMUM RATIO	9.903E-01	1.319E+00	1.522E+00

LATITUDE # 7	NUMBER OF CCS. 33		
	AVERAGE	COVARIANCE	CORR COEF
AVERAGE RATIO	0.995	1.235	1.104
RATIO STD DEV	0.000E+00	1.858E-01	1.834E-01
MINIMUM RATIO	9.951E-01	8.293E-01	7.528E-01
MAXIMUM RATIO	9.951E-01	1.929E+00	1.709E+00

LATITUDE # 8	NUMBER OF CCS. 37		
	AVERAGE	COVARIANCE	CORR COEF
AVERAGE RATIO	1.011	0.953	1.071
RATIO STD DEV	0.000E+00	2.760E-01	2.261E-01
MINIMUM RATIO	1.011E+00	4.375E-01	4.600E-01
MAXIMUM RATIO	1.011E+00	1.863E+00	1.616E+00

TABLE D.2

In this table (as in table D.1), I compare the results of the 6DAY 49BA and 49BIN ADD analyses to determine the effect of using different amounts of data on the resulting statistics. I looked at average visible flux and the covariances and correlation coefficients of visible flux with all variables for each of the geographic groupings. I took the ratios of the 49BIN ADD results to the 6DAY 49BA results and utilized these ratios in determining average, minimum, and maximum ratios, and standard deviations of the ratios, for the average visible flux and each of the visible flux covariances and correlation coefficients. At the beginning of the table, I tabulate the results for the average flux ratios. Then for each variable (with which visible flux was correlated) the covariance results are tabulated followed by the number of 6DAY 49BA correlation coefficients (out of 20) that were greater than or equal to 0.15 (since, as in the last table, only these cases were investigated for the ratios of the covariances and correlation coefficients) followed by the ratio results for the correlation coefficients.

	20
AVERAGE	0.9898
STAND DEV	0.0300
MINIMUM	0.9178
MAXIMUM	1.0527

	AVG MUSUN	FLUX UP V	FLUX UP I	F CL TOTL	F CL LOW
AVERAGE	0.9665	0.9367	1.0251	1.0793	1.0266
STAND DEV	0.1946	0.1533	0.3180	0.4125	0.3230
MINIMUM	0.3753	0.6145	-0.1660	0.2102	0.6250
MAXIMUM	1.2750	1.2282	1.4247	2.3444	2.0643
	17	19	19	17	16
AVERAGE	0.9995	1.0000	1.0086	1.1335	1.0556
STAND DEV	0.1688	0.0000	0.3140	0.3892	0.1758
MINIMUM	0.4609	1.0000	-0.2709	0.3588	0.7449
MAXIMUM	1.2297	1.0000	1.3511	2.4621	1.3503

	F CL MID	F CL HIGH	F CL HI I	F CL HI W	FCL**2
AVERAGE	0.9343	0.9711	1.0470	0.9907	1.0594
STAND DEV	0.3390	0.2322	0.2259	0.3341	0.3935
MINIMUM	0.2619	0.2250	0.5051	0.3515	0.1563
MAXIMUM	1.6959	1.2575	1.4039	1.7853	2.2165
	17	15	13	18	17
AVERAGE	0.9631	1.0947	1.1432	1.0657	1.1094
STAND DEV	0.2848	0.1125	0.2302	0.1534	0.3663
MINIMUM	0.3337	0.8924	0.8164	0.7797	0.2637
MAXIMUM	1.4553	1.4013	1.6071	1.3950	2.2736

	FCL*ASURF	FCL*TSURF	FCL*TS**4	FCL*T1000	FCL*TCTOP
AVERAGE	0.9411	1.1258	1.0042	1.1265	1.1230
STAND DEV	0.3005	0.5021	0.2774	0.5032	0.4852
MINIMUM	-0.0839	0.2300	0.2854	0.2283	0.2311
MAXIMUM	1.1960	2.8805	1.6020	2.8829	2.7900
	17	18	18	18	18
AVERAGE	0.9876	1.1786	1.0542	1.1794	1.1787
STAND DEV	0.3154	0.5024	0.1939	0.5033	0.4891
MINIMUM	-0.1390	0.3982	0.5114	0.3938	0.3970
MAXIMUM	1.3461	3.0795	1.4456	3.0803	3.0195

	FCL*MUSUN	FCL*AS*MU	T SURFACE	TSURF**2	TSURF**3
AVERAGE	1.0246	0.9531	0.9620	0.9663	0.9669
STAND DEV	0.2818	0.2080	0.1226	0.1203	0.1212
MINIMUM	0.3753	0.2585	0.7890	0.7761	0.7634
MAXIMUM	1.9172	1.1876	1.2116	1.2096	1.2109
	19	19	16	16	16
AVERAGE	1.1084	1.0306	1.0527	1.0260	1.0200
STAND DEV	0.2332	0.1493	0.1121	0.0784	0.0779
MINIMUM	0.7036	0.5085	0.8674	0.8752	0.8789
MAXIMUM	1.9709	1.2362	1.3659	1.1556	1.1591

	TSURF**4	Z500	T500	T1000	P SURFACE
AVERAGE	0.9666	0.9407	0.8749	1.0205	1.1612
STAND DEV	0.1226	0.2208	0.3798	0.2609	0.6286
MINIMUM	0.7510	0.6832	-0.1300	0.6313	0.5343
MAXIMUM	1.2132	1.4705	1.6969	1.8990	3.1894
	16	17	16	18	14
AVERAGE	1.0174	0.9669	0.9312	1.1185	1.2079
STAND DEV	0.0792	0.2118	0.3889	0.2904	0.5562
MINIMUM	0.8800	0.5918	-0.1576	0.7406	0.5389
MAXIMUM	1.1611	1.5435	1.8708	2.1637	2.7833

	SIGMA W V	N CLD LYR	Z CLD TOP	T CLD TOP	DS/DZ
AVERAGE	0.9511	1.0454	0.9919	0.9944	0.9599
STAND DEV	0.2056	0.4058	0.3375	0.1773	0.4251
MINIMUM	0.6275	0.0501	0.4174	0.5827	0.1870
MAXIMUM	1.4027	1.8451	1.8625	1.3409	1.7246
	16	14	15	14	13
AVERAGE	1.0150	1.1046	1.1059	1.0528	1.0039
STAND DEV	0.2062	0.3317	0.2564	0.1298	0.3698
MINIMUM	0.7555	0.1580	0.5243	0.8083	0.2393
MAXIMUM	1.5206	1.6159	1.5116	1.4268	1.5098

	DH*/DZ	DH-AV/DZ	FLAG ST W R	SURFACE	U500
AVERAGE	0.9921	1.1123	1.0609	1.0875	0.7917
STAND DEV	0.2663	0.3105	0.4373	0.3225	0.7124
MINIMUM	0.2666	0.7138	-0.0414	0.4330	-0.1902
MAXIMUM	1.4243	1.9292	1.7703	1.8353	2.2122
	14	12	14	13	11
AVERAGE	1.0559	1.1679	1.2155	1.1165	0.8097
STAND DEV	0.2102	0.2347	0.5201	0.2738	0.7100
MINIMUM	0.4498	0.8896	-0.0573	0.5168	-0.2005
MAXIMUM	1.3581	1.7087	2.0010	1.5904	2.1932

	V500	P1 LATITU	P2 LATITU	A SURFACE	ASURF**2
AVERAGE	0.9225	0.9595	1.0178	0.9898	1.0207
STAND DEV	0.3249	0.1553	0.2537	0.1624	0.1316
MINIMUM	0.3641	0.4673	0.4780	0.5231	0.6545
MAXIMUM	1.4981	1.1895	1.7734	1.1538	1.1841
	11	17	16	12	12
AVERAGE	0.9436	0.9868	1.0514	1.0351	1.0644
STAND DEV	0.3025	0.1379	0.2542	0.1920	0.1662
MINIMUM	0.5080	0.5500	0.5623	0.6138	0.7663
MAXIMUM	1.5199	1.2192	1.8657	1.5134	1.5178

	AS*MUSUN Z	SURFACE
AVERAGE	0.9246	0.9516
STAND DEV	0.1727	0.1399
MINIMUM	0.5190	0.7015
MAXIMUM	1.1019	1.1543
	14	9
AVERAGE	0.9449	1.0349
STAND DEV	0.1350	0.1714
MINIMUM	0.6097	0.7363
MAXIMUM	1.0746	1.3766